International Reviews in Physical Chemistry
Vol. 28, No. 4, October–December 2009, 607–680

Taylor & Francis
Taylor & Francis Group

Imaging chemical reactions – 3D velocity mapping

A. I. Chichinin[ab], K.-H. Gericke[a]*, S. Kauczok[a] and C. Maul[a]

[a]*Institut für Physikalische und Theoretische Chemie, Technische Universität Braunschweig, Hans-Sommer-Straße 10, 38106 Braunschweig, Germany;* [b]*Institute of Chemical Kinetics and Combustion, 630090 Novosibirsk, Russia*

(*Received 13 July 2009; final version received 2 August 2009*)

Visualising a collision between an atom or a molecule or a photodissociation (half-collision) of a molecule on a single particle and single quantum level is like watching the collision of billiard balls on a pool table: Molecular beams or monoenergetic photodissociation products provide the colliding reactants at controlled velocity before the reaction products velocity is imaged directly with an elaborate camera system, where one should keep in mind that velocity is, in general, a three-dimensional (3D) vectorial property which combines scattering angles and speed. If the processes under study have no cylindrical symmetry, then only this 3D product velocity vector contains the full information of the elementary process under study.

Keywords: reaction dynamics; ion imaging; velocity map imaging; REMPI; reactive scattering; photodissociaton; time-of-flight spectrometry

Contents

*Corresponding author. Email: k.gericke@tu-bs.de

ISSN 0144–235X print/ISSN 1366–591X online

DOI: 10.1080/01442350903235045
http://www.informaworld.com

1. Introduction

Imaging experiments in chemical dynamics provide dynamical information about elementary chemical processes, e.g. whether a reaction product is translationally or internally excited, what is the nature of the internal excitation and whether or not the spatial product distribution is anisotropic. All these data yield information about the nature of the electronic states and the potential energy surfaces controlling the elementary chemical process [1]. Imaging techniques have experienced a rapid development immediately after the first report of a two-dimensional (2D) imaging experiment on the photodissociation of CH_3I by Chandler and Houston in 1987 [2]. Since then conceptual and technological improvements have yielded a too large number of diverse applications to be manageable in a single review article like this one. Therefore, the scope of this article is restricted to the two following topics.

The first part of this review deals with one of the most exciting recent innovations in chemical dynamics imaging techniques which is the development of full three-dimensional (3D) imaging spectroscopy. Naturally, full 3D imaging is the ultimate goal of the experimentalist who wants to study elementary chemical dynamics. It allows the full 3D momentum vector of chemical products to be experimentally determined in addition to the product quantum state, thus eliminating the need to rely on mathematical reconstruction or forward convolution methods.

Generally speaking, 2D imaging yields complete information only about systems if the third dimension does not contain independent information. This condition is always fulfilled for systems with cylindrical symmetry or where the total angular dependence $F_\Omega(\theta, \phi)$ can be factorised with respect to the polar angle θ and the azimuthal angle ϕ: $F_\Omega(\theta, \phi) = F_\theta(\theta)F_\phi(\phi)$. While impressive results have been obtained by 2D imaging techniques, their application is limited to the systems of favourable properties [1]. Figure 1 shows a simple example for which the reconstruction of the 3D distribution from a set of three orthogonal 2D projections is not possible once the system does not have any symmetry or the system's symmetry is unknown. The reconstruction of arbitrary 3D distributions from 2D images without *a priori* symmetry assumptions must rely on tomographic concepts, which require a large number of projections to be monitored for different viewing angles. 3D imaging is therefore a powerful, timely and elegant method to circumvent the tedious, if not impossible task of tomography in chemical dynamics. Its main application field should ultimately be the study of chemical processes exhibiting no or low symmetry, such as bimolecular reactions of aligned or oriented reactants with controlled angles of attack, but also much simpler systems, for example the photodissociation of aligned or oriented molecules.

The focus of the first part of this review will be laid on the transition from the nowadays widely established 2D velocity map imaging (VMI) technique to real 3D imaging and VMI schemes and their applications in the field of reaction dynamics. Several approaches for realising 3D imaging schemes are presented, their merits and limitations

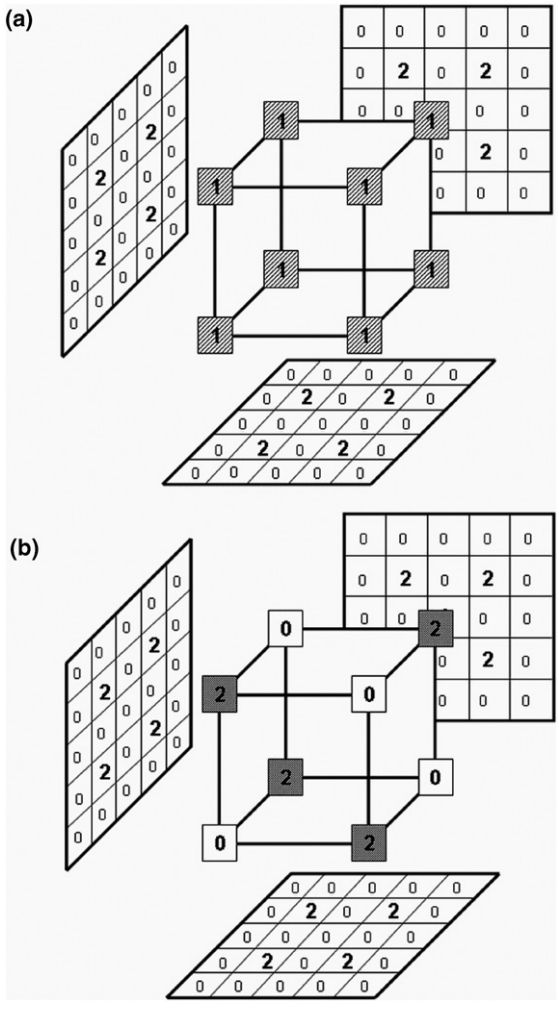

Figure 1. Recovery of a 3D distribution from 2D images. The central cube schematically represents a 3D distribution, with the numbers on the corners reflecting space dependent particle densities. Numbers on the screens show the corresponding intensity distributions in three orthogonal 2D images, resulting from projection of the 3D distribution into a plane. 2D imaging cannot discriminate between the isotropic case (a) and the anisotropic case (b).

are evaluated, experimental results are presented and future developments are discussed. In this part of the article, we outline the general approach of 3D imaging and discuss the important issue of sensitivity of the method. These more general considerations are followed by a short historic overview of how dimension by dimension has been added to conventional time-of-flight (TOF) mass spectroscopy until real 3D imaging spectroscopy was finally realised. Next, the achievable overall resolution in 3D imaging is discussed which is probably the most crucial point in 3D imaging experiments because optimising the resolution in any one dimension strongly affects, i.e. normally deteriorates, the resolution in another. The discussed sensitivity, uncertainty and resolution considerations

let us present some basic design strategies setting up 3D imaging experiments. The last section of the first part of this review is dedicated to the presentation of state of the art applications of 3D imaging to complex chemical reaction dynamics systems.

In the second part of this review we highlight several developments in technological advancements related to chemical imaging in a more general sense and give an overview of imaging studies presented after the publication of the review article of Ashfold *et al.* [1] in which the development of imaging spectroscopy from its beginning as TOF mass spectroscopy to current state of the art VMI has comprehensively been reviewed. In particular, we present an overview over common and less common position sensitive detectors that either have been or are being used for the study of reaction dynamics imaging or that might be applicable in this context. Also, various electric field configurations are discussed which in addition to simply accelerating products towards the detector can be designed to result in focussing conditions that significantly improve the resolution performance of an imaging setup. Following this technical sections, we present a comprehensive review over recent imaging studies of chemical elementary processes, in particular on photodissociation, alignment and orientation and bimolecular reactions, before we summarise the presented data and give an outlook what the future might bring for imaging applications in reaction dynamics.

2. Imaging three dimensions

2.1. *3D imaging*

2.1.1. *General approach*

The general aim of 3D imaging spectroscopy is to obtain a complete kinematic description of a chemical elementary process, which can be either the unimolecular decay or a bimolecular reaction. In both cases the quantum state q of a product as well as its 3D momentum vector $\vec{p}$ needs to be determined simultaneously.

In order to determine the momentum vector $\vec{p}$ of a product generated in a chemical elementary process, this process must be initiated at a well-defined time and the product must not undergo any collisions prior to its detection. In order to meet both demands simultaneously, the process is usually initiated by the action of a pulsed laser in the low pressure environment of a vacuum chamber. For the spectroscopic analysis of the product quantum state q normally a second, tunable pulsed laser is necessary. Not always two independent lasers are needed to fulfil these tasks. In the favourable case of a so-called one-colour experiment a single laser can do both tasks at the same time. The initiating laser does not only set the start time $t=0$, but the direction of its polarisation vector also defines the coordinate system (X, Y, Z) for the measurement of the product momentum vector $\vec{p}$, with the origin of the coordinate system normally lying in the centre of the laser focus. For the study of a photoinitiated bimolecular reaction the coordinate system may be defined differently, e.g. by using two (crossed) molecular beams or by a defined displacement of initiating and analysing lasers. Once the coordinate system (X, Y, Z) and the start time have been established by the action of the first laser and the product has been tagged by the action of the second, the product momentum vector $\vec{p}$ needs to be measured. The best way to do this is to monitor the TOF t of the particle when it arrives at a suitable detector. The original (and the simplest) form of such an experiment has been called photofragment translational spectroscopy and makes use of a movable particle detector

for repeated measurements of the tagged particles' TOF distribution in different directions [3–5]. A disadvantage of this method is that most produced particles will not fly towards the detector and that the number of registered particles is consequently very small. In fact, the higher the spatial resolution is, the smaller must be the detector surface area and the smaller becomes the count rate. Therefore it is desirable to record all products generated in the studied process and to discriminate their momentum vectors $\vec{p}$ after their detection from the properties of the monitored detector signal.

In order to enforce the detection of all tagged particles, at some stage of the process charged particles must be involved, so that electric fields can be used to direct them towards the detector. This can be the case for the precursors of the reaction, e.g. if ionic reactions or photodetachment processes of anions are to be studied. Most common, however, is to generate the charged particle in the tagging process by resonance enhanced multi-photon ionisation (REMPI). The ionised product is then accelerated towards a particle detector where it is monitored. For describing the detected products' image on the detector we use a detector based coordinate system (x, y, z) with the z axis aligned along the axis of the TOF spectrometer and x and y axes defining the detector surface. The detector based coordinate system $(x>, y, z)$ can be transformed into the laser based system (X, Y, Z) by a simple rotation. If the polarisation vector of the initiating laser is oriented along the spectrometer axis, the two systems are identical. Laser based and spectrometer based coordinate systems are illustrated in Figure 2.

Now consider a hypothetical reference particle with zero momentum vector $\vec{p} = (0, 0, 0)$, generated at $t = 0$ in the centre of the laser focus ($x = y = z = 0$). The TOF t_0 and the impact position (x_0, y_0) of this reference particle are determined by the particle's mass m only. Gating the detector offers therefore a simple tool for discriminating against ions of different masses resulting from any otherwise possibly interfering processes. However, the individual TOF t and the individual impact position (x, y) of an ionised product of mass m depends not only on its mass, but also on its initial momentum vector $\vec{p} = (p_x, p_y, p_z)$ which it has obtained in the chemical process under investigation. Therefore, the quantities $\Delta t = t - t_0$, $\Delta x = x - x_0$ and $\Delta y = y - y_0$ are the relevant quantities

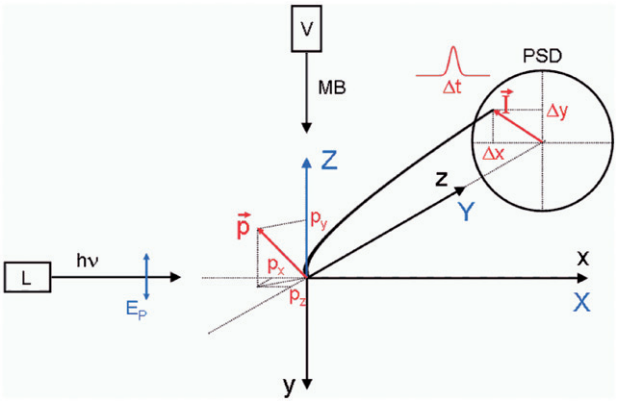

Figure 2. [Colour online] Laser based (XYZ, blue) and spectrometer based (xyz, black) coordinate systems. The PSD is situated on the z axis, the laser beam (L) and the molecular beam (MB) propagate in x and y directions, respectively. The curved trajectory along the z axis shows how the initial momentum vector $\vec{p}$ is transformed into the measured image vector $\vec{I}$.

that need to be determined simultaneously and with high precision in a 3D imaging experiment. We call the vector $\vec{I}$ combining the three relevant observable quantities the image vector: $\vec{I} = (I_1, I_2, I_3) = (\Delta x, \Delta y, \Delta t)$. How the quantities $I_1 = \Delta x$, $I_2 = \Delta y$, and $I_3 = \Delta t$ can simultaneously be measured with sufficiently high accuracy, how they are related to $\vec{p}$ and how $\vec{p}$ can be extracted from the measured values are the principal questions to be asked and to be answered. Image and momentum vectors are also illustrated in Figure 2.

Unfortunately the components of $\vec{I}$ are not only affected by the initial momentum to be imaged, but also by the initial conditions. Of course, it is important not to disregard any non-zero momentum vectors of the precursor particles, in particular when performing room-temperature experiments or fast beam experiments with accelerated, charged precursor molecules. However, mostly imaging experiments are performed under the low temperature conditions prevailing in a supersonic gas expansion, and therefore the precursor momentum vector can in good approximation be assumed to be zero. More important for imaging experiments are therefore the uncertainties in the source position of the imaged particles and their time of generation given by the random variables $(\delta x, \delta y, \delta z)$ and δt determined by the duration of the laser pulse. Therefore, the experimental image vector $\vec{I}_E = (I_{E1}, I_{E2}, I_{E3}) = (\Delta x_E, \Delta y_E, \Delta t_E)$ depends on seven parameters as shown in Equation (1):

$$\begin{aligned} I_{E1} &= \Delta x_E = f_1(p_x, p_y, p_z;\ \delta x, \delta y, \delta z, \delta t) \\ I_{E2} &= \Delta y_E = f_2(p_x, p_y, p_z;\ \delta x, \delta y, \delta z, \delta t) \\ I_{E3} &= \Delta t_E = f_3(p_x, p_y, p_z;\ \delta x, \delta y, \delta z, \delta t) \end{aligned} \tag{1}$$

For the following discussion it is convenient to linearise Equation (1) around the point $(\vec{p}_0, \delta\vec{r}_0 = \vec{0},\ \delta t_0 = 0)$.

$$\begin{pmatrix} \Delta x_E \\ \Delta y_E \\ \Delta t_E \end{pmatrix} \approx \begin{pmatrix} \Delta x_{E0} \\ \Delta y_{E0} \\ \Delta t_{E0} \end{pmatrix} + \hat{J}(\vec{p}_0, \delta\vec{r}_0 = \vec{0}, \delta t_0 = 0) \begin{pmatrix} \vec{p} - \vec{p}_0 \\ \delta\vec{r} \\ \delta t \end{pmatrix} \tag{2a}$$

Here $\hat{J}$ is the 3×7 jacobian matrix with the elements $j_{ik} = (\partial I_i / \partial q_k)$ with the vector $\vec{q}$ summarising all seven independent variables of Equation ((1) $(1 \le i \le 3,\ 1 \le k \le 7)$. Inspection of this Equation (2a) leads one to formulate several desiderata for the elements of the jacobian matrix $\hat{J}$:

(1) The 3×3 submatrix containing the partial derivatives with respect to the components of $\vec{p}$ – henceforth referred to as the momentum dispersion matrix $\hat{M}$ – would best be diagonal and its elements as large as possible. Diagonality is a prerequisite for straightforward data analysis while the values of the coefficients directly relate to the sensitivity of the method.
(2) The remaining 3×4 matrix $\hat{J}_\delta$ responsible for the experimental uncertainties – from now on called σ_{Ex}, σ_{Ey}, σ_{Et} – should contain only zeros. The smaller the values, the less experimental uncertainties affect the determination of the momentum vector components, thus increasing the *resolution* of the method.
(3) If (1) cannot be granted, the determinant of the momentum dispersion matrix must not be zero, i.e. $\hat{M}$ should be invertible for all $\vec{p}_0$ – having in mind that the linearisation is not necessarily a valid assumption.
(4) The elements of M should not vary with $\vec{p}_0$.

In real life not all of this can be realised at once, but one can suggest two general concepts how to minimise the influence of the uncertainties in the initial conditions on the image vector $\vec{I}$:

(1) Minimise the uncertainties: This can be accomplished by decreasing the source volume, e.g. by tighter focussing of the laser if the optical ionisation process is nonlinear. Alternatively, one can cut the molecular beam into a very narrow sheet by employing a narrow slit after the skimmer in connection with a shorter laser pulse in order to minimise the temporal uncertainty.
(2) Minimise the respective partial derivatives $(\partial I_i/\partial \delta r_j)$ and $(\partial I_i/\partial \delta t)$ in the 3×4 submatrix $\hat{J}_\delta$ by employing inhomogeneous electrical fields.

The first strategy has its limitations because the number of molecules is reduced by reducing the volume if the density is constant.

The second strategy has the drawback that $\hat{M}$ will in general not be diagonal anymore and its elements become dependent on $\vec{p}_0$ which makes the analysis less straightforward. Furthermore, uncertainties in one dimension, e.g. δy, will affect experimental uncertainties in another, e.g. σ_{Et}.

Therefore, a combination of both strategies should be applied in a manner to fit the individual process under investigation.

For the following discussion it will be useful to rewrite Equation (2a) using the assumption that experiments are run in a way that $\hat{M}$ is not affected by the random source position.

$$\begin{pmatrix} \Delta x \\ \Delta y \\ \Delta t \end{pmatrix} + \begin{pmatrix} \delta \Delta x_E \\ \delta \Delta y_E \\ \delta \Delta t_E \end{pmatrix} \approx \left[\begin{pmatrix} \Delta x_0 \\ \Delta y_0 \\ \Delta t_0 \end{pmatrix} + \hat{M}(\vec{p}_0)(\vec{p} - \vec{p}_o) \right] + \left[\hat{J}_\delta(\vec{p}_0, \delta\vec{r}_0 = \vec{0}, \delta t_0 = 0) \begin{pmatrix} \delta\vec{r} \\ \delta t \end{pmatrix} \right] \tag{2b}$$

The first vector on the left-hand side of Equation (2b) is a clean image vector without any random contribution represented by the term in the first square brackets. The second vector summarises the experimental random contribution from the uncontrolled initial conditions represented by the second square brackets. The distribution of the individual random shifts $\delta\vec{r}$ and δt result in distributions of the experimental random shifts δI_{Ei} that we will characterise by their standard deviations σ_{Ex}, σ_{Ey} and σ_{Et} which are the above introduced experimental uncertainties. Please note that Equation (2b) also indicates that these depend on the components of the momentum vector $\vec{p}_0$, which will be discussed in Section 2.3.

2.1.2. *Sensitivity: the momentum dispersion matrix* $\hat{M}$

Generally, the relationship between a variation in the clean image vector $\mathrm{d}\vec{I} = (\mathrm{d}\Delta x, \mathrm{d}\Delta y, \mathrm{d}\Delta t)$ and the initial product momentum vector $\mathrm{d}\vec{p} = (\mathrm{d}p_x, \mathrm{d}p_y, \mathrm{d}p_z)$ can be very complex, in particular if pathological acceleration fields are used. Since this is not favourable as stated in desideratum (4) above, the experimental conditions are often such that $\hat{M}$ does not depend too strongly on $\vec{p}$, e.g. if a linear dependence between the radial component in the detector plane and the corresponding component $p_r = (p_x^2 + p_y^2)^{1/2}$ is

a good approximation. But for the sake of the comparability of different techniques we may assume a global momentum dispersion matrix such that:

$$\vec{I} = \hat{M}\vec{p} \tag{3}$$

with $\hat{M}$ being a diagonal matrix. This is the case if the point of impact to a first approximation is not a function of p_z and the acceleration field has no radial components. These conditions are most perfectly met in 2D ion imaging with energy focussing, since here the TOF is so narrow that $(x, y) = (p_x, p_y) \cdot t_0$ is an excellent approximation. In conventional 3D ion imaging for example, the radial component also depends on the p_z component as $(x, y) = (p_x, p_y) \cdot (t_0 + \text{const} \cdot p_z)$, thus yielding $\vec{p}$ dependent partial derivatives: $\partial x/\partial p_x = t_0 + \text{const} \cdot p_z$ and $\partial x/\partial p_z = \text{const} \cdot p_x$. However, in order to compare the techniques, the diagonal element contains enough information on how sensitive the components of the image vector are to variations of the initial momentum vector $\vec{p}$.

A more intuitive quantity is the closely related speed dispersion matrix which is obtained by simply dividing all coefficients of the $\hat{M}$ matrix by the mass of the detected particle. Speed dispersions are measured in units of s^2/m and s, respectively, or, more conveniently for the experimentalist, in ns/ms and μm/ms. The speed dispersion coefficients tell us how broad the TOF profile (in ns) and how large the image on the detector (in μm) will be for a given initial speed of the particle (in m/s).

Another point is that if components in Equation (3) are separable from the rest of the variables, i.e. if $\hat{M}$ is diagonal for a certain subspace, useful information can be obtained from the measurement of only one or two components of the image vector $\vec{I}$. This situation is prerequisite for any reduced dimension imaging experiment. Some typical examples of diagonal dispersion coefficients are compiled in Table 2.

2.2. *The road towards three dimensions*

Table 1 shows an overview of the image vector components containing relevant information for 3D and different variants of reduced dimensionality imaging schemes. The latter is discussed in more detail in the following sections.

2.2.1. *Conventional TOF mass spectrometry*

In conventional TOF mass spectrometry the detector cannot discriminate impact positions, only t is measured, and the mass resolution $m/\Delta m$ is sought to be optimised.

Table 1. Overview of the relevant image vector components for various 3D and reduced dimensionality imaging schemes. The measured image vector components are marked by X.

	Δx	Δy	Δt
TOF mass spectrometry ('0D') [7]	–	–	–
1D TOF imaging [8]	–	–	X
2D imaging [2]	X	X	–
3D imaging [9]	X	X	X

The particle detector normally consists of a secondary electron multiplier, nowadays commonly a micro-channel plate (MCP) [6] coupled to an anode integrating the electronic signal from the rear side of the MCP over the total surface (x, y) of the anode. Different masses m will arrive at the detector at different times t_0. Since Δx and Δy are not measured and the $\hat{M}$ matrix is diagonal, the only relevant relationship in Equation (3) remains

$$\Delta t = M_{tz} \cdot p_z. \tag{4}$$

For optimum mass resolution, Δt should be as small as possible, ideally equal to 0 (which would result in infinitely large mass resolution). Hence, M_{tz} must be made as small as possible which is the concept of energy focussing. It can be achieved by using a combination of two homogeneous acceleration fields with a field-free drift region in the TOF spectrometer. This design was first described by Wiley and McLaren who called the two homogeneous fields the extraction and the acceleration field [7]. The very good mass resolution quickly made the Wiley–McLaren design the standard TOF spectrometer in laboratories world wide.

Table 1 shows that none of the image vector components is measured in TOF mass spectrometry. Two of the three image vector components are not monitored at all and the information on the third one is eliminated by a clever electric field design. Consequently, from an imaging point of view, the Wiley–McLaren TOF spectrometer can be called a zero-dimensional imaging machine.

2.2.2. *Measuring time: reduction to 1D imaging*

The philosophy of 1D imaging is in parts identical to the philosophy of TOF mass spectrometry. In both cases a time-resolving particle detector is used which is not position-sensitive, i.e. Δt is being measured, while Δx and Δy are not (Table 1). However, there is a crucial difference between the mass spectroscopist and the imager: In 1D imaging one wants to maximise the measurable quantity Δt for a given p_z, i.e. M_{tz} should be as large as possible:

$$p_z = \Delta t / M_{tz} \tag{5}$$

Clearly, this cannot be achieved with a Wiley–McLaren spectrometer under energy focussing conditions. Either, the electric fields have to be adjusted according to the requirements of 1D imaging, or the spectrometer design has to be modified. In fact, the latter approach has the following advantages. (1) A single homogeneous field in combination with a drift region twice as long as the acceleration region yields large M_{tz} coefficients which are independent of p_z, in contrast to the Wiley–McLaren design. (2) The TOF profile is strictly symmetric around t_0, and t_0 itself is independent of $\vec{p}$. (3) The spectrometer yields spatial focussing for the z axis eliminating the influence of small laser shifts on the TOF. (4) M_{tz} can be calculated from the length of the acceleration region s and the average TOF t_0 [8]:

$$M_{tz} = \frac{3t_0^2}{8ms} \tag{6}$$

For typical values ($s = 0.2\,\text{m}$, $t_0 = 7\,\mu\text{s}$) one obtains a speed dispersion of *ca* 0.1 ns/ms, i.e. a product speed of 1000 m/s will give rise to a TOF profile with a total width of 200 ns.

For $t_0 = 10\,\mu s$ the values double, and one obtains $M_{tz} = 0.2\,ns/ms$ with a total width of the TOF profile of 400 ns for a speed of 1000 m/s. If time can be measured with a 1 ns precision this speed dispersion value will result in a speed resolution of 0.25%.

By rotating the polarisation vector of the initiating laser Δt will be a measure for different components of the product momentum vector in the polarisation vector based coordinate system (X, Y, Z). If additionally, the distribution of the product momentum vectors is cylindrically symmetric about the polarisation vector of the initiating laser, the third component of the product momentum vector does not carry any additional information, and with two consecutive measurements the full 3D product momentum vector distribution may be reconstructed from 1D imaging measurements.

2.2.3. *Measuring position: reduction to 2D imaging*

The first realisation of a 2D imaging experiment in reaction dynamics was reported by Chandler and Houston [2]. They replaced the surface integrating anode by a position sensitive, but time integrating phosphor screen. The 2D image on the phosphor screen was photographed by a suitable camera, nowadays almost always a charge-coupled device (CCD) camera. Now, Δx and Δy were measured instead of Δt (Table 1), and with a diagonal $\hat{M}$ matrix the relevant relationships from Equation (3) are

$$p_x = \Delta x / M_{xx} \tag{7a}$$

$$p_y = \Delta y / M_{yy} \tag{7b}$$

For well-behaved fields, M_{xx} and M_{yy} are equal to each other, constant and independent of the product momentum vector. For a good momentum resolution M_{xx} and M_{yy} should be as large as possible, the limiting factor being the detector radius R_D which must be larger than Δx and Δy.

For homogeneous fields, the momentum dispersion is calculated to be $M_{xx} = M_{yy} = m/t_0$. For $t_0 = 7\,\mu s$ one obtains a speed dispersion of approximately $7\,\mu m/ms$, with maximum measurable speeds of 2800 m/s for a 40 mm diameter detector and 4900 m/s for a 70 mm diameter detector. A product speed of 1000 m/s will give rise to an image diameter of 14 mm. If position can be measured with a 20 μm precision [1] this speed dispersion value will result in a speed resolution of 0.1%.

2.2.4. *Measuring time and position: full 3D imaging*

We have shown before that 3D imaging requires the simultaneous measurement of all three components of the imaging vector $\vec{I} = (\Delta x, \Delta y, \Delta t)$ with large sensitivity and accuracy. Thus, at the heart of 3D imaging lies a highly sophisticated position sensitive particle detector (PSD) which must be capable of simultaneously measuring the time as well as the position of an impinging particle. Two conceptually different strategies might be followed in order to achieve this goal. One might add space resolution to 1D TOF imaging or one might add time resolution to 2D imaging. As will be discussed in more detail below, the first approach relies on using MCPs in combination with delay line anodes [9,10], the second one on using MCPs in combination with phosphor screens coupled to a multiple exposure CCD camera [11].

Since the lower dimensionality imaging techniques discussed above focus on subsets of the vector Equation (3) and of the momentum dispersion matrix $\hat{M}$, they need not worry about sensitivity and resolution in those dimensions which are not observed. On the contrary, by a clever experimental design one can enhance the performance for the desired dimensions at the cost of the unwanted ones. Since this approach is not feasible for full 3D imaging, we need to carefully asses the resolution issue for imaging setups in general and for 3D imaging setups in particular, before we proceed to discussing experimental realisations of 3D imaging techniques.

In particular, any measures aimed at improving the resolution in any one dimension e.g. by using inhomogeneous focussing fields will normally increase the values of those elements of the 3×4 matrix $\hat{J}_\delta$ in Equation (2b) that mediate between the different dimensions of $\vec{I}$ and consequently decrease the resolution in these dimensions as well as affect all other elements in $\hat{M}$. This non-trivial interplay between different dimensions is the crucial issue to be assessed when trying to optimise 3D imaging resolution and deserves the thorough discussion following underneath. To this end one needs to further discuss the typical uncertainty sources summarised in $\hat{J}_\delta$ and to quantify their effects on the image vector $\vec{I}$ using the relationship in Equations (2).

2.3. *Sources of uncertainty: resolution optimisation*

Above, we have obtained a rough idea on the sensitivities that can be obtained in today's state of the art imaging experiments and the influence of the initial conditions not being controlled under molecular beam conditions. We do know that we should work with large momentum dispersion coefficients, and we do know that life becomes easy if the momentum dispersion matrix is diagonal and its coefficients are independent of the momentum vector $\vec{p}$. However, we have not yet discussed the issue of resolution achievable in imaging experiments.

For assessing the resolution of an imaging experiment one needs to distinguish between conceptually different uncertainties sources which arise in a typical imaging setup. By typical imaging setup we refer to a setup that is employed for the study of chemical processes, i.e. where product energies to be resolved lie in the range of a few electron volts or below. Additionally, we will assume a spectrometer setup in which the initiating laser propagates in y direction, i.e. perpendicularly to the spectrometer axis which is the most common realisation for reaction dynamics imaging experiments.

We discuss uncertainties only that we consider to be unavoidable. How can their effect be minimised in order to push the resolution of an imaging experiment to the limit from a principal point of view? Sources of uncertainty which are not being considered in this context are avoidable imperfections in the layout of the experiment, such as e.g. uncertainties in the product momentum vector $\vec{p}$ itself owing to insufficient cooling of precursor molecules, imperfect field design, space charge effects owing to large ion densities in the ionisation region, non-negligible rotational excitation of the precursor molecules and the like. It must be noted in this context that for the investigation of bimolecular reactions, control of initial conditions, in particular of the initial momentum vector $\vec{p}$, is normally the most difficult problem to solve.

The two general types of uncertainties that need to be considered for evaluating the resolution of an imaging experiment are the detector uncertainty σ_{D} and the experimental uncertainty σ_{E}.

2.3.1. *Detector uncertainty* σ_D

One unavoidable uncertainty source is the limited performance of the employed detector assembly consisting of the detector itself, any data acquisition hardware and the data acquisition software. How precise can time and position be measured by the detector assembly? We will call these detector characteristics the detector uncertainty σ_{D}. Every dimension (x, y, t) will have its own detector uncertainty. However, it can be assumed that normally x and y space uncertainties will be identical ($\sigma_{\mathrm{D}x} = \sigma_{\mathrm{D}y} = \sigma_{\mathrm{D}r}$) whereas the detector time uncertainty $\sigma_{\mathrm{D}t}$ and the detector space uncertainty $\sigma_{\mathrm{D}r}$ might be substantially different from each other. Today, the space uncertainty of state of the art detector assemblies ranges from several 10 µm to a few 100 µm, depending on the type of detector used, whereas time uncertainty typically lies in the 100 ps to 1 ns range. Typical detector uncertainties σ_{D} are listed in Table 2 along with the corresponding sensitivities.

2.3.2. *Experimental uncertainty* σ_E

The second unavoidable uncertainty source is the limited experimental control over the start conditions. For a hypothetical reference particle one assumes a start position $x = y = z = 0$ and a start time $t = 0$ if one looks at the $\hat{M}$ matrix only. In reality, the particle will start at the position $(\delta x, \delta y, \delta z)$ at time δt. The components of the image vector not only depend on the initial product momentum vector $\vec{p} = (p_x, p_y, p_z)$, but also on the exact start position and on the exact start time. The distribution of the start condition uncertainties $(\delta x, \delta y, \delta z)$ and δt give rise to random distributions of the image according to Equations (1)–(3) introducing experimental uncertainties σ_{Ex}, σ_{Ey} and σ_{Et} on the image vector components.

In order to fully utilise the resolving powers of our detector, we need to either sufficiently reduce the uncertainties $(\delta x, \delta y, \delta z)$ and δt of the start conditions themselves or minimise the experimental uncertainty σ_E for which the start condition uncertainties are responsible for. Ideally, the experimental uncertainty should be of the same order of magnitude as the detector uncertainty σ_D: $\sigma_{Ex} \approx \sigma_{Dr}$, $\sigma_{Ey} \approx \sigma_{Dr}$ and $\sigma_{Et} \approx \sigma_{Dt}$. As long as start condition uncertainties can be assumed to be small, it is justified to focus one's attention primarily to the discussion of 'diagonal' effects, i.e. the influence of δt and δz on Δt and to the influence of δx on Δx and δy on Δy. It will be shown below, however, that when approaching the optimal resolution design non-diagonal effects become noticeable.

The main source for δx and δz uncertainties is the width of the laser focus in the ionisation region. By tight focussing this width can be reduced to values of a few 10 µm. Additionally, both the single field configuration and the Wiley–McLaren two field configuration will normally be used under space focussing conditions where the effect of the δz uncertainty as well as that of unavoidable shifts in the laser pathway on the TOC is essentially eliminated. For the single field setup space focussing is achieved when the drift region is twice as long as the acceleration region whereas in the Wiley–McLaren design space focussing is obtained for adequately adjusted strengths of the extraction and the acceleration field. Moreover, when using nanosecond lasers, the uncertainty in the Δt

Table 2. Uncertainty and resolution of several imaging setups. The investigated process is assumed to be the two-photon Rydberg excitation of molecular oxygen at 225 nm with $t_0 = 3\,\mu s$ resulting in O atoms with a maximum speed of ca 6000 m/s [12]. Quantities are explained in the text. (A: 1D TOF [8], B: 2D imaging, non-VMI [12], C: 2D VMI [12], D: 3D imaging, non-VMI [9], E: 3D VMI [11] and F: 3D VMI [10]).

	A	B[a]	C	D	E	F
mM_{xx} [μm/ms]		3	3	3	3	2.2
mM_{yy} [μm/ms]		3	3	3	3	2.2
mM_{tz} [ps/ms]	6			24	1.7	32
σ_{Dx} (μm)		20[b]	20[b]	100[c]	20[b]	100[c]
σ_{Dy} (μm)		20[b]	20[b]	100[c]	20[b]	100[c]
σ_{Dt} (ns)	<0.2[d]			<0.2[d]	>1.2[e]	<0.2[d]
σ_{Ex}[f] (μm)		17	17	17	17	17
σ_{Ey} (μm)		2000[g]	300[i]	2000[g,h]	300[i]	18
σ_{Et} (ns)	5			5	$<10^{-3}$	5
σ_x[j] (μm)		22	22	102	22	102
σ_y[j] (μm)		2000	300	2003	300	102
σ_t[j] (ns)	5			5	>1.2	5
$[\sigma_{px}/m]$[k] (ms^{-1})		7.3	7.3	34	7.3	46
$[\sigma_{py}/m]$[k] (ms^{-1})		667	100	668	100	46
$[\sigma_{pz}/m]$[k] (ms^{-1})	833			208	706	156
$[\sigma_p/m]$[l] (ms^{-1})				700	713	169
σ_p/p[m]	13.9% (1D)	11.1% (2D)	1.7% (2D)	11.7%	11.9%	2.8%

Notes: [a]Assuming the spectrometer geometry of ref. [12] without Einzel lens.
[b]Value taken from p. 29 of ref. [1].
[c]Value taken from ref. [10].
[d]Value taken from Table 1 of ref. [238].
[e]Value taken from Table 1 of ref. [11]. This value must be regarded as a lower limit because for its determination the TOF profiles were erroneously assumed to be symmetric.
[f]$\sigma_x \approx 2w_0 = \frac{4\lambda f}{\pi d}$ is taken to be twice the focus radius w_0 of a tightly focussed Gaussian beam (beam diameter $d = 2$ mm, wavelength $\lambda = 225$ nm, focus length $f = 12$ cm).
[g]$\sigma_y \approx 2z_0 = \frac{2\pi w_0^2}{\lambda}$ is taken to be twice the Rayleigh length of a tightly focussed Gaussian beam (focus diameter $2w_0 = 17\,\mu$m, wavelength $\lambda = 225$ nm).
[h]We have previously reported an experimental value of $\sigma_y = 3.2$ mm for the real 3D imaging experiment. The value 2 μm was chosen to discuss resolution for comparable conditions. Note that in the text of this work the performance of 3D velocity mapping has been investigated for $\sigma_y = 8$ mm.
[i]value taken from Figure 7 of ref. [12].
[j]Equation (8).
[k]Equation (12).
[l]Equation (10a).
[m]Equation (10b).

component of the image vector will be dominated by the laser pulse duration and not by the position uncertainty δz as can be seen in Table 2. In short, δx and δz uncertainties are usually not of major concern in imaging experiments.

The situation is very different for the remaining spatial uncertainty δy. First, δy now represents the length of the laser focus which is much larger than its width. Typically, δy will be in the range of one to several mm. Second, no space focussing for the y direction is available in the standard single-field or Wiley–McLaren setups. If the δy uncertainty is carried over to the Δy component of the image vector, i.e. if $\sigma_{Ey} = \delta y$, then σ_{Ey} will be one

or two orders of magnitude larger than the detector space resolution σ_{Dr} which is not acceptable. Note that for 1D imaging or for TOF mass spectroscopy the δy uncertainty is irrelevant if only diagonal uncertainty propagation is assumed, since the Δy component of the image vector is not monitored. However, for 2D imaging and of course for 3D Imaging δy does matter.

With the exception of imaging experiments relying on pulsed electric fields, any start time uncertainty δt is directly transferred onto the Δt component of the image vector, i.e. $\sigma_{Et} = \delta t$, if the δz contribution is negligible. The main reason for start time uncertainty is the pulse duration of the pulsed laser. In view of a detector time resolution of roughly 1 ns, a typical 5 ns pulse duration of a Nd : YAG laser pumped dye laser may seem tolerable, in particular since multi-photon excitation with frequency doubled light is likely to occur in a shorter time period than 5 ns, owing to the threshold behaviour of lasing, frequency doubling and multi-photon excitation leading to a compression of the original pulse width. Nevertheless, the use of excimer lasers for imaging experiments must be discouraged because of their typical pulse duration of more than 10 ns. Ultra-short laser pulses in the sub-nanosecond regime will basically eliminate any δt uncertainty. However, the requirement of quantum state selection of the products often forbids the use of such lasers. Additionally, for femtosecond lasers at least, one needs to be aware of the fact that a 200 fs laser initiating a process with excess energy of 1 eV will introduce a 2% uncertainty in the excess energy due to the Heisenberg uncertainty principle. For these reasons, Nd : YAG laser based imaging experiments are nowadays very common.

2.3.3. *Total uncertainty* σ

Total uncertainties are contributed to by detector and experimental uncertainties:

$$\sigma_i = \sqrt{\sigma_{Di}^2 + \sigma_{Ei}^2} \quad \text{with } i = x, y, t. \tag{8}$$

Uncertainty components are combined in an uncertainty vector $\vec{\sigma} = (\sigma_x, \sigma_y, \sigma_t)$. Detector uncertainties are detector properties. Once a detector has been chosen, detector uncertainties are known quantities which guide the experimenter through the design of an imaging setup. In order to fully exploit the detector performance, experimental uncertainties must be matched to detector uncertainties component wise.

Estimated and reported values for the total uncertainty vector $\vec{\sigma}$ are listed in Table 2 with the two-photon dissociation of molecular oxygen at 225 nm as the reference experiment, along with experimental uncertainties σ_E, detector uncertainties σ_D and (diagonal) sensitivities M. Note that the values reported in Table 2 do not represent the ultimately achievable resolution, but are intended to compare different variants of 3D imaging and to demonstrate the progress achieved by the introduction of velocity mapping conditions. They also represent rather typical values. However, for achieving ultimate resolution in an imaging experiment, the experiment must be adjusted to match the properties of the studied products.

2.3.4. *The crucial role of* σ_{Ey}

From the preceding discussion it is clear that, apart from the laser pulse duration, the experimental uncertainty σ_{Ey} is the main problem to worry about because it is the only

uncertainty where $\sigma_E \gg \sigma_D$. From Table 1 one can see that the σ_{Ey} issue is important only for 2D and 3D imaging experiments. Several strategies have been realised to reduce its value and let it match the detector uncertainty σ_{Dy}.

A likewise elegant and effective and by far the most popular method to reduce the value of σ_{Ey} for a given uncertainty δy is the VMI technique introduced by Eppink and Parker [12] in which particles with the same velocity are projected onto the same position on the detector. Basically, this concept uses electrostatic focussing of ions accelerated in a TOF spectrometer of Wiley–McLaren design where the grids separating extraction, acceleration and drift regions of the spectrometer have been removed. The corresponding curved equipotential surfaces and the absence of disturbing grids provided y space focussing conditions. For 2D imaging purposes this approach is the best way to push the resolution to its limit. Eppink and Parker reported angle-dependent 'deblurring factors' ranging from 5 to 34 meaning that an initial δy uncertainty of 3 mm will be reduced to spot sizes on the detector surface between 0.6 and 0.088 mm [12]. Another advantage is that a relatively large volume can be sampled by the laser focus without deterioration of the resolution so that lower particle densities can be accepted without risking too low count rates at the detector. Lower particle densities in turn have the advantage of avoiding the risk of space charge affecting the original particle momenta. The superb y resolution of this method requires a price to be paid for, however. The inhomogeneous fields used in this setup let the non-diagonal elements in the x, y subset of the momentum dispersion matrix be non-zero, and the resolution gain in Δy direction is accompanied by a resolution loss in Δt. In order to eliminate uncertainties in the y direction, in Parker and Eppink's approach all efforts for securing a good z resolution are sacrificed. The TOF peak broadening is deformed to such an extent that a 2D image filling a conventional 40 mm or 70 mm diameter position sensitive detector has a temporal width of only several nanoseconds. This behaviour has consequently been termed 'crushing' or more intuitively 'pan-caking' of the ion sphere. Consequently, in combination with nanosecond pulsed lasers, as discussed above and considering the typical detector time resolution σ_{Dy}, the information about the third dimension of the velocity vector is completely lost.

The VMI scheme reported by Eppink and Parker therefore cannot be used in 3D imaging without major modification. Another strategy that can be used is not to reduce σ_{Ey}, the uncertainty propagation of δy on Δy, but to reduce the uncertainty in δy itself. If the molecular beam carrying the precursor molecules is geometrically narrowed by using narrow slits and if this narrowed beam is propagated along the x or the z axis, then δy is determined by the small width of the molecular beam rather than by the length of the laser focus. This method has successfully been demonstrated in a 3D imaging experiment for H^+ ions resulting from the intriguingly complex photodissociation of HCl [13]. The advantage of this approach is that maintaining well-behaved electric fields leaves the speed dispersion matrix diagonal. A disadvantage is that owing to the narrowed molecular beam the total number of precursor molecules and thus the count rate at the detector is reduced.

An approach avoiding this disadvantage is to start from the conventional 3D imaging setup [9] and to add ion optics in order to improve spatial resolution without damaging the temporal resolution more than tolerable. To this end we have inserted an Einzel lens into the acceleration region of the spectrometer such that (1) the diagonality of the momentum dispersion matrix was preserved well enough to leave off-diagonal elements of minor importance, (2) that the diagonal elements M_{xx}, M_{yy} and M_{tz} are nearly constant, yielding

nearly linear relationships between p_x and Δx, p_y and Δy, and between p_z and Δt and (3) the 'clean' mapping of $\vec{p}$ onto $\vec{I}$ shown in its locally linearised form in Equations (2) is bijective. The fields that comply with these conditions we call well-behaved. Thus, a comparatively straightforward data analysis remains possible, and at the same time velocity mapping conditions are established [10]. Even for well-behaved inhomogeneous fields, however, the exact action of the ion optics can only be investigated by simulated ion trajectories and the role of non-diagonal elements of the dispersion matrix need to be taken into account. Ideally, the latter two approaches can be combined.

2.4. *3D imaging experimental design*

2.4.1. *General considerations*

The resolution issue in TOC mass spectroscopy and in TOC imaging spectroscopy has always been a crucial one. Depending on the operation mode and on the quantity of interest, improving resolution requires different strategies leading to very different philosophies and solutions. The strategy for optimising resolving power of a 3D imaging experiment (velocity mapping or not) must be to establish conditions where the resolution σ_{pi} for all three components of the momentum vector ($i = x, y, z$) are equally good.

$$\sigma_{px} = \sigma_{py} = \sigma_{pz} \tag{9}$$

where σ_{pi} denotes the absolute momentum uncertainty of the momentum vector component p_i. The three resolution components form a resolution vector $\vec{\sigma}_p = (\sigma_{px}, \sigma_{py}, \sigma_{pz})$ with its magnitude σ_{px} as absolute momentum resolution

$$\sigma_p = \sqrt{\sigma_{px}^2 + \sigma_{py}^2 + \sigma_{pz}^2} \tag{10a}$$

and σ_p/p as relative momentum resolution:

$$\frac{\sigma_p}{p} = \sqrt{\frac{\sigma_{px}^2 + \sigma_{py}^2 + \sigma_{pz}^2}{p_x^2 + p_y^2 + p_z^2}}. \tag{10b}$$

Since any evaluation procedure must rely on the $(\delta x, \delta y, \delta z)$ and δt to be zero, because the mapping in Equation (1) cannot be bijective, the total uncertainties in the image will transform to $\vec{\sigma}_p$ using the inverse functions ${I^{-1}}_i(p_x, p_y, p_z;\ 0, 0, 0, 0)$ (see Equation (1)). Especially, if the coefficients of the momentum dispersion matrix are independent of the momentum vector $\vec{p}$, then the total uncertainties and momentum resolution are related to each other by

$$\vec{\sigma} = \hat{J}_\delta \begin{pmatrix} \delta\vec{r} \\ \delta t \end{pmatrix} \tag{11a}$$

$$\vec{\sigma}_p = \hat{M}^{-1}\vec{\sigma}. \tag{11b}$$

Equations (11) are the core equations for assessing the resolving power of an imaging experiment. Random uncertainties in starting conditions are transferred into a mean imaging vector uncertainty $\vec{\sigma}$ by action of the matrix $\hat{J}_\delta$. The analysis procedure necessarily

converts these imaging vector uncertainties to momentum vector uncertainties $\vec{\sigma}_p$ owing to the momentum dispersion matrix $\hat{M}$. Thus, random uncertainties in starting conditions, the momentum dispersion matrix $\hat{M}$, and the uncertainty matrix $\hat{J}_\delta$ act together to limit the resolution of the imaging experiment. Optimal balancing of these quantities is the ultimate goal of the imaging experiment designer.

If uncertainties are small, non-diagonal contributions of the $\hat{M}$ matrix can be neglected and the resolution in any dimension is obtained by simply dividing the uncertainties σ by the sensitivities given by the diagonal momentum dispersion matrix coefficients M. For $i = x, y$ one obtains

$$\sigma_{pi} = \sigma_i / M_{ii}. \tag{12a}$$

Similarly, the maximum momentum resolution σ_{pz} in z direction is determined by the total z uncertainty σ_z and the matrix coefficient M_{tz}:

$$\sigma_{pz} = \sigma_t / M_{tz}. \tag{12b}$$

Once a given detector with uncertainties σ_D has been chosen, one must adjust experimental conditions in such a way that total uncertainties σ are of the same order of magnitude as detector uncertainties σ_D alone. This requires that experimental uncertainties σ_E do not exceed the detector uncertainties. Then sensitivities, i.e. the coefficients in the momentum dispersion matrix must be adjusted such that Equations (9) and (12) are satisfied simultaneously. It must be noted that only the corresponding ratios of Equation (12) need to be equal to one another and not the uncertainty components or the dispersion matrix coefficients themselves. Thus, differing detector resolution can be compensated for by corresponding adjustment of dispersion matrix elements and vice versa.

Generally, if no constraints on the employed electric fields are made, there is no other way than to run a sufficiently large number of simulated ion trajectories in the relevant momentum vector range to characterise the behaviour of the imaging setup with respect to Equation (11). Even in the case of well-behaved fields, it is advisable to proceed like this, in order to recognise where the deviation from well-behaving becomes unacceptably large.

For common cases and well-behaved fields, however, some simple conclusions can be drawn without too much effort. First, not all quantities of Equations (9)–(12) are likewise adjustable. e.g., in x direction the experimental uncertainty $\sigma_{\mathrm{E}x}$ can normally be assumed to be negligible. Consequently, the total uncertainty σ_x is mainly determined by the detector uncertainty $\sigma_{\mathrm{D}x}$. Second, the size of the PSD sets an upper limit to the diagonal spatial dispersion coefficients M_{ii} $(i = x, y)$. If ion fly-out is to be prevented, then the product of the maximum possible particle momentum p_max with the momentum dispersion coefficient must not exceed the detector radius R_D: $p_\mathrm{max} M_{ii} \leq R_\mathrm{D}$. This condition merely accounts for the fact that the detector size and the maximum speed of the particles to be monitored determine the maximum TOC t_0 for which all particles will still hit the detector. In fact, the spatial speed dispersion turns out to be nothing else than exactly this TOC t_0:

$$mM_{ii} = R_D / v_\mathrm{max} = t_0 \tag{13}$$

with $i = x, y$. Realistically, product kinetic energies in reaction dynamics experiments are of the order of an electron volt or less, corresponding to a speed range from 10^3 to 10^4 m/s, depending on the particle mass. For common detector sizes of 40 or 70 mm diameter,

one obtains therefore typical TOF ranging from 2 to 10 μs, corresponding to spatial speed dispersions of 2μm/(m/s) to −10 μm/(m/s).

For the x component, inserting Equation (13) into Equation (12a) and assuming $\sigma_x = \sigma_{Dx} = \sigma_{Dr}$ one obtains the simple intuitive relationship

$$\frac{\sigma_{px}}{p} = \frac{\sigma_{Dr}}{R_D}. \tag{14a}$$

This result may seem trivial at first sight. It must be remembered, however, that Equation (14a) holds only if electric fields are well-behaved (Section 2.3.2.), and if the experimental uncertainty σ_{Ey} is negligibly small compared to the detector uncertainty $\sigma_{Dy} = \sigma_{Dr}$.

While for the x component these conditions are normally fulfilled by default, this is generally not the case for the y and the z components, and one cannot assume the resolution issue for y and z to be similarly trivial as for x. However, the x resolution sets an expectation value which should be reached for careful design of an imaging setup for y and z dimensions as well (Equation (9)).

For the y dimension the case is conceptually simple. One just needs to reduce the total uncertainty σ_y to σ_{Dy}. Several strategies for achieving this have been discussed before. One needs to be careful about non-diagonal effects that σ_{Ey} reduction has on σ_x and σ_t, particularly if the x resolution derived from Equation (14a) is used as a benchmark value.

For z (or t) resolution, the case is slightly different. If a nanosecond laser is used for the process photoinitiation, then the uncertainty σ_t is not given by the detector uncertainty σ_{Dt}, but rather by the laser pulse duration τ_L. The role of the detector diameter $2R_D$ (which was assumed to be equal to the diameter of the ion sphere impinging on the detector surface) is now played by the total width of the temporal TOF profile 2T. Then, the equivalent to Equation (14a) for the z component reads:

$$\frac{\sigma_{pz}}{p} = \frac{\tau_L}{T}. \tag{14b}$$

In fact Equation (14b) sets a lower limit for the TOF peak broadening 2T that must occur for a given imaging setup, in order to warrant similar resolution for all three momentum components of the product particle.

As a first approximation, Equations (14) boil down to a set of three simple rules of thumb which need to be fulfilled simultaneously in a good 3D imaging setup:

- The relative momentum resolution in x direction is given by the ratio of the detector uncertainty σ_{Dr} and the detector radius R_D. For state of the art detectors this value lies in the range of a few tenths of a per cent.
- The detector uncertainty σ_{Dx} sets an upper limit for the experimental uncertainty σ_{Ey}:

$$\sigma_{Ey} \leq \sigma_{Ds}. \tag{15a}$$

- The laser pulse duration τ_L sets a lower limit for the TOF peak broadening T:

$$T \geq \frac{\tau_L R_D}{\sigma_{Ds}}. \tag{15b}$$

Simultaneously fulfilling Equations (15) is not a straightforward task. For example, the standard 2D VMI scheme reported by Eppink and Parker [12] satisfies Equation (15a), but fails to satisfy Equation (15b) while the original version of the 3D imaging setup [9] previously reported by the authors of this review complies with Equation (15b), but not with Equation (15a). To our understanding, the first and up to date the only 3D imaging setup ever reported fulfilling both Equations (15a) and (15b) simultaneously is the 3D VMI setup recently reported by us [10].

2.4.2. *The performance of 3D VMI*

Before discussing the performance characteristics of several selected imaging concepts, we would like to shortly describe the Braunschweig 3D VMI machine. The original experimental 3D imaging setup as well as its VMI modification relies on a single-field space focussing TOF spectrometer and has been described elsewhere in detail [9,10]. Briefly, it consists of an acceleration region which is attached to a field free drift region, with the acceleration region comprising 10 ring electrodes with an inner diameter of 106 mm. The supplied acceleration voltage is either split by nine 2 MΩ resistors in order to obtain a homogeneous electric field (ion imaging configuration), or it can be applied to the eighth electrode which is connected to the first electrode by an 11 MΩ resistor, with the remainder split again uniformly. In the latter case the electrodes 7, 8 and 9 serve as an Einzel lens and their field is superimposed by a homogeneous field (velocity mapping configuration). An important advantage of this configuration is that one can choose to run the spectrometer either in the homogeneous field mode or the Einzel lens mode by a simple switch. After having passed the TOF spectrometer, the ions are projected onto a PSD consisting of a double stage MCP assembly and a delay line anode (Roentdek) [14]. The eight signals from the four lines of the delay line are decoupled from the high DC voltage, differentially amplified by an eight channel differential amplifier, and finally recorded and analysed by a LeCroy 500 MHz oscilloscope (Waverunner 6050). The individual ion signals are fit by Gaussians in order to determine the centre of the electron cloud emerging from the MCP stack. From this the point of impact and the TOF for every ion detected are extracted. Detector uncertainties of $\sigma_{Dr} = 100\,\mu m$ and $\sigma_{Dt} = 300\,ps$ have been reported, and a momentum resolution $\sigma_p/p = 2.2\%$ has experimentally been determined [10]. This latter value is still subject to substantial improvement, if the spectrometer dimensions are accordingly increased.

In Table 2, we compare the performance characteristics of this machine with those of several other, conceptually different imaging techniques. Three of these are lower dimensionality (1D and 2D) imaging setups. These are our own space-focussing single-field 1D TOF setup [8] and the phosphor screen based 2D imaging setup by Eppink and Parker with and without velocity mapping conditions [12]. The other three are real 3D imaging experiments. Those are the phosphor screen based 3D VMI setup relying on Eppink–Parker focussing [11] and our own setup in the imaging and in the velocity mapping mode [9,10]. The performance of an imaging setup depends on the system that is being studied. In order to present an unbiased overview, here we refer to the experiment performed by Eppink and Parker who investigated the photodissociation of molecular oxygen following two-photon Rydberg excitation around 225 nm [12,15]. The maximum kinetic energy released when two ground state oxygen atoms are produced is 5.87 eV,

resulting in a maximum O atom speed of close to 6000 m/s [15]. Consequently, we have used a speed of 6000 m/s at a TOF of 3 μs for assessing the imaging performance of the six setups listed in Table 2. The initial start position uncertainty δy has been taken to be 2 mm, in accordance with the assumptions made by Eppink and Parker [12].

The spatial speed dispersion coefficients have been assumed to be equal to t_0, except for our 3D VMI experiment (F) where velocity map conditions lead to a 25% reduction of the image diameter on the detector when compared to the homogeneous field non-VMI conditions (D). In principle, this sensitivity and resolution limiting effect can be compensated for by decreasing the acceleration field strength accordingly. The reduction in image size goes along with a similarly large increase in TOF peak broadening.

Experimental uncertainties σ_{Ey} in the Eppink–Parker VMI configurations (C, E) are taken from reference [12]. They agree well with the reported deblurring factors [12]. Our own deblurring factor which has been calculated from ion trajectory simulations is much larger. In Figure 3 we present polar plots of the propagation of the δy start condition uncertainty onto the spatial σ_{Er} and temporal σ_{Et} uncertainties. The propagated δy uncertainties onto Δr and Δt image vector components have been normalised to the image size R on the detector surface and the TOF peak broadening T, respectively. Δr represents Δx or Δy components likewise, as electric fields do not depend on the azimuthal angle ϕ. The experimental uncertainty $\sigma_{Ey} = 18\,\mu m$ in the F column of Table 2 results from averaging the upper panel of Figure 3. The existence of non-zero non-diagonal contributions in the momentum dispersion matrix are easily identified by the effect of the initial δy uncertainty onto the Δt component of the image vector $\vec{I}$, as shown in the lower panel of Figure 3. Nevertheless, the uncertainty in Δt induced by the δy starting condition uncertainty propagation is significantly smaller than the laser pulse duration τ_L. Therefore, the experimental uncertainty σ_{Et} is still essentially determined by the laser pulse duration and the improvement in y resolution is essentially obtained at negligible cost for the other dimensions. Of course, this situation would be different, if a short pulse laser were used for process photoinitiation.

It is obvious from Table 2 that high resolution 3D imaging without velocity mapping conditions is not possible. The resolution increase when changing from non-VMI conditions to VMI conditions is substantial for 2D imaging (column B *versus* C) as well as for 3D imaging (column D *versus* F). It is also clearly seen that the desired balance between the three components of the resolution vector $\vec{\sigma}_p$ is best approximated by our 3D VMI setup (F). The remaining imbalance is mainly due to the application of the setup to unusually fast fragment from the O_2 dissociation. While the detector space resolution can be almost completely be utilised, the short TOF of only 3 μs results in a relatively small TOF peak broadening, so that in this case the pulse duration of the Nd : YAG laser has a deteriorating effect on the temporal resolution of our setup. For less energetic fragments a better balance between the resolution vector components will be achieved.

The performance of the 3D VMI setup (E) is significantly lower due to the poor resolution in the z component. In fact, while the spatial detector resolution of the phosphor screen is superior to the delay line anode by a factor 5, the use of the Parker–Eppink VMI conditions does not allow the temporal detector resolution to be fully used. Running the double exposure phosphor screen setup under the VMI conditions of reference [10] should greatly enhance its performance.

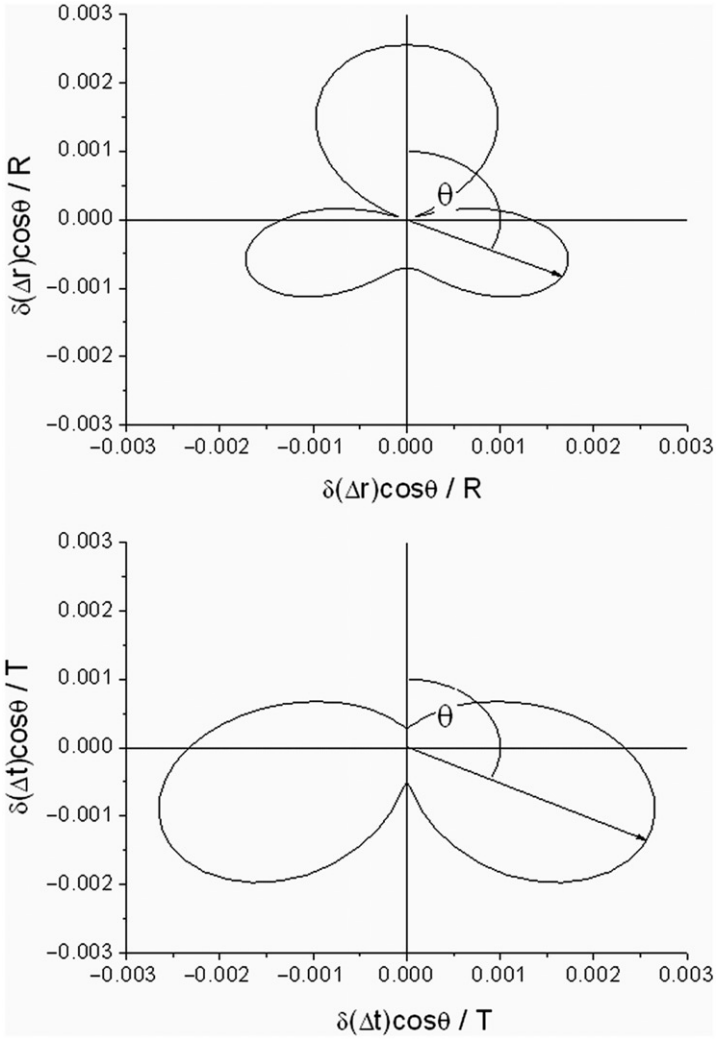

Figure 3. Polar plots showing the propagation of $\delta y = 2$ mm start condition uncertainty onto Δt and Δr image vector components for O atoms with initial speed of 6000 m/s at a total time of flight $t_0 = 3$ μs. The angle θ describes the angle of the initial velocity vector with the spectrometer axis. The image diameter on the detector surface is $2R = 26$ mm, and the total TOF peak broadening $2T = 383$ ns. Results are normalised to the image radius R and to the TOF peak broadening T, respectively.

2.5. *Applications of 3D imaging to reaction dynamics*

We do not comprehensively summarise 3D imaging applications from the very beginning, since the birthplace of 3D imaging was (nuclear and atomic) particle physics where applications of this technology must cope with very different conditions from those encountered in a reaction dynamics environment. Instead we focus on the application of the technology in chemical dynamics.

A comprehensive review of applications of 3D imaging in atomic physics relying on delay line technology has been given by Schmidt-Böcking *et al*. [16]. Early applications of the delay line technology for 3D imaging studies in reaction dynamics included work on benchmark systems as the photoionisation of nitric oxide (NO) at a laser wavelength of 226 nm and the Cl_2 photodissociation of molecular chlorine (Cl_2) at a dissociation wavelength of 355 nm. For these applications a superb speed resolution was demonstrated for the NO photoionisation process where an NO speed as low as 14 m/s could be determined from the measurements. This small speed corresponds to the ion recoil from the ejected electron, and it was for the first time that the ionisation recoil of a molecular species was observed experimentally [17,18]. Subsequently, several molecular fragmentation processes were studied by the characterisation of the 3D momentum distribution of Cl atoms, [19,20] namely the photodissociation of $COCl_2$, [21] $CSCl_2$, [22] $SOCl_2$ [23] and S_2Cl_2 [24]. In addition the complex competition between photoionisation and photodissociation of HCl has also been characterised [13,18,25].

The improved resolution of the 3D VMI setup was demonstrated for the first time in the reinvestigation of the competing ionisation and fragmentation processes in the HCl molecule after UV photoexcitation. A resolution enhancement of a factor of 4 was reported. Later, the technique was used to study the bimolecular reaction $O(^1D) + N_2O \rightarrow NO + NO$ [26].

As a further development, Doppler free monitoring of reaction products was added to the 3D imaging concept by Zare *et al*. [27]. The Doppler free detection scheme increases the detection sensitivity, thus allows for smaller laser intensities, reducing space charge effects and contribution of background signal. These improvements are especially valuable in the case of light (and correspondingly fast) products and low concentration products, i.e. in particular for the study of bimolecular reactions. Consequently this technique has been applied to the investigations of the hydrogen exchange reaction as the prototype benchmark chemical reaction $H + D_2 \rightarrow D + HD$ [28–30] and to its inelastic scattering equivalent: $H + D_2(v, J) \rightarrow H + D_2(v', J')$ [31]. Latest improvements consist of the introduction of a reflectron into the imaging setup allowing continuous TOF ion imaging and application to fragmentation [32].

As an alternative to delay line based 3D imaging setups, phosphor PSDs with a time sensitive read-out system have been utilised. For carefully selected phosphors, matching the time structure of the studied system, information about the impact time of a particle can be obtained by either monitoring the image on the phosphor screen with two independent cameras at slightly different times [33], or by one fast double exposure camera [11]. In both cases the start time for the exponential decay of the phosphorescence can be determined from the intensity ratio of the pixels belonging to the same event.

The first approach has been demonstrated for the photodissociation of H_2^+ in a conventional imaging experiment without the use of ion optics [33]. The second technique was applied to multi-photon ionisation and dissociation of molecular iodine [11] where the space resolution of the PSD was increased using the VMI scheme developed by Parker and Eppink [12]. However, the severe disturbance of ion arrival time at the detector due to the VMI conditions prevented the authors to obtain a time resolution in their experiment that would match the excellent space resolution (Table 1).

Coincidence techniques in particle physics as well as in reaction dynamics necessarily rely on the detection of 3D momenta of individual particles. Applied techniques are

therefore to a large extent very similar to the ones discussed in this review. Nevertheless, coincidence spectroscopy is not the subject of this work. Instead the interested reader is referred to the recent review by Continetti [34] who has extensively discussed the application of coincidence techniques to the study of the reaction dynamics of isolated molecules.

Ironically, most applications of 3D imaging have been performed on systems which exhibit cylindrical symmetry. In these cases, the principal advantage of 3D imaging cannot fully be exploited. Instead, the trade-offs which need to be settled for in order to balance the components of the resolution vector $\vec{\sigma}_p$ do not allow to realise the same high resolution that state of the art 2D VMI experiments achieve when ignoring the third dimension is possible and appropriate. A good candidate for a 3D imaging study needs therefore to exhibit a highly non-symmetric behaviour with respect to the spatial distribution of its chemical products. Generally, such systems comprise e.g. multi-photon excitation processes with polarised laser light or chemical reactions of aligned or oriented reactants.

2.5.1. *Multi-photon excitation processes*

The $(2+1)$ resonance enhanced multi-photon ionisation of hydrogen chloride was extensively investigated by Green *et al.* [35–37]. In the region from $77{,}000\,\mathrm{cm}^{-1}$ to $96{,}000\,\mathrm{cm}^{-1}$ Rydberg states with a $[^2\Pi_i]$ core are accessed which show a complex fragmentation behaviour which has been studied by several groups [13,25,38,39]. The excitation into the double minimum $V(^1\Sigma^+)$ state yields mainly H^+ and Cl^+ fragments from three sources: (1) Fragmentation of a super-excited Rydberg state into either $H^*(n=2)+Cl$ or $H+Cl^*(4s,4p,3d)$ followed by ionisation of the excited atomic species, (2) fragmentation into $H^+ + Cl^-$ on the ion pair excited potential energy surface and (3) fragmentation of vibrationally excited $HCl^+(v \geq 5)$ into $H^+ + Cl$. All three pathways require the existence of the outer well of the $V(^1\Sigma^+)$ state at rather large internuclear distances of ca 250 pm whereas excitation of HCl into Rydberg states of different electronic character mainly produces vibrationally cold HCl^+ molecular ions.

The total number of photons absorbed by H^+ and Cl^+ products is 4 whereas for the generation of HCl^+ three photons need to be absorbed, so higher order anisotropy terms become important for describing the spatial anisotropy of the process. Depending on the involved states and the number of absorbed photons, the kinetic energy release and the spatial distribution of the products will be different. The investigation of these competing multi-photon processes therefore yields information about the dynamics of the decay process. The observed 3D images were fitted with the function $F(\chi) = A\sin\chi\,(1+\beta_2 P_2(\cos\chi)+\beta_4 P_4(\cos\chi)$ where A, β_2 and β_4 are fit parameters, P_2 and P_4 are the second and the fourth Legendre polynomials, and χ denotes the angle between the polarisation vector of the laser and the product momentum vector $\vec{p}$. In 3D imaging this fitting procedure can directly be applied to the observed 3D image and does not rely on any reconstruction methods. Physically, Legendre polynomials up to rank $K=6$ and even more may be needed to describe the angular distribution, having in mind possible contributions from the initial anisotropy in the molecular beam, alignment of the molecular excited states, and the following multi-photon fragmentation. However, it was found that the contribution from the additional $\beta_6 P_6(\cos\chi)$ term could not be accurately extracted from the experimental data.

From the analysis of the 3D velocity distributions of H^+ ions for the $Q(0)$ and $Q(1)$ rotational transitions of the (E, $v=0-X$, $v=0$) and the (V, $v=12-X$, $v=0$) vibrational bands large and positive β_2 parameters were obtained. Further, a decrease of β_2 parameters in the $Q(1)$ transition in comparison to the $Q(0)$ transition was found for both vibrational transitions. It was concluded that this decrease is due to the alignment of the excited HCl*($J=1$) molecule, which is produced via the $Q(1)$ transition in a two-photon step. This alignment is absent for the $Q(0)$ transition, since the $J=0$ rotational state is isotropic. The alignment is due to the perpendicular nature of the two-photon step which occurs via a $^1\Sigma \rightarrow {}^1\Pi \rightarrow {}^1\Sigma$ pathway [13].

In principle, the 3D imaging technique allows one to also study the alignment of HCl in the molecular beam prior to photon absorption. Such alignment has been observed for a variety of molecules, and such alignment cannot be *a priori* considered to be absent. While the general theory outlined in reference [13] is applicable to the aligned and non-aligned species likewise, the values for the experimentally observed anisotropy parameters must be different for different polarisation directions of the excitation laser. Note that the presence of such alignment is a serious problem for 2D imaging methods relying on reconstruction methods, while the 3D imaging technique is ideally suited for its study. However, from the comparison of the angular distributions of H^+ ions obtained for $Q(1)$ transitions for both laser polarisations, it could be concluded that alignment of HCl in the molecular beam was small under the prevailing experimental conditions.

It has recently been reported that for selected rotational states of the F($^1\Delta_2$) state of HCl the fragmentation pattern resembles that of the V($^1\Sigma^+$) case rather than that of the F($^1\Delta_2$) case [40]. This behaviour was suggested to be due to the accidental resonance between rotational states belonging to the two surfaces. The suggested mechanism for the unusual behaviour of the F($^1\Delta_2$) state can only be investigated by analysing the kinetic energy release and the spatial distribution of the fragments. We have therefore further studied this process by 3D VMI. The results indicate that in addition to the proposed rather effective resonance assisted fragmentation another minor fragmentation channel exists which most probably proceeds via the inner wall of a super-excited bound Rydberg state. Corresponding results of energy and spatial distributions of the fragments will be presented and discussed in a forthcoming publication.

2.5.2. *Constrained geometry bimolecular reactions*

The reaction $O(^1D) + N_2O(X^1\Sigma^+) \rightarrow NO(X^2\Pi) + NO(X^2\Pi)$ has extensively been studied in the gas phase and initiated from the $(N_2O)_2$ dimer. At room temperature conditions, the vibrational population distribution of NO was monitored in a series of experiments and found to decrease monotonically from $v=0$ to $v=14$ [41–44]. Simons *et al.* studied the stereodynamics of the reaction by LIF [45–47] and observed vibrational excitation of NO up to $v=18$. Kajimoto *et al.* performed LIF studies with isotopically labelled precursor molecules to distinguish between the newly formed and the old NO bonds [43,48]. Although the vibrational distribution of the new NO was found to be more excited than that of the old NO, their vibrational populations are not significantly different. Rotational and translational temperatures are large (10,000 K and 13,000 K) and agree with statistical models [49,50]. Earlier, Kajimoto *et al.* had initiated reaction (1) in the $(N_2O)_2$ dimer by 193 nm photolysis of isotopically labelled N_2O and detected the NO reaction product by

LIF (laser induced fluorescence) in order to characterise vibrational and rotational populations of the NO product of the same system [51,52]. Results were strikingly different from those of the bulk reaction.

In order to reinvestigate this different behaviour, the reaction $O(^1D) + N_2O \rightarrow NO + NO$ was initiated in a $(N_2O)_2$ van der Waals complex and NO products were state-selectively analysed by the 3D VMI [26]. The dimer was produced by a supersonic molecular beam expansion. Product properties were found to be strikingly different from products generated in the bulk reaction, in good agreement with previous results on vibrational and rotational excitation [53]. Vibrational excitation of NO was detected from $v = 0$ to $v = 7$. Higher vibrational states are less populated than lower ones. Vibrational states with $v > 7$ are likely to be populated, but are not detectable by the employed $(1 + 1)$-REMPI scheme. Rotational excitation in all studied vibrational bands was very low and could well be described by a rotational temperature of ca 150 K. Translational excitation was determined for the first time. In the molecular beam frame products are very slow, i.e. the speed of NO in the $O(^1D) + N_2O$ centre of mass frame must be of similar absolute value, but of opposite sign than the speed of the centre of mass in the molecular beam frame. In other words, all observed NO products are pronouncedly backward scattered. The spatial distribution of the backward scattered products was determined with unprecedented accuracy. In the molecular beam frame it was found to be isotropic.

The pronounced difference between products generated from the bulk reaction and from the reaction initiated in the dimer should be due to a restrained reaction geometry which allows to sample only a small part of the potential energy surface controlling the $O(^1D) + N_2O$ system.

Both examples discussed above represent systems where full 3D imaging is needed to be employed in order to obtain reliable and accurate results for systems exhibiting no or only restricted symmetry. Another such example is the work done in the Zare group on the H atom exchange reaction [28–30]. Further such applications can be expected to be described in the future, given the rapid technological development described in detail in the following section.

3. Recent technology

3.1. *Introduction*

Imaging techniques in chemistry rely on position sensitive detection of low-energy ions and electrons. Since in this detection technique normally micro-channel plates (MCP) are used as image intensifiers, one can say that the real 'birthday' of imaging techniques was in 1971 [54]. Very soon after this date, several imaging detector systems for mass spectrometry were created. These systems had different read-out schemes, which started endless attempts to employ the temporal and spatial information provided by MCPs and endless discussions which read-out scheme is better. For example, in 1974 Lampton and Paresce built one of the first such mass spectrometers which they called 'Resistive Anode Image CONvertor (Ranicon), where the MCP was coupled to a large area resistive anode [55,56]. This 2D anode is an extension of the resistive wire technique into planar geometry. The pickup element is a flat rectangular or circular resistor equipped with conductive electrodes contacting three or more zones of its periphery. When charge is deposited at any point on the resistive anode, it is removed via the contacts in relative amounts which

depend upon the location. Such techniques were applied, for example, for mass spectrometry of large molecules [57]. Electro-optical read-out using a fluorescent screen in combination with a vidicon camera was used by several other authors [58,59]. In such experiments, the phosphor-coated anode converted the pulses of electrons from the MCP into an optical image. It showed large sensitivity and large potential for further improvement due to modernisation of individual components of the system. Also, several other techniques for read-out of the MCP signal were used. For example, linear resistive anodes were used in reference [56], or in reference [60] an array of photodiodes was used behind a phosphor-coated anode instead of a vidicon camera.

Probably, the first really informative 2D imaging of reaction products was observed in 1974, when Czyzewsky *et al*. [61] observed O^+ ions emitted from a tungsten surface due to low-energy electron ($\sim$100 eV) bombardment of O_2 molecules absorbed at the surface. The real start of applications of the imaging technique in gas-phase chemistry was in 1987, when Chandler and Houston [2] published an article, in which the photolysis of CH_3I at 266 nm was studied and photofragments – CH_3 and iodine atoms – were detected via resonance enhanced multi-photon ionisation (REMPI) by flashes on a phosphor screen. In other words, it was the first TOC mass-spectrometer with position sensitive detection of ions. This experiment provided an image (a photography) of the space distribution of the ions, which is a 2D projection of the 3D velocity distribution. Here the time component of the image vector was not accessible and therefore its influence on x and y needed to be minimised which has been achieved by using the 2-field Wiley–McLaren TOF spectrometer under energy and space focussing conditions. Since that time there have been a lot of important technical improvements. Imaging techniques have been strongly developed and nowadays they are extensively used in molecular dynamics. In some areas, such as molecular dynamics of photodissociation, it has become the most popular experimental tool.

3.2. *Technology*

3.2.1. *Micro-channel plates*

An MCP is a flat glass disc (of typically 2 mm thickness, with maximum outer diameters of about 120 mm) containing millions of very thin glass capillaries leading from one side to the opposite side, densely distributed over the whole surface and covered by a semiconducting material. Each capillary or channel works as an independent secondary-electron multiplier, in which the multiplication takes place under the presence of a strong electric field. The impact of an ion starts a cascade of electrons that propagates through the channel by which the original signal is amplified by several orders of magnitude depending on the electric field strength and the geometry of the MCP. After the cascade, a micro-channel takes some time to recharge before it can detect another signal. Most modern MCP detectors consist of two MCPs with channels slightly tilted with respect to the MCP surface. They are rotated 180° against each other producing a chevron (V-like) shape of two channels in the different MCPs facing each other. In a chevron MCP the electrons that exit the first plate start the cascade in the next plate. The advantage of the chevron MCP over the straight channel MCP is good ion feedback suppression and significantly more gain at a given voltage.

The electrons exit the channels on the opposite side where they are themselves detected by additional means, often simply a single metal anode measuring total current. In some applications each channel is monitored independently to produce an image.

MCPs are used for detection of particles (neutrons, electrons or ions) and a wide range of other radiation including UV, VUV and soft X-ray photons with a high detection efficiency. MCPs have a combination of unique properties, such as high gain (10^6–10^8), high spatial resolution and high temporal resolution. MCPs are intrinsically very fast detectors. The pulse transit time through the intense electric field is of the order of 100 ps, hence the transit time for a single plate with a length to diameter ratio of 40 : 1 operating under typical voltages is about 50 ps. Since each channel of the MCP serves as an independent electron multiplier, the channel diameter d and centre-to-centre spacing l_{c-c} determine the MCP resolution. The ratio of the open area to the total effective area of the MCP is called open area ratio. The particles incident on the MCP between channels are not detected, hence the ratio is an important characteristic of an MCP, since it limits the ultimate detection sensitivity of the MCP. For a 10–12 structure ($d = 10\,\mu m$, $l_{c-c} = 12\,\mu m$) the ratio is 63%, for 12–15 it is 58% and for 15–18 it is 63%. In some applications, such as coincidence measurements, it is desired to make the ratio as large as possible. For this purpose, there are custom MCPs in which the glass channel walls on the input side have been etched to increase the ratio up to 80%.

For MCPs with tilted channels the sensitivity depends on the angle between the velocity vector of the particles (ions or electrons) and the axes of the individual micro-channels [62–65]. Normally, the angle between the micro-channel axis and the surface vector of the MCP surface is 8°. When particles fly into the micro-channels parallel to the axes of the micro-channels, they penetrate deeply into the channels before producing secondary electrons, thus reducing the total gain of the MCP. This fact is normally ignored, but it may introduce some systematic error in the measurements, where total intensity of output electron flow from the MCP is integrated. Dependences of MCP efficiencies on the particle impact angle have been reported for electrons [62,65] and ions [63,64].

3.2.2. *Multi-coincidence 3D detectors for low-energy particles*

The electrons which exit MCP assemblies are normally accelerated to read-out devices, which should provide an electrical output signal responding to the position of the incident electron cloud and its time of arrival. The most popular 3D read-out electronic processing concepts and typical specifications are listed in Table 3. Some interesting, but not very common 3D detection concepts, such as, for example, the large area resistive anode [55,63] are not mentioned in Table 3.

3.2.2.1. *Multi-pixel detectors.* Multi-pixel detectors (MPDs, semiconductor detectors) are rather popular detectors in the physics of our days. They provide independent read-out of a large number of anode pixels. For example, the last version (1.5) of the Beetle read-out chip, developed by the Max Planck Institute for Nuclear Physics and the Kirchhoff Institute for Physics in Heidelberg, features an 8192 pixel anode [66]. This chip is designed for multi-anode photomultiplier read-out. It has 1 ns timing resolution, < 0.2 mm position resolution (0.8 mm pixel size), no dead time for distances > 3 mm, but 20 ns for smaller

Table 3. Read-out electronic processing 3D concepts used in imaging techniques and their typical specifications.

	Multi-hit capability	Detector resolution		Rate	
Concept	'Events'/dead time	mm	ns	kHz	References
MPD	100	0.2	1	1100	[66]
CWD	1/(3–5 ns)	2.5	0.2	1000	[68]
DLD	<3	0.1	0.1	20–1000	[73]
WSA	1	0.04–0.1	>6	0.4–150	[76]
DLD+CCD	$<3(>1.5$ ns)	0.1	0.07	0.03	[88,89]
CCD+PMT		0.04	0.2	0.06	[86]
CCD + CCD′	100	0.05	0.4–2	0.025	[87]

distances and can monitor up to 5 hits per pixel. Hence, the detector has an optimum multi-hit capability at a good signal processing rate and moderate time and position resolution. Current multi-pixel semiconductor detectors have a low position and a good time-resolution at potentially high data-processing rates. Also, they normally have a very good multi-hit capability. Their disadvantages are their high price and their complexity, because of the large number of electronic processing channels.

3.2.2.2. *Crossed wire detectors*. A crossed wire detector (CWD) consists of two sets of independent wires, along the X and the Y axis, to provide position information in two dimensions. The signals from each wire are processed independently. If an electron cloud from the MCP hits at a crossing of two wires, coincident pulses on the wires will be generated and registered by time-to-digital converters (TDCs). The detector is thus unable to detect particles which arrive at the same time. A typical CWD, consisting of 30×330 wires with 0.5 mm spacing has been used in the group of Becker [67].

An interesting example of CWDs is used by Lutz *et al*. [68] (Figure 4). Instead of wires, the lines are made from copper squares connected in rows. There are 16 rows along the x axis and 16 rows along the y axis. Hence there is an array of 256 squares ('pixels') etched into a copper-plated epoxy-board. These rows are terminated by 50 Ω shower-max detectors on each end, with each opposite end connected to trans-impedance amplifier. An important advantage of this system is the large sensitive surface area of each 'pixel'. As a result, typical signals have amplitudes of 10–30 mV. For comparison: the signal amplitudes for a usual CWD made from 32×32 gilded tungsten wires (50 μm in diameter) are about 1 mV. Moreover, the efficiency is less than 20% of that of the etched structure: only a comparatively small number of hits produced large signals in both the x and the y wires [68]. This detector has a timing resolution down to 0.2 ns and a position resolution of 2.5 mm. Finally, such detectors have a simple concept, an effective read-out scheme with good timing resolution, no dead time for different x and y positions, but a low position and a moderate multi-hit resolution.

3.2.2.3. *Delay line detectors*. The technical realisation of the delay line detector (DLD) itself is described in detail in references [69–73]. A DLD consists of two individual delay

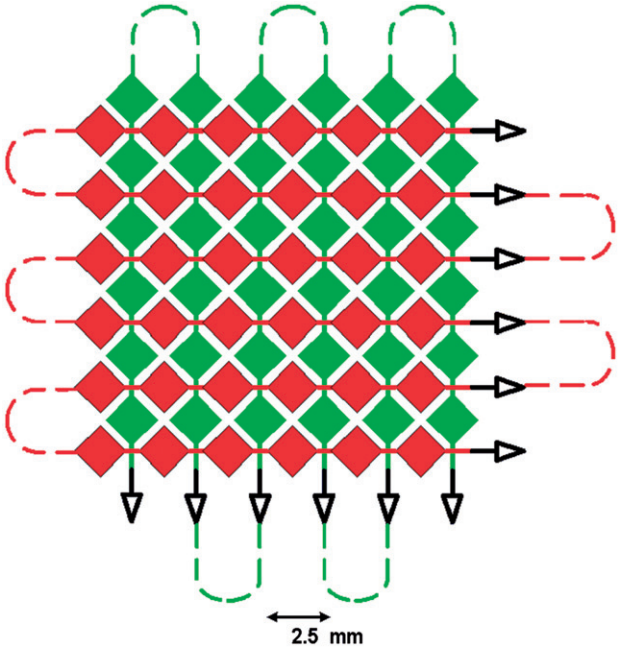

Figure 4. [Colour online] Scheme of a CWD with printed circuit board 'wires' (only 6×6 are shown). Its advantage is a large sensitive surface of each 'pixel'. Triangles denote TDCs. There are no contacts between the green and red lines. If an electron cloud from the MCP hits such a 'pixel', the pulses on the 'wires' will be registered by the TDCs. Contacts shown by the dashed lines are absent is the case of a CWD. They show how to make a delay-line detector as described by Jagutzki *et al*. [73].

lines wound orthogonal to each other to provide positional information in two dimensions (Figure 5). These lines are held with ceramic holders fixed on the edges of the 8×8 cm square copper plate, with wire planes separated from each other and from the copper plate by about 1 mm. Each delay line consists of a pair of wires separated by approximately 0.5 mm, with a small potential difference (30 V) applied between the two wires. Thus, the incoming charge cloud from the MCP induces a differential signal on each delay line pair that propagates to the delay line ends where it is picked up by a differential amplifier. By this folding technique, a propagation delay of 20 ns/cm and a total single-pass delay of 150 ns is realised.

One 'event' produces two pairs of times, $t(x_1)$, $t(x_2)$ and $t(y_1)$, $t(y_2)$ on the delay lines wound along the x and y axes, respectively. The x and y coordinates of a single event in time units may be calculated as $k(x_1-x_2)$ and $k(y_1-y_2)$, where k is a factor which converts time to distance; the time of the event (corresponding to the z coordinate) is usually calculated as $t=[t(x_1)+t(x_2)+t(y_1)+t(y_2)]/4$. Thus the DLD yields the 3D coordinates of each single event. The latter condition allows one to distinguish between true and false events: the time for a true event provided by the different delay lines must coincide, hence $t(x_1)+t(x_2)=t(y_1)+t(y_2)$. Only those events that obey this condition are taken into account and all others are ignored.

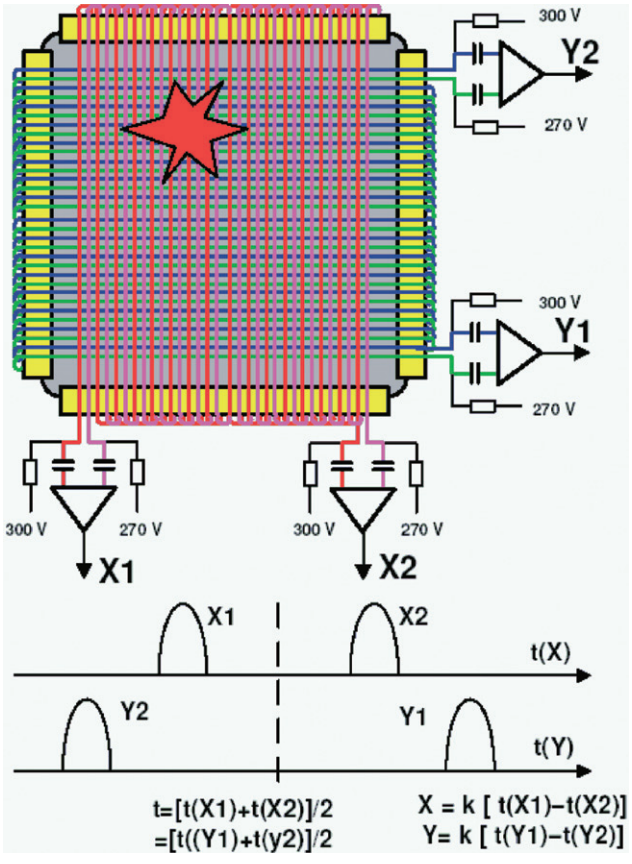

Figure 5. [Colour online] Principle of the DLD. The x_1, x_2, y_1 and y_2 denote differential amplifiers placed at the end of delay line pairs. $t(x_1)$, $t(x_2)$, $t(y_1)$ and $t(y_2)$ denote signal arrival times, respectively.

Such detectors have a simple concept, low complexity and costs, high data processing rates and good time and position resolution. However, there exist some important limitations for such DLD detectors: First, they principally cannot assign the electrical pulses to events if the events occur at the same place, but at different times, and second, they have a very restricted multi-hit capability.

A hexagonal version of a DLD detector is presented in Figure 6. It consists of three delay lines, wound at 120° relative to each other. Hence, it gives six arrival times, $t(A_1)$, $t(A_2)$, $t(B_1)$, $t(B_2)$, $t(C_1)$ and $t(C_2)$, from which the three coordinates of an 'event' can be calculated: $t=[t(A_1)+t(A_2)]/2=[t(B_1)+t(B_2)]/2=[t(C_1)+t(C_2))]/2$, $x=t(B_2)-t(B_1)=[t(A_2)-t(A_1)]+[t(C_2)-t(C_1)]$ and $y=[t(C_2)-t(C_1)]-[t(A_2)-t(A_1)]$. Now there are three mathematical conditions to assign the pulses to the events: This increases the multi-hit capability of the hexagonal detector. Also, the problem of ions which arrive at the same place at different times is not encountered in this setup. Such hexagonal detectors have been designed rather recently, but they have already been used, for example, in the Cold Target Recoil Ion Momentum Spectroscopy (COLTRIMS) reaction

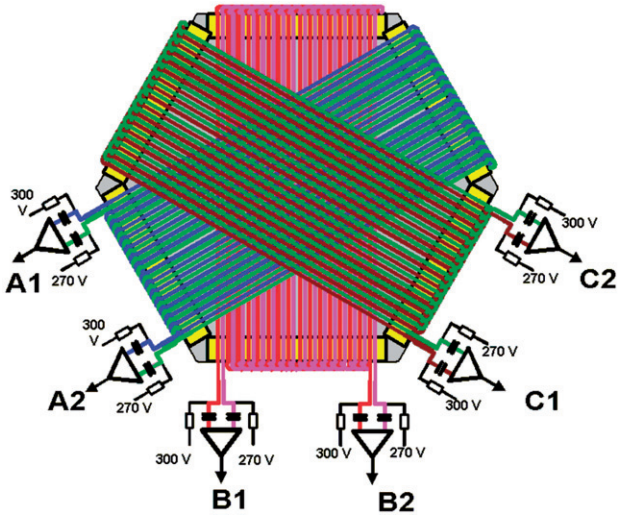

Figure 6. [Colour online] Hexagonal version of a DLD detector. Three delay line pairs are used. A_1, A_2, B_1, B_2, C_1 and C_2 denote differential amplifiers placed at the end of delay line pairs. The $t(A_1)$, $t(A_2)$, $t(B_1)$, $t(B_2)$, $t(C_1)$ and $t(C_2)$ denote signal arrival times, respectively.

microscope [74,75]. Another new interesting version of a rectangular DLD was proposed recently by Jagutzki *et al*. [76]. The idea is the same as in Figure 4. Instead of copper wires, the lines are made from squares connected in rows. As a result the x and y lines occupy the whole area of the detector without overlapping. This technology is simple, the square structures are produced by standard line photo-etching on a 40 μm two-layer kapton substrate with 25 μm copper.

In early versions of DLD detectors, the arrival times were normally obtained from TDCs, but nowadays they are commercially available together with fast analogue to digital converters (ADCs). In our group we analyse the shape of the signals by fitting the output of the DLD (Roentdek) by a set of Gaussian functions, using a 4-channel 500 MHz LeCroy oscilloscope (5Gs/s, Waverunner 6050) also possessing fast ADCs. This analysis gives the positions of the electric pulses with large accuracy, it allows one to distinguish between overlapping pulses, and also to assign pulses to events, according to their amplitudes, an information not used in the TDC analysis. We found that the knowledge of amplitudes of the pulses is very useful for the analysis of complicated many-pulsed signals. This approach also increases the multi-hit capability of the DLD detector.

The DLDs are normally used for large-frequency applications. For example, the 'reaction microscope' (ion-electron coincidence detection from ionisation processes) at the VUV free electron laser based on the electron synchrotron (DESY) at Hamburg uses 12 cm diameter DLDs with a 1 GHz flash ADC read-out. Another example is the recently created multi-plexed chemical kinetic photoionisation mass spectrometer [77]. It is designed for the study of kinetics and isomeric product branching of gas phase chemical reactions; hence, it is able to distinguish between different structural isomers. This excellent apparatus uses rectangular DLDs with the average ion count rate limited by the electronics (~30 kHz).

Figure 7. [Colour online] Three anodes are shown by different colours. They are separated by very narrow insulating gaps (~30 μm). The area of black anodes (strip) linearly increases in width, as they progress from left to right (x direction), the area of each of the red anodes (wedge) linearly increases in width, as they progress from the bottom to the top (y direction), and the yellow anode (meander) zigzags between the black and red anodes.

3.2.2.4. *Wedge-and-strip anode*. Different constructions of wedge-and-strip anodes (WSAs) are proposed in the literature [78]. They may have three or four electrodes, which may be placed in many different ways. For example, there exist Cartesian and polar coordinate anodes. The most popular anode consists of three coplanar electrodes called according to their geometry wedge, strip and meander [78,76]. Such a WSA is schematically shown in Figure 7. Some authors make WSA detectors in different ways. One possibility, for example, is to manufacture the resistive layer by sputter coating with germanium on a ceramic substrate.

Like all detectors discussed in this section, a WSA detector is placed just behind the MCP stack. The charge of the electrons from the MCP is distributed over these three electrodes. To determine the position of the charge cloud centre one should measure the charge on each electrode independently and calculate x and y values using the expressions:

$$x = \frac{Q_S}{Q_S + Q_W + Q_M} \tag{16a}$$

$$y = \frac{Q_W}{Q_S + Q_W + Q_M}. \tag{16b}$$

Q_S, Q_W and Q_M are measured charges on strip, wedge and meander anodes, respectively. As one can see in Figure 7 the equations are derived just from the geometry of the anode structure.

Such detectors have a good position resolution, but no multi-hit capacity; and they have a large signal processing rate, which determines the time resolution. Specifications of the detector of Jagutzki *et al.* [76] are given in Table 3. Due to the limitation of the electronics, the spatial accuracy of the detector degrades from 40 μm at a 400 Hz read-out

frequency to 100 μm at a 150 kHz read-out frequency (with an active area of 40 mm in diameter). Also, there is a small nonlinearity near the perimeter of the detector due to electrostatic effects.

3.2.2.5. *Concepts based on detection of luminescence from a phosphor screen.* For imaging applications with low temporal resolution a phosphor screen coupled to a CCD camera is normally used. CCD camera based multi-fragment-detectors have an excellent position resolution. For example, on a typical 1000×1000 pixel CCD camera each ion creates a spot of ca 3 × 3 pixels. Centroiding calculations (which are made in real time) reduce the area of the spot down to 1/16 pixel size, yielding a 4000×4000 pixel image of the screen which is close to the spatial resolution limited by the MCP pore size (25 μm). It is important to know that ion imaging which includes real-time centre-of-mass calculations may be realised with standard video methods at very low cost [79].

Probably, the most important improvement in the phosphor screen photography technique in the past years is the above mentioned large acceleration of the electronic read-out due to usage of a complementary metal oxide semiconductor (CMOS) image sensor instead of a CCD camera [65] (Figure 8a). The detector consists of an MCP, a phosphor screen, a multi-stage image intensifier, a 512 × 512 pixel CMOS image sensor and a field programmable gate array (FPGA) circuit. The image data arrive at the CMOS device with a 1 kHz rate, then the FPGA performs digitization and calculation of the event coordinates and transfers the data in real time to a computer monitor. The read-out timing of a CMOS sensor is synchronised with the 1 kHz laser. Note that a light spot is detected in an 8×8 pixel block and the centre of gravity calculation yields an accuracy of 1/8 of a pixel.

In Table 3 the read-out frequencies of all CCD camera based detectors are shown to be about 20–60 Hz. However, if a CMOS based detector of Horio *et al.* [65] will replace the CCD camera, then the read-out frequencies of future 3D imaging CMOS based techniques (DLD + CMOS, CMOS + PMT and CMOS + CMOS′) should rise strongly, up to 1 kHz.

According to our knowledge, two purely CCD based concepts of 3D imaging exist, which allow one to measure the arrival times of ions. The first concept (CCD + PMT) is used in the Neumark group [71,80–86] (Figure 8b). Each event produces a spot on the phosphor screen; the position and arrival time of which are determined by correlated measurements using a CCD camera placed behind the image intensifier and a 4 × 4 multi-anode photomultiplier tube (PMT). The position of the event is determined from the CCD camera image and the arrival time from the PMT. The image intensifier and the PMT have different spectral sensitivities. Therefore, a dichroic beam splitter positioned at 45° with respect to the phosphor screen and with 50% transmission at 565 nm is placed behind the phosphor screen. It reflects smaller wavelengths of light to the PMT and transmits larger wavelengths to the image intensifier and the CCD camera. For this rather simple configuration the expected detector resolution σ_D is 40 μm in position and 200 ps in time.

The second concept is realised by two different research groups [11,87] and has already been discussed in Section 2.2.4. We denote it as CCD + CCD because it is based on using two CCD cameras focussed on the phosphor screen (Figure 8c). In the original concept, one camera (A) operates continuously while the other one (B) is time-gated in order to integrate light only over a limited time starting from the beginning of the laser pulse.

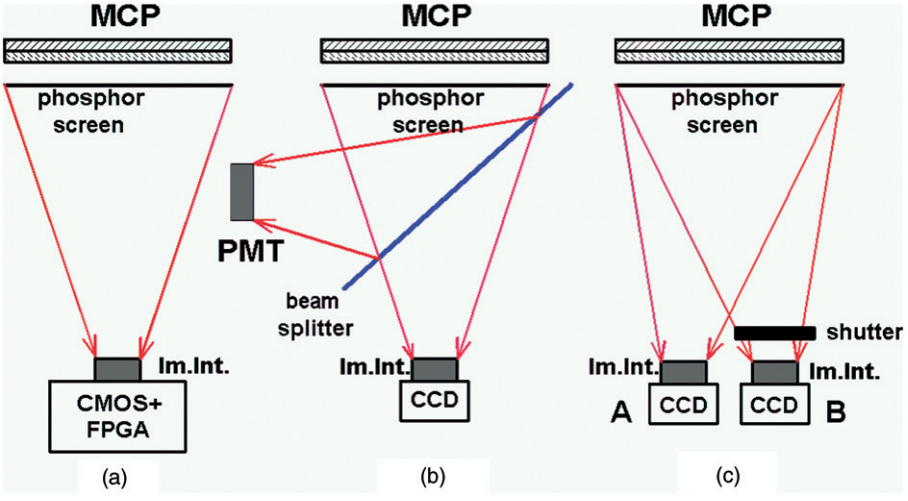

Figure 8. [Colour online] Phosphor screen based 3D detectors: (a) CMOS image sensor [65], (b) CCD + PMT, (c) CCD + CCD′ (CMOS: complementary metal oxide semiconductor image sensor, FPGA: field programmable gate array, CCD: charge-coupled device camera, PMT: photomultiplier, Im.Int.: image intensifier). Optical lenses are not shown.

Imagine, for simplicity, that two ions i ($i = 1, 2$) arrive at times t_i. The time dependence of the luminescence intensity $I_i(t)$ normally follows an exponential law:

$$I_i(t) = \begin{cases} I_0 e^{-\frac{t-t_i}{\tau}} & \text{for } t \geq t_i \\ 0 & \text{for } t < t_i \end{cases} \tag{17}$$

One can show, that the difference between the times t_i may be determined as

$$t_1 - t_2 = \tau \cdot \ln\left(\frac{1 - \frac{I_{A1}}{I_{B1}}}{1 - \frac{I_{A2}}{I_{B2}}}\right) \tag{18}$$

Here, I_{Ai} and I_{Bi} denote integrated light intensities for the i-th ion from cameras A and B, respectively.

Da Costa *et al.* wrote in reference [88]: 'This very clever and innovative system has probably the highest multiplicity that has been reached up to now. Strasser *et al.* suggested using this device for 3D atom probe applications. However, its use requires extreme care in the choice of the CCD features and the phosphor material. In the case of 3D atom probe, multiple events occur over a period of 10 µs after the ablation pulse, so the use of a phosphor material with a long decay time would require a CCD camera with a large number of pixels and high dynamic (over 12 bits). Such a camera cannot be run at high frequencies and this is the main limitation to this device.'

3.2.2.6. *DLDs with CCD.* The CCD read-out combined with the delay-line technique was recently designed by Deconihout *et al.* [88, 89]. In the detector the delay-line anode is

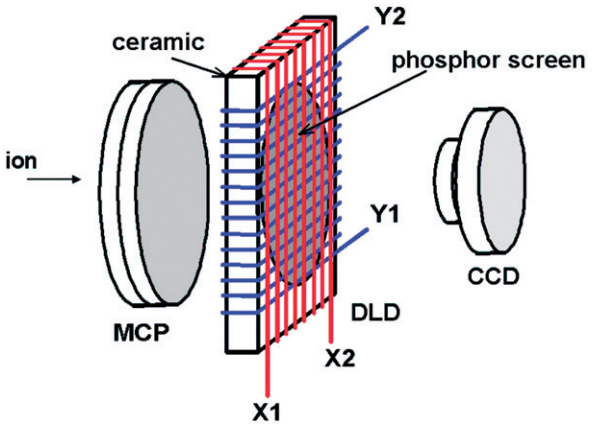

Figure 9. [Colour online] Scheme of a combined CCD-DLD assembly [88]. The image on the CCD screen yields rough x, y coordinates of events while the precise coordinates and timing information is obtained from the DLD.

combined with a phosphor screen allowing additional positioning to be made via a CCD camera, (Figure 9). This additional positioning information is used to unambiguously quantify performances in terms of spatial resolution and multi-hit capabilities. The use of dedicated signal processing procedures leads to a timing accuracy of 70 ps and a dead-time below 1.5 ns (no dead time for different positions). As a result, the spatial resolving power of this detector is close to 0.2 mm leading to a relatively high multi-hit capability, but the signal processing rate is relatively low.

A sharp depleted zone is observed for impacts separated by less than 1.5 mm. This distance is clearly related to the 1.5 ns time resolving power of the method. Simultaneous impacts separated by less than this distance are not resolved by the method because their time difference on the ends of the wire pairs is less than 1.5 ns. As a result, the advanced DLD is only blinded during less than 1.5 ns on a square surface of less than $1.5 \times 1.5\,\text{mm}^2$.

Note also that the distance between the back of the MCP assembly and the phosphor screen is rather large (~2 cm) and that a voltage of 2 kV is applied between them. Hence, only wide spots are observed. This is not important, however, since the CCD camera provides only approximate qualitative data on positions of events while all exact measurements are done by the DLD.

3.2.2.7. *Summary on 3D imaging detectors*. In order to fully exploit the MCP specifications, the 'ideal' read-out device should be able to detect hundreds of simultaneously hitting particles with a 20–30 μm position resolution and sub-nanosecond time resolution. As it is shown above, although presently there are no such 'ideal' read-out devices, progress in this area is rapid and existing detectors approach 'ideality' quickly.

Note, however, that for many chemical applications existing detectors are already perfectly suited. For example, there is no need to have a time resolution of $\sigma_{Dt} = 0.1$ ns, if the experimental uncertainty σ_{Et} is much larger due to the use of standard lasers with a pulse duration of approximately 5 ns. Of course, excellent detector space resolution σ_{Dr}

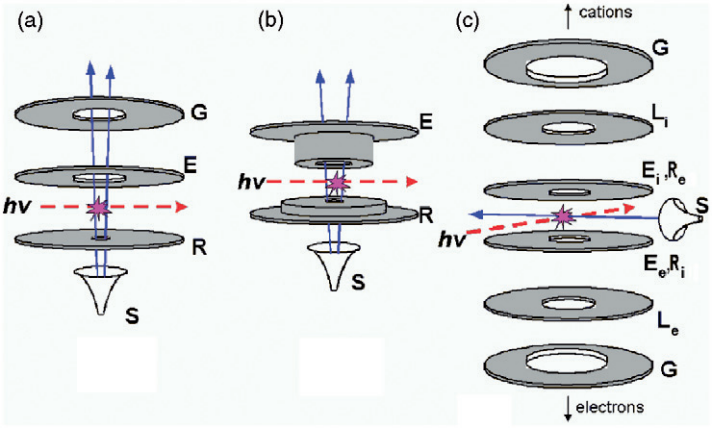

Figure 10. [Colour online] Different VMI configurations (S: skimmer, R: repeller, E: extractor, G: ground electrode, L: lens). The blue solid arrows represent the molecular beam, the dashed red arrows the laser beam. Indices i(on) and e(lectron) are used to show the polarity of the electrodes. (a) 'Conventional' VMI configuration [12]. (b) Single field (two electrodes) ionic lens configurations [104], (c) VMI for photoion–photoelectron coincidence [90]. The lenses L are for convenience, they are not necessary elements. During 100 ns after the pulse of femtosecond laser the voltages E_e and R_e are applied for electron VMI, after this time the voltages E_i and R_i provide ion VMI.

is necessary in photoelectron spectroscopy, but in REMPI spectroscopy of ions the experimental uncertainty σ_{Er} is often determined by the electron recoil in the photoionisation process [1,17]. Also, really narrow speed distributions of ions normally occur only in the photodissociation of diatomic molecules while in other cases it is much broader. Moreover, the detector space resolution σ_{Dr} of the cross-strip anodes used by Vredenborg *et al*. was limited by the ultimate pore diameter of the entrance MCP of about 7 μm. However, the total spatial resolution σ_r was limited by the quality σ_{Er} of the velocity mapping the ion trajectories due to the extended source of the ions and electrons [90].

3.2.3. *Electrostatic field configurations*

3.2.3.1. *Configurations before 2005*. Now we consider the configurations of electrostatic fields in TOF mass spectrometers. It is assumed that the ions are produced in the gas phase by laser radiation and the electric field accelerates them towards the MCP. We have already discussed in Section 2.2 the single-field and Wiley–McLaren configurations [7,8] and the velocity mapping scheme derived from the Wiley–McLaren configuration by Eppink and Parker [12].

Different schemes of a VMI spectrometer are given in Figure 10. The 'conventional' ion optic design consists of three parallel flat annular electrodes: repeller R, extractor E and ground G. Ions are created between repeller and extractor. In the apparatus of Parker and Eppink the diameters of R, E and G are 70 mm, with inner diameters of l, 20 and 20 mm, respectively. Voltages are $V_R = 4000$ V, $V_E = 2820$ V, $V_G = 0$ V, respectively, and distances are: R − E = E − G = 15 mm, G − D = 360 mm, where G − D is the distance from the ground electrode to the MCP [12,15]. In general, the optimum focussing conditions

were achieved when $(V_E - V_G)/(V_R - V_G) = 0.71$. Note that the potentials may be synchronously scaled in order to change the final kinetic energy of ions.

Other authors have modified this 'conventional' VMI configuration. Modifications include the addition of an Einzel lens (two extractor electrodes) [91–93], the use of several lenses [94,95], of a non-flat extractor electrode [96], of a focussing electrostatic hexapole lens situated between the skimmer and the repeller plate, working also as state-selector [97–99], or of deflection plates or electrodes placed between the ionic lens and the MCP assembly [100]. The latter are normally used to direct the ion beam exactly to the middle of the detector and may either be of electrostatic or hexapole type.

A very interesting idea is employed in the spectrometer of Lipciuc *et al.* [101]. The ion lens system operates in two different modes. One is the 'conventional' VMI mode, and the other mode is used to orient molecules before photodissociation by a strong and homogeneous electric field. It is important that the directions of the electric fields in these two modes are perpendicular. Note that the repeller and extractor electrodes are split into an upper half and a lower half. In the first mode the ionic lens works as usual, while in the second mode a positive voltage is applied to the upper repeller, orientation and extractor electrodes, and a negative voltage to their lower counterparts.

At present, the design of a new VMI spectrometer [90,100,102] requires the simulation of ion trajectories. For this purpose normally the program Scientific Instruments Services (SIMION) is used. The design is used not only to provide VMI conditions, but also to minimise the spherical and chromatic aberrations [96]. Note that these aberrations can only be minimised, but not eliminated. For example, the ionic lens design of Wrede *et al.* [96] reduced chromatic aberration by a factor of ~3.5 relative to that achievable with a 'conventional' ion optic design, but yielded only a small reduction of spherical aberration.

An example of a VMI lens configuration for a novel photoelectron–photoion coincidence machine [90] is shown schematically in Figure 10c. First, 65 ns after the laser pulse the voltages $E_e = -385$ V, $R_e = -520$ V and $L_e = -270$ V are applied. Thus, the mass spectrometer detects all photoelectrons which have a TOF of about 15 ns. After this time the voltages are switched to opposite polarity $R_i = 2000$ V, $E_i = 1550$ V and $L_i = 750$ V. Now, photoions are detected by DLDs on the opposite side of the mass spectrometer.

A very simple electrostatic lens that magnifies the images of a VMI apparatus up to a factor of 20 has been designed by Offerhaus *et al.* [103]. It can be used to scale the image while keeping the field strength in the interaction region constant. The lens was reported not to add any observable aberrations to the image.

3.2.3.2. *Single field configuration.* Single field (two electrodes) ionic lens configurations to perform slicing and velocity mapping were proposed by Papadakis and Kitsopoulos [104]. The main idea of these configurations is to obtain space focussing. The new VMI geometry consists of two parallel annular electrodes (repeller and extractor) instead of three. These two electrodes are not flat, but have small flat-top steps (Figure 10b). The repeller is held using flush screws while the extractor is bolted onto a larger grounded plate. One geometry contains a flat metallic grid, the second one does not. The ion trajectories in both cases were simulated with SIMION.

The two electrode configurations have several advantages over the three electrode design: Space focussing, negligible chromatic aberration (that is, the focussing is

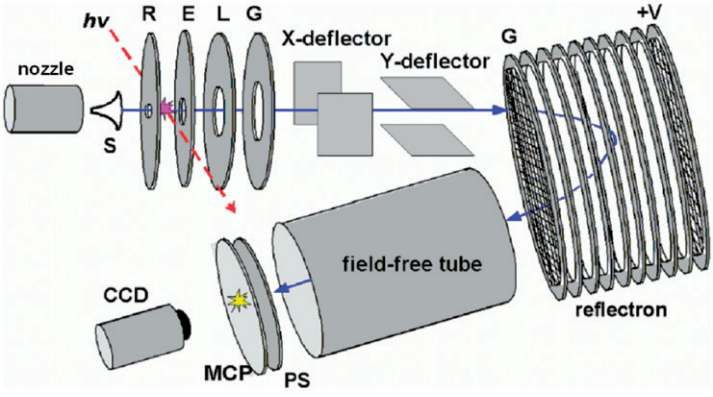

Figure 11. [Colour online] VMI reflectron configuration (S: skimmer, R: repeller, E: extractor, L: lens, G: ground, PS: phosphor screen). The reflectron delays the high-energy ions in comparison with low-energy ions. A uniform potential gradient in the reflectron is provided by rings and grids. The inside diameters for the R, E, L and G electrodes are 2, 16, 32 and 40 mm with spacing of 1.8, 2.1 and 2.9 cm, respectively. Typical voltages employed for this arrangement are 3000, 2550, 1827 and 0 V, respectively, with the reflectron held at 3860 V [92,106,107].

independent of the initial centre of mass velocity of the recoil particles) and compactness. Space resolutions for the two and three electrode designs are comparable. For both photoelectrons and photofragments a resolution of ~1% in velocity is achieved without further software manipulation, such as event counting [105].

3.2.3.3. *Reflectron multi-mass VMI configuration*. A VMI reflectron configuration [92,106,107] is shown schematically in Figure 11. It has conventional ion optics design (flat repeller, extractor and ground) with an additional lens. Ions are accelerated towards the reflectron, which can be regarded as an ion mirror reflecting incoming ions. The reflectron is a set of parallel resistively connected rings which create a homogeneous electric field directed towards the ions. The front and back of the reflectron is terminated by grids, which serve to define the retarding field. The higher the energy of ions, the deeper they penetrate into the reflectron and the longer time they spend in the reflectron. That is, the ions from higher potential regions of the ionisation volume are delayed more than the ions from lower potential regions. The potentials of the system are optimised in order to provide space focussing conditions. All ions of the same mass have the same total flight times regardless of the point of formation. The advantage of this configuration is achievement of VMI conditions together with space focussing and large overall flight length (2.5 m) which leads to high mass resolution.

In order to achieve spatially resolved mass dispersion, this technique has been modified by the introduction of a transverse deflection by short, pulsed electric fields [108]. The pulse is applied to the deflection plates and deflects the ions according to their mass. The pulse is turned on before the first ion in an ion packet reaches the deflection region, and is turned off before the first ion exits the deflection region. As a result, the position of a spot on the 2D-image represents ions of a certain mass and the size of the spot indicates

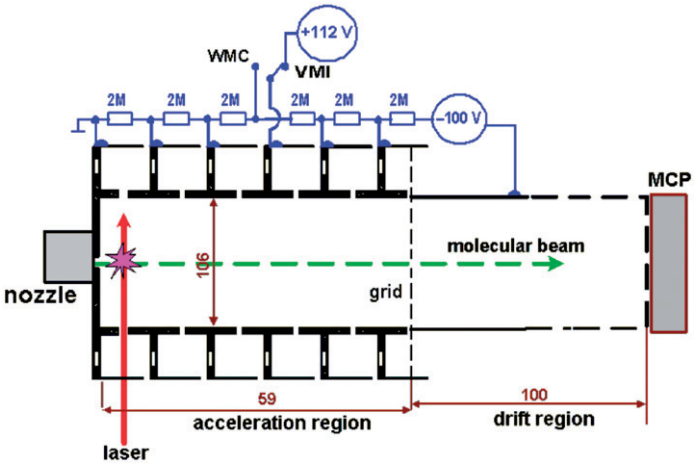

Figure 12. [Colour online] Realisation of a simple switching option between a diagonal single homogeneous field configuration (SF) and a 3D VMI configuration [10]. The direction of the laser beam is shown by a red solid arrow, the direction of the molecular beam is shown by a green dashed arrow.

the velocities of the ions. A mass resolution greater than 600 and a dynamic range $>10^3$ have been achieved.

3.2.3.4. *Simple switch between spatial and VMI.* The single homogeneous field configuration is sometimes very useful. The near diagonality of the momentum dispersion matrix lets one directly 'see' real dimensions and positions of laser and molecular beams, which can be used for adjusting the system. Second, in particular in experiments with low speed of ions (like the study of electron recoil in photoionisation [17]) the spatial imaging is hindered by the very small spot size of the image and only the 1D TOF mass spectrometry is feasible which has better time-of-flight resolution than the VMI configurations derived from a Wiley–McLaren setup (Table 2). Third, it is easy to describe the ion trajectories without having to rely on SIMION. Thus, a simple switching option to choose between the single-field and VMI configurations is highly desirable. A realisation of such an option is depicted in Figure 12. Briefly, it consists of a conventional single-field configuration with a field-free drift region twice as long as the acceleration region providing space focussing and linearity between p_z and Δt together with a good momentum dispersion M_{tz}, in which a homogeneous electric field is created by a set of parallel resistively connected ring electrodes. The switching between the single field and the VMI configuration is achieved by applying an appropriate voltage on one of the acceleration rings thus generating a superposition of the homogeneous field with an Einzel lens field.

The distortion of the ion position by the mesh is estimated to be less than 150 μm (about one pixel) [67]. Several authors have reported that the metallic grid on the way of the ions to the detector reduces the space resolution and hence the gridless configurations have a noticeable advantage. We doubt that this advantage is really so noticeable since there are several grid-containing VMI configurations [91,104] where the degradation of the space resolution is negligible. Moreover, in reference [104] it is reported that in spite

of SIMION predictions in the slicing mode, the gridless geometry performed less well than the grid-containing geometry. Note that in Wiley–McLaren configurations and VMI configurations derived from Wiley–McLaren design, the ionisation volume is very close (~1 cm) to the grid, so that grid induced image blurring can easily occur. However, in our configuration the grid is rather far (~5 cm) from the ionisation volume, hence the image blurring associated with the grid in our case should be substantially smaller.

3.2.4. *Doppler-free imaging*

Doppler-free (2 + 1) REMPI is a method which increases the detection efficiency without increasing the laser power, thereby creating more signal ions without changing the number of background ions. It assumes that the background ions absorb non-resonantly and that $\Delta\nu_D > \Delta\nu_L$, where $\Delta\nu_D$ and $\Delta\nu_L$ are the width of the Doppler broadened absorption spectral line of the probed particle and the spectral width of the laser radiation, respectively.

Doppler-free REMPI detection of ions was first proposed by Vrakking *et al.* [109] and later it was used with 2D imaging by Pomerantz and Zare [110]. In such experiments, the laser beam is divided into two equally intense beams using a 1 : 1 beam splitter. The beams are introduced into the reaction chamber from opposite sides towards each other. The beams are focussed into the centre of the chamber with lenses of equal focal lengths, so that they overlap in space and time. Now the REMPI absorption spectrum consists of two components. The first component has a normal Doppler broadened profile, because it arises from the absorption of two photons coming from the same propagation direction. The second component is Doppler-free, because it arises from the absorption of one photon from each of the two counter-propagating laser beams. The second component is normally much stronger by a factor of $\sim\Delta\nu_D/\Delta\nu_L$. Therefore, the method is particularly well suited for the detection of light ions (hydrogen atoms and molecules). The technique proved to be especially useful when there are few ions, for example, in the products of chemical reactions [27–29].

An important improvement was proposed by Riedel *et al.* [111]. While in the experiments of Pomerantz and Zare counter-propagating laser beams were linearly polarised, Riedel *et al.* used circularly polarised beams. In both cases, hydrogen atoms were detected through two-photon absorption via the 1^2S–2^2S transition where absorption of one photon from each of the two counter-propagating directions is assumed to take place. For this transition the selection rule is $\Delta M_J = 0$, which is always fulfilled for the case of circular polarisation, but only to 50% for the case of linear polarisation.

Yet another version has been reported by Goldberg *et al.* They have proposed two-colour Doppler-free REMPI [28] where one laser is detuned from the line centre by 8 cm^{-1} to the blue and the other laser is detuned to the red by the same amount. Now the two-photon resonant transition can only be driven by the absorption of one photon from each laser beam. A third photon from either laser beam ionises the excited molecule. This scheme achieves the same result as the scheme of Riedel *et al.* [111], but it does not rely on the selection rule $\Delta M_J = 0$ for a two-photon transition. It may be used, for example, to detect Cl atoms via the $3p(^2P_{1/2})-4p(^4D_{5/2})$ transition at 240.248 nm [112] where the selection rule $\Delta M_J = 0$ is not fulfilled.

4. Recent applications

Recently, Ashfold *et al*. [1] have published a comprehensive review article on imaging which is devoted to the applications of 2D imaging to the dynamics of gas phase reactions and which discusses imaging literature that appeared before mid-2005. This second part of the present review is written as a supplement and continuation of the review of Ashfold *et al*., and we try to avoid too much overlap with it. That is, we review imaging literature published from 2005 till the beginning of 2009, paying maximum attention to most important results and technical developments. Also, some subjects which are absent in the paper of Ashfold *et al*. are described in some detail.

The processes in our article fall into the categories (the references refer to review papers): (1) photodissociation of molecules, clusters and nanodroplets [1,104–106], including femtosecond studies [113], (2) inelastic scattering and bimolecular reactions [113–117] and (3) polarisation of photodissociation products [114,116,118] and preparation of polarised particles. Femtosecond photoelectron spectroscopy [119,120] and photoelectron imaging of negative ions [121–126] are not discussed in detail.

This article is devoted to chemical applications of 3D imaging. Hence, we limit our review somewhere on the boundary between physics and chemistry. This boundary we have chosen rather arbitrarily. Thus, we would like to discuss ions (cations and anions) 2D and 3D imaging, produced at 'low' excitation energies, i.e. in the range of a few eV, by conventional lasers. For example, since the studies of dynamics of one-photon dissociative photoionisation normally requires synchrotron radiation [127], we do not review such subjects.

We know of at least two recently developed very interesting continuous multi-mass ion imaging techniques. One is developed in the group of Ni which uses a delay between photodissociation and photoionisation. It also employs a magnetic field for spatial separation of ions and 2D imaging detection [128,129]. The other one has been developed in the group of Zare and consists of a reflectron TOF mass spectrometer that uses pseudo-random ion beam modulation and provides a mass spectrum at every pixel of a 2D surface of a 3D detector [32]. In our understanding both are neither 3D nor 2D imaging. Hence they are not discussed here. Likewise, applications of imaging in surface chemistry are beyond the scope of the present review. Thus, the emphasis of this article will lie on gas-phase chemistry.

4.1. *Photodissociation*

4.1.1. *Summary of 'traditional' photodissociation studies*

Table 4 lists all photodissociation processes of neutral molecules we know of which were studied by 'traditional' ion imaging. Normally, a $(1_d + 2 + 1_i)$ photon absorption consequence is assumed for all processes where the indices d and i are used to denote a dissociative and an ionisation step, respectively. Today, more and more studies are reported with different photon absorption sequences. Often, the ionisation occurs before the photodissociation. For example, Vidma *et al*. [130] observed that REMPI of the van der Waals dimer $(CH_3I)_2$ produces I_2^+ ions via the pathway $(CH_3I)_2 \xrightarrow{2h\nu} (CH_3I)_2^+ \xrightarrow{h\nu} I_2^+ + \text{products}$. Here, the photon absorption sequence is $(2_i + 1_d)$. Such processes cannot be excluded from Table 4, because very often they compete with

Table 4. Systems for which photolysis products were detected by imaging techniques. Precursor molecules and detected particles are listed in order, first, of increasing number of atoms in molecules, second, of increasing molecular mass. Clusters are denoted as A, B or A_n.

Detected	Precursor molecules
H,D	H_2 [239–243], D_2 [240], OH [244], OD [244,245], HCl [39,246], HBr [27,39,104,246,247], DBr [27,248] HI [246,249–251], H_3 [252–257], HCO [111], H_2S [258], NH_3 [259,260], C_2H_2 [261], H_2CO [262], HNCO [263], CH_2Cl [264], CH_4 [265,266], CH_2D_2 [265], C_2H_3 [267], $CDCl_3$ [268], C_2H_4 [269], CH_3SH [258], CH_3NH_2 [270], CD_3ND_2 [270], C_2H_6 [269], CH_3CHO [181], CH_3CFCl_2 [268], *N*-methylpyrrole(C_4H_5N) [105,271–274], pyrrole(C_4H_4NH) [104], C_3H_8 [269], C_3H_7SH [275], uracil($C_4N_2O_2H_4$) [276], phenol-d5(C_6D_5OH) [277], thymine($C_5N_2O_2H_6$) [278], $(D_2O)_{2n}$ [279]
$C(^1D)$	CO [280,281]
$N(^2D)$	NO [282], N_3 [283], N_2O [284,285]
$N(^2P)$	N_2O [285]
$O(^3P)$	OH [244], OD [244], NO [282,286,287], O_2 [15,250,288–294], ClO [289,295], BrO [296]. N_2O [284,297,298], NO_2 [299–305], O_3 [114,306–308], SO_2 [307,309–311], OClO [312,313], $(NO_2)_2$ [300]
$O(^1D)$	O_2 [294,314], N_2O [285,297,315–321], NO_2 [301], O_3 [307,322–327]
$O(^1S)$	N_2O [285]
O^+,O^-	O_2 [134]
$S(^3P)$	SH [99], SD [99], OCS [328,329], SO_2 [330], CS_2[331–335]
$S(^1D)$	SH [336], SD [336], OCS [97,98,329,330,332,334,337–342], SO_2 [330], CS_2 [331,333], C_2H_4S [343]
$S(^1S)$	OCS [344]
Cl	HCl [345,346], ClO [289,347], Cl_2 [9,94,348–352,198,353–356], BrCl [195,357–361], ICl [362,363], HOCl [364], ClNO [365–367], Cl_2O [364], CH_2Cl [264,368], ClN_3 [369,370], Cl_2CO [21], Cl_2CS [22], Cl_2SO [366], S_2Cl_2 [24], CH_3Cl [371], $CDCl_3$ [268], CH_2BrCl [372,373], CCl_4 [366], CF_2ClBr [374,375], CCl_3Br [376], C_2H_3Cl [377], C_3H_3Cl [163,378], CH_3COCl [379,380], $CH_2CHCOCl$ [381], CH_3OCOCl(methyl chloroformate) [382],CH_3CFCl_2 [268],CH_3OSOCl [383],CH_3SO_2Cl [383], C_3H_5Cl [384], CH_3CH_2COCl [385], 1,1-dichloroacetone($CH_3COCHCl_2$) [386], 2-chloro-2-propen-1-ol(CH_2CClCH_2OH) [387], c-OCH_2CHCH_2Cl [388], 2-chlorobutane(C_4H_9Cl) [389], $(CH_3)_3COCl$ [378]
Al	AlO [390]
Ar	ArKr [391]
Fe	FeO [390,392]
Br	HBr [345,393], BrCl [126,357,361], BrO [296]. Br_2 [355,394–398], IBr [96,355,399,400], BrCN [401], $COBr_2$ [402], CH_3Br [403–405], CH_2BrCl [406], CF_3Br [407], CF_2ClBr [374,375,408], CH_2Br_2 [409], CCl_3Br [376], CF_2Br_2 [410], $CHBr_3$ [411], CBr_4 [412], C_2H_3Br [413,414], C_2F_3Br [413], $C_2H_2Br_2$ [415], C_3H_3Br [378,416,417], CH_3COBr [418], C_2H_5Br [419], 1,2-C_2H_4BrCl [420], 2-bromopropene (C_3H_5Br) [421], CH_2CHCH_2Br [422], C_3H_6BrCl [423], 1,2-dibromopropane ($C_3H_6Br_2$) [424], 1,3-dibromopropane ($C_3H_6Br_2$) [425], cyclobutyl bromide (C_4H_7Br) [426], 1-bromo-2-butene ($CH_2BrCHCHCH_3$) [427], cyclopropylmethyl bromide ($CH_2BrCHCH_2CH_2$) [427], 4-bromo-1-butene ($CH_2CHCH_2CH_2Br$) [427], C_6H_5Br [428], *o*-,*m*-,*p*-$BrFC_6H_4$ [429], *n*-C_4H_9Br [430], *n*-C_4H_9Br [431], *m*-bromotoluene (*m*-C_7H_7Br) [432], *n*-$C_5H_{11}Br$ [433], *n*-$C_7H_{15}Br$ [434]

(*continued*)

Table 4. Continued.

Detected	Precursor molecules
Kr	ArKr [391], Kr_2 [391], Xe·pyrrole [168]
I	HI [435], IO [436], ICl [437,438], I_2 [11,439,440], ICH_2CN [441], CH_2I_2 [442,443], CH_3I [444–447], CF_3I [142,445,448,449], C_2H_5I [450–452], cyclopropane iodide (C_3H_5I) [453], *i*-C_3H_7I [451,454], *n*-C_3H_7I [451], C_6H_5I [192,455], $(CH_3I)_2$ [456], $(CH_3I)_n$ [457]
Xe	Xe·pyrrole [168]
W	WO [390]
H_2	CH_4 [265]
OH	CH_3CH_2O [81]
CO	OCS [92,98,135,458–463], H_2CO [175–178,464], HNCO [263,465–470], HCCO [471], CH_2CO [472,473], CH_3CHO [181], CH_3COCl [380], CH_3CH_2COCl [385], dicyclopropyl ketone (C_3H_5–CO–C_3H_5) [474]
N_2	N_2* [475][a], N_2O [315,476], ClN_3 [477]
NO	NO_2 [133,299,302,303,305,351,365,478–485], Ar · NO [486], $(NO)_2$[487–493], $(CH_3)_2$–ClCNO [494], C_6H_5NO [495]
$O_2(a^1\Delta_g)$	O_3 [496]
HCl	$HCl\cdots C_2H_2$ [497]
SO	SO_2 [330]
Br_2	$COBr_2$ [402]
I_2	$(CH_3I)_2$ [498], $CF_2I{=}CF_2I$ [143]
$^3CH_2$	CH_2Cl [264]
HCO	CH_3CHO [499]
CHBr	$CHBr_3$ [411]
BrCO	$COBr_2$ [402]
CH_3	CH_3Br [403,405,500,501], CH_3I [2,102,444–446,500,502–509],CH_3SH [510,511], CH_3CHO [499], CH_3COCl [380], CH_3CH_2O [81], $(CH_3)_2S$ [512,513], CD_3SCD_3 [514], *N*-methylpyrrole (C_4H_5N) [515], $(CH_3I)_n$ [457]
CD_3	CD_3I [101, 516],
NH_3	$C_2H_2\cdots NH_3$ [517]
CF_3	CF_3I [445,142]
CF_2Cl	CF_2ClBr [408]
$CHBr_2$	$CHBr_3$ [501]
C_2H_4	CH_3CH_2O [81]
CH_2O	CH_3CH_2O [81]
C_2H_5	C_2H_5I [451]
C_3H_3	Propargyl chloride (C_3H_3Cl) [163], propargyl bromide (C_3H_3Br) [416]
C_3H_5	2-bromopropene (C_3H_5Br) [421], allyl iodide (C_3H_5I) [518]
i-C_3H_7	*i*-C_3H_7I [451,454]
n-C_3H_7	*n*-C_3H_7I [451]
C_4H_7	Cyclobutyl bromide (C_4H_7Br) [426]
CH_2CHCO	$CH_2CHCOCl$ [381]
$CH_2CHCHCH_3$	1-Bromo-2-butene ($CH_2BrCHCHCH_3$) [427]
$CH_2CHCH_2CH_2$	Cyclopropylmethyl bromide ($CH_2BrCHCH_2CH_2$) [427]
$CH_2CHCH_2CH_2$	4-Bromo-1-butene ($CH_2CHCH_2CH_2Br$) [427]
CH_3CO	CH_3COCl [379]
Ar_{15}	Ar_n ($n = 630, 680, 750$) [519]

Notes: [a]N_2*: $N_2(c'^1\Sigma_u^+,\ v=3,4)$, $N_2(c^1\Pi_u,\ v=3,4)$, $N_2(b'^1\Sigma_u^+,\ v=10,12,13,15)$.

'traditional' $(2+1_i)$ processes. Such competition occurs, for example, for HCl [25,38], HBr [131], BrCl [132] and NO_2 [133].

In Section 2.5.1 we have presented an example of a REMPI imaging study in which several ideas were illustrated. The potential of (3D) imaging has been demonstrated by outlining the full complexity of such a seemingly simple process like REMPI of the HCl molecule. For the full account of this process the reader is referred to references [13,25,38,39].

Another interesting example is the study of Baklanov *et al*. [134], where the excitation of O_2 via consequent absorption of three 205 nm femtosecond photons was used. All three absorption steps occur through repulsive states of $^3\Sigma$ symmetry. As a result, two different photon absorption sequences were observed: $(1+1_i)$ for $O_2 + 2h\nu \rightarrow O_2^+ + e^-$ and $(1+1+1_d)$ for $O_2 + 3h\nu \rightarrow O^+ + O^-$. In the latter case there is no ionisation step, since both products are ionic.

Many studies in Table 4 exhibit some interesting peculiarity. A very original mass spectrometer with split electrodes was designed to study the photodissociation of laboratory-oriented molecules with slice imaging detection of ions [101]. The performance of this technique was demonstrated by a study of the photodissociation of CD_3I molecules. Sugita et al. [135] studied the role of vibrational preexcitation in the photodissociation of OCS molecules. Some studies were done by means of photoelectron–photoion coincidence imaging [133].

4.1.2. *Photodissociation dynamics studied in the femtosecond domain*

Gas-phase studies of molecular dynamics by femtosecond time-resolved methods were pioneered by Zewail *et al*. [136,137] and were awarded the Nobel Prize in Chemistry in 1999. There exist numerous recent reviews on this subject [138] which has become a field in itself. Here we only mention recent work, where the VMI technique has been combined with a femtosecond pump probe scheme.

Detailed studies of the photodissociation of CH_3I molecules excited into the dissociative A band have been reported by Bañares *et al*. [139–141]. For every vibrational state of CH_3 the two channels producing $I(^2P_{3/2})$ and $I^*(^2P_{1/2})$ iodine atoms have been resolved in time.

Janssen *et al*. have developed a novel femtosecond photoelectron–photoion coincidence imaging machine [90], which was used to study the multi-photon multi-channel photodynamics of NO_2 [133] where the main subject of this work was to determine different REMPI pathways and their photon absorption sequences. Also, femtosecond VMI of the dissociative ionisation dynamics of CF_3I [142] and of $IF_2C\text{-}CF_2I$ [143] has been performed.

4.1.3. *Photodissociation of cations*

Photodissociation studies of cations are not included in Table 4, since here state-selective REMPI normally takes place before photodissociation, i.e. the photon absorption sequence is usually $(2+1_i+1_d)$. Photodissociation of the following cations was studied by imaging techniques: H_2^+ [144], CO^+ [145], DCl^+ [146], $BrCl^+$ [147–149], Br_2^+ [150,151], H_2S^+ [152,153], OCS^+ [154], ClN_3^+ [155], $CH_2Br_2^+$ [156], $CHBr_3^+$ [157], CBr_4^+ [158], CF_3I^+[159,160], $C_2H_4^+$ [107], CH_3COCH^+ [161], $C_2H_5Br^+$ [162], $C_3H_5Cl^+$, $C_3H_5Br^+$ [163] and Ar_n^+ $(n=2\text{–}25)$ [164,165].

The spectroscopy and the dynamics of ion pair dissociation processes, such as $H_2S + h\nu \rightarrow H^+ + SH^-$ or $CH_3Cl + h\nu \rightarrow CH_3^+ + Cl^-$ have recently been reviewed by Suits and Hepburn [166]. Such ion pair dissociations may occur in competition to usual $(2 + 1_i)$ REMPI, as reported e.g. for HCl [13,25,38,39] (Section 2.5.2).

Okino *et al.* [167] studied the photodissociation of cations via Coulomb explosion. Photoexcitation of doubly charged methanol, for example, results in a competition between different reaction channels:

$$\begin{aligned} CH_3OD^{2+} \rightarrow & CH_{3-n}OH_n \cdot D^{2+} \\ & CH_{3-n}^+ + OH_n \cdot D^{2+} \\ & CH_3D^+ + O^+ \\ & CH_2D^+ + OH^+. \end{aligned}$$

These processes were investigated by coincidence momentum imaging after having been initiated by an ultra-short intense laser field ($0.2\,PW\,cm^{-2}$ at 60 fs pulse duration). H/D migration or H/D exchange within the parent molecule was found to occur within the period of a laser pulse prior to C–O bond breaking.

Vidma *et al.* [130] studied the photodissociation of $(CH_3I)_2$ clusters at 248 nm by VMI. A cluster specific feature in this process is the presence of I_2^+ and of translationally hot I^+ ions. The comparison of the images of I^+ ions arising from the photoexcitation of CH_3I clusters with those from neutral I_2 showed that a concerted photodissociation of the ionised $(CH_3I)_2^+$ dimer is the most likely mechanism for the formation of I_2^+ ions instead of photoionisation of neutral molecular iodine. Hot I^+ ions are subsequently produced by photodissociation of the I_2^+ ions.

4.1.4. *Photodissociation of clusters*

In the past years, several VMI studies of photodissociation processes of clusters have been reported: Xe·Kr, Kr·Kr [168], X·O_2 (X = CH_3I, C_3H_6, C_6H_{12} and Xe) [169] and $(N_2O)_2$ [26]. Also, a series of studies is devoted to the photodissociation of fluorinated alkyl iodides [170–172] and benzene [173] in helium nanodroplets.

Baklanov *et al.* [169] found that the yield of oxygen atoms from the photodissociation of van der Waals complexes $X \cdot O_2$ at 226 nm is about three orders of magnitude larger than from photodissociation of free oxygen. At least five different channels producing O atoms with specific kinetic energy distributions and angular anisotropy were observed. Two main one-photon excitation pathways are proposed. The first one starts from one-photon excitation to the X–$O_2(A'^3\Delta_u)$ state, which is forbidden in the free oxygen molecule, but becomes allowed in a van der Waals complex due to admixture of the charge transfer state $^3(X^+–O_2^-)$. The second starts from direct one-photon excitation to this charge transfer state, which is rather stable and has a large UV absorption cross section. Subsequent absorption of additional photons then leads to the observed different products.

Just recently, we have studied the reaction $(N_2O)_2 + h\nu\,(193\,nm) \rightarrow N_2O \cdot N_2 \cdot O(^1D) \rightarrow 2NO + N_2$ which was initiated in $(N_2O)_2$ clusters using 3D VMI of NO products [26] for which a pronounced forward–backward scattering for the new and old NO bonds was observed (Section 2.5.2).

4.1.5. *Roaming atom elimination mechanism*

A novel elimination mechanism, the roaming H atom pathway was observed in the photodissociation of H_2CO [174–178], acetone [179] and acetaldehyde [180,181]. Besides radical pathways in which only one chemical bond is broken, in all cases molecular elimination channels were observed by VMI of the CO product:

$$H_2CO + h\nu \rightarrow H_2 + CO$$
$$CH_3CHO + h \rightarrow CO + \text{products}$$
$$(CH_3)_2CO + h \rightarrow CO + \text{products}.$$

For formaldehyde two molecular channels were identified. The first one proceeds via the well-known transition state and yields rotationally hot CO correlated with vibrationally cold H_2. As a second molecular channel, a novel mechanism was suggested involving intramolecular H abstraction, thereby entirely avoiding the region of the transition state to molecular elimination. This novel mechanism yields rotationally cold CO correlated with highly vibrationally excited H_2 [174].

An analogous molecular elimination process yielding molecular iodine I_2 from the photodissociation of CF_4I_2 was studied by Roeterdink *et al.* [143] by means of VMI in combination with femtosecond pump-probe laser excitation. The pump laser initialised the dissociation, and the probe laser interrogated the molecular system. By varying the pump-probe femtosecond delay, it was found that I_2 elimination is a concerted process, although the two C–I bonds are not broken synchronously. An electron transfer between the two iodine atoms in the parent molecule seems to be the crucial step in this fragmentation process, resulting in Coulomb attraction and creation of an ion-pair state in the molecular iodine fragment.

4.2. *Alignment and orientation*

Polarisation effects, such as alignment and orientation break the symmetry of a chemical elementary process. Therefore they are ideal systems to be studied by 3D imaging techniques where reconstruction methods employed by lower dimensionality techniques cannot be expected to yield accurate results. Those effects can either occur as an unwanted by-product in the experiment, for example if molecular alignment takes place in a supersonic beam expansion, or they can be in the focus of interest, for example if alignment of molecules in external electric or magnetic fields are to be studied.

Several kinds of polarisation are normally discussed in the literature. Among them are laser-induced alignment, polarisation of photofragments, and polarisation of products of bimolecular scattering and chemical reactions. Imaging studies of bimolecular processes where alignment of products was observed are accordingly marked in Table 5.

4.2.1. *Polarisation due to electric fields*

Alignment and orientation of molecules in a molecular beam may be achieved by static electric fields [182] or optical fields [183–187] or both of them [188]. A real breakthrough occurred a decade ago when it was realised that moderately intense laser fields can align molecules due to the interaction of their (permanent or induced) electric dipole moment

Table 5. Bimolecular processes which have been studied by imaging techniques (ED: dissociative electron collision).

Precursor	A + B → detected particle+ ⋯	Configuration[a]	References
$HI + (218\,nm) \rightarrow H$	$H + HI \rightarrow H_2(v=1) + \cdots$	↑↑	[520]
	$NO(J=1/2) + He,\ Ar \rightarrow NO + \cdots$[b]	→↑	[521–526]
$HI + (218\,nm) \rightarrow H$	$H + D_2 \rightarrow HD + \cdots$	↑↑	[527]
$Cl_2 + (355\,nm) \rightarrow 2Cl$	$Cl + CH_4(\nu_3=1),\ CHD_3(\nu_1=1) \rightarrow HCl + \cdots$[b]	↑	[209,528,529]
	$NO(J=1/2) + Ar \rightarrow NO + \cdots$	→↑	[530]
	$HCl + Ar \rightarrow HCl + \cdots$	→↑	[531]
$(ClCO)_2 + (193\,nm) \rightarrow 2Cl$	$Cl + RHOH(RH = CH_3, C_2H_5, 2\text{-}C_3H_7) \rightarrow ROH + \cdots$[c]	→↑	[532]
$(ClCO)_2 + (193\,nm) \rightarrow 2Cl$	$Cl + CH_3OH \rightarrow CH_2OH + \cdots$[c]	→↑	[532,533]
$Cl_2 + (308\,nm) \rightarrow 2Cl$	$Cl + C_2H_6 \rightarrow HCl + \cdots$	↑	[534]
	$CO + Ne \rightarrow CO + \cdots$	→↑	[535]
$SO_2 + (193\,nm) \rightarrow O$	$O + c\text{-}C_6H_{12} \rightarrow c\text{-}C_6H_{11} + \cdots$[c]	→↑	[536]
$F_2 + ED \rightarrow 2F$	$F + CH_4,\ CD_4,\ CHD_3 \rightarrow CH_3,\ CD_3 + \cdots$	→↑[d]	[95,206,537–543,228,229]
$Cl_2 + (355\,nm) \rightarrow 2Cl$	$Cl + C_2H_6,\ C_4H_{10} \rightarrow HCl + \cdots$	↑↑	[544]
$Cl_2 + (355\,nm) \rightarrow 2Cl$	$Cl + CH_3Cl,\ CH_3Br \rightarrow HCl + \cdots$	↑↑	[545]
$Cl_2 + (355\,nm) \rightarrow 2Cl$	$Cl + CH_3OH,\ CH_3OCH_3 \rightarrow HCl + \cdots$	↑↑	[546]
$Cl_2 + ED \rightarrow 2Cl$	$Cl + CH_4(CD_4) \rightarrow CH_3(CD_3) + \cdots$	→↑[d]	[230,237,547]
$Cl_2 + (355\,nm) \rightarrow 2Cl$	$Cl(^2P_{3/2,1/2}) + D_2 \rightarrow Cl(^2P_{1/2,3/2}) \cdots$	→←	[218]
$N_2O + (193\,nm) \rightarrow O^*(^1D),\ O^*(^1D) + H_2 \rightarrow OH$	$OH + CH_4,\ CHD_3,\ CD_4 \rightarrow CH_3,\ CD_3,\ CHD_2 + \cdots$	→↑[d]	[548–550]
$Cl_2 + (308\,nm) \rightarrow 2Cl$	$Cl + CH_4,\ CD_4,\ CH_2D_2 \rightarrow Cl,\ CH_3,\ CD_3 + \cdots$	↑[b]	[211]
$Cl_2 + (355\,nm) \rightarrow 2Cl$	$Cl + CH_3OH,\ CH_3Cl,\ CH_3Br \rightarrow HCl + \cdots$	↑↑	[207]
$SO_2 + (193\,nm) \rightarrow O$	$O + CD_4,\ CHD_3 \rightarrow CD_3,\ CHD_2 + \cdots$	→↑	[234]
$Cl_2 + (420\,nm) \rightarrow 2Cl$	$Cl(^2P_{3/2,1/2}) + H_2 \rightarrow Cl(^2P_{1/2,3/2}) \cdots$	→←	[551]
$Cl_2 + (308\,nm) \rightarrow 2Cl$	$Cl + C_2H_6 \rightarrow HCl + \cdots$	→↑	[552,553]
$O_2 + (157\,nm).O\ *\ (1D)$	$O^*(^1D) + HCl \rightarrow Cl(^2P_{3/2,1/2}) + \cdots$	→↑	[554,555]
$Cl_2 + ED \rightarrow 2Cl$	$Cl + CHD_3\ (\nu_1=0,1) \rightarrow CD_3 + \cdots$	→↑	[220–222]
$HBr + h\nu \rightarrow H$	$H + D_2 \rightarrow HD + \cdots$	↑	[28,29]
$Cl_2 + (355\,nm) \rightarrow 2Cl$	$Cl + C_2H_6,\ c\text{-}C_2H_4O,\ c\text{-}C_3H_6O \rightarrow HCl + \cdots$	↑[e]	[235]
$Cl_2 + (355\,nm) \rightarrow 2Cl$	$Cl + CH_3(CD_3) \rightarrow HCl + \cdots$	↑[e]	[93,556]
$F_2 + ED \rightarrow 2F$	$F + CH_2D_2 \rightarrow CHD_2 + \cdots$	→↑	[557]
$Cl_2 + ED \rightarrow 2Cl$	$Cl + CH_4(\nu_3=1) \rightarrow CH_3 + \cdots$	→↑	[219]
$Cl_2 + ED \rightarrow 2Cl$	$Cl + CH_2D_2(\nu_3=1 \text{ or } \S_6=1) \rightarrow CHD_2,\ CH_2D + \cdots$	→↑[d]	[223,224]
$Cl_2 + (355\,nm) \rightarrow \rightarrow 2Cl$	$Cl + Si(CH_3)_4 \rightarrow HCl + \cdots$	↑[e]	[558]
$O_2 + (157\,nm) \rightarrow O^*(^1D)$	$O^*(^1D) + CD_4 \rightarrow CD_3 + \cdots$	→↑	[236]
$N_2O + (193\,nm) \rightarrow O^*(^1D)$	$O^*(^1D) + D_2 \rightarrow D + \cdots$	↑	[26]

Notes: [a]The symbols ↑, →↑, ↑↑ and →← denote single beam, crossed beams, parallel beams and counter-propagating molecular beam configurations.
[b]Rotational polarisation of products was observed.
[c]The products were detected using single photon ionisation by an F_2 excimer laser at 157 nm.
[d]Evidence of resonance-mediated channel.
[e]Late mixing single beam.

and the laser field. This technique is generally applicable to all molecules (other than spherical tops). Applications of this technique include ultrafast electron or X-ray imaging [189], femtosecond time-resolved photoelectron spectroscopy [190] or laser-based methods to control the rotation of polyatomic molecules in space [191]. Here we only highlight a few selected experiments where interesting results have been obtained by an imaging technique.

Meijer *et al.* [192] achieved an unprecedented, almost ideal degree of laser-induced alignment for state-selected iodobenzene molecules. This result was achieved by using an electrostatic deflector which provided a molecular beam with all molecules in their rotational ground state.

In general, the deflection of a molecular beam by static inhomogeneous electric fields may be used, for example, to determine dipole moments and polarisabilities of different molecular systems. Thus, hexapole state selectors have recently been used for the direct determination of the sign of the NO($v=0$) dipole moment [193]. The knowledge of the sign was necessary to rule out an error in the sign of the dipole of NO as the possible source of a remarkable discrepancy between previous theoretical and experimental works on orientation effects in bimolecular collisions involving oriented NO [194]. Several examples of state selection of large molecules are given in Ref. [192].

4.2.2. *Polarisation of photofragments*

A recent review on imaging of atomic orbital polarisation in photodissociation has recently been presented by Suits and Vasyutinskii [118]. Smolin *et al.* [195] obtained a complete set of orientation parameters describing the polarisation of electronic angular momentum occurring in the photodissociation of BrCl. Photolysis of BrCl can be regarded as a benchmark system in photofragment polarisation studies. Photofragment polarisation also includes vector correlations in molecular photofragments, for example the correlation between rotational angular momentum J and recoil velocity v [196–198].

Rose *et al.* [99] have studied the predissociation of the lowest rotational states of SH/SD($A^2\Sigma^+, v=0,1,2$). The dissociation process is slow compared to rotation and is dominated by interference effects due to predissociation of states with low rotational quantum numbers prepared by photoexcitation using overlapping transitions of different parities. A strong polarisation of the S($^3P_{2,1}$) atoms was observed and explained in terms of nonadiabatic dynamics involving mixing of the $1^4\Sigma^-$ state with the $X^2\Pi_{1/2}$ state.

van den Brom *et al.* [97] have measured the polarisation of S($^1D_2$) excited atoms generated in the photolysis OCS at 223 and 230 nm. According to Bracker *et al.* [198], the photofragment angular momentum polarisation in the molecular frame may be described in terms of $a_q^{(k)}(\parallel,\perp)$ coefficients for a modified spherical harmonic expansion of the polarisation. The symbol $\parallel,\perp$ denotes a mixed (parallel and perpendicular) transition. The most important coefficient is $a_1^{(k)}(\parallel,\perp)$ which contains information on the photofragment orientation arising from the interference of dissociative states of different symmetries or the breakdown of the axial recoil approximation. van den Brom *et al.* measured this parameter for clean rovibrational states which had been prepared by a hexapole state selector. For 230 nm photolysis, the $a_1^{(k)}(\parallel,\perp)$ coefficient highly depended on the bending vibrational state of OCS, whereas for 223 nm photolysis there was no such dependence observed.

4.2.3. *Alignment in a two-photon transition*

Recently, we have proposed a new method for the determination of alignment of the molecular axis of a diatomic molecule as a result of a two-photon transition [13]. Experimentally, we have studied REMPI of jet-cooled HCl molecules in the process $HCl(X^1\Sigma^+, v''=0)+2h\nu \rightarrow HCl^*(V^1\Sigma^+, v'=12)$ around 236 nm by 3D imaging of H^+ ions and compared the 3D distributions for $Q(0)$ and $Q(1)$ rotational transitions. The $Q(0)$ transition produces HCl*(V) molecules in a rotationally unpolarised state, and the absorption of another photon results in production of H^+ ions via different pathways, with angular distributions characterised by functions $\omega_{p,\exp}(\theta, J'=0)$. The index p labels the reaction pathway upon absorption of the third photon. The $Q(1)$ transition produces HCl*(V) in a rotationally anisotropic state characterised by the functions $\omega_f(\theta, J'=1)$ and the absorption of another photon results in the production of H^+ ions via different pathways with angular distributions denoted as $\omega_{p,\exp}(\theta, J'=1)$. We proved the important relation

$$\omega_{p,\exp}(\theta, J'=1) = \omega_f(\theta, J'=1)\cdot\omega_{p,\exp}(\theta, J'=0) \tag{19}$$

Accordingly, the photofragment angular distribution produced by one or multi-photon excitation of the polarised intermediate state is given by the product of the intermediate state axis spatial distribution and the angular distribution of the photofragments from the unpolarised intermediate state. Since both functions $\omega_{p,\exp}(\theta, J'=1)$ and $\omega_{p,\exp}(\theta, J'=0)$ are measured experimentally, the function $\omega_f(\theta, J'=1)$ may easily be extracted from relation Equation (19). In practice, all three functions may be presented as a sum of Legendre polynomials with a rank $K=2$ for $\omega_f(\theta, J'=1)$ and $\omega_{p,\exp}(\theta, J'=0)$ and a rank $K=4$ for $\omega_{p,\exp}(\theta, J'=1)$. Physically, the Legendre polynomials up to the rank $K=6$ and even more may be needed to describe the angular distribution, having in mind the possible contribution from initial anisotropy in the molecular beam, alignment of molecular excited states and the following multiphoton fragmentation. However, we found that the contributions from higher rank terms are small which is why they could not accurately be extracted from the experimental data. Finally, we found, that the two-photon transition $X^1\Sigma^+ \rightarrow V^1\Sigma^+$ in HCl has clearly a perpendicular character [13].

The 3D imaging technique is also ideally suited to study the alignment of the HCl rotational angular momentum along the axis of the molecular beam prior to photon absorption. Such alignment has been observed for a variety of molecules (O_2 [199,200], N_2 [201], CO [202], N_2^+ [203], benzene [204]), and such alignment cannot *a priori* be considered to be absent. The degree of alignment can be rather large and strongly varies with the molecular speed. It is also expected to depend on the used experimental conditions [205]. If alignment occurs, observed anisotropies must be different for laser polarisations parallel and perpendicular to the molecular beam. The presence of such alignment is a serious problem for imaging methods relying on reconstruction methods. However, for the photoexcitation of HCl no alignment effects were observed.

4.3. *Bimolecular reactions*

A recent overview over successes and limitations of crossed molecular beam studies for the investigation of reactive scattering has been given by Liu [117] covering the published

literature until 2006. Therefore here we will restrict ourselves to discussing the most recent developments that have been reported since 2006.

4.3.1. *Experimental configurations*

There exist several experimental configurations for studying bimolecular processes by imaging three of which are shown in Figure 13. The first one (a) is the crossed beams configuration. Sometimes a fixed right angle for the intersection of the beams is used, but there also exist variants with counter-propagating beams. Zhou *et al*. [206] use an adjustable intersection angle allowing them to conveniently change the collision energy.

In panel (b) a variant with two non-colliding, parallel beams is depicted [207]. Finally, panel (C) shows a configuration which uses coexpansion of reactants in a single molecular beam. This configuration is sometimes called PHOTOinitiated reaction analysed by the Law Of Cosines (PHOTOLOC) [27,208–210]. It exploits the law of cosines to determine the angular distribution of detected products from the experimental velocity distribution which is blurred due to uncertainty in the direction of reactant velocities. The sensitivity of PHOTOLOC to the products is the largest, but the interpretation of the results is the most difficult [211].

Table 5 lists bimolecular processes most of which are chemical reactions studied by imaging techniques. The processes are presented in chronological order. If one of the reactants is a radical, in the first column the scheme of radical production is shown while in the second column the bimolecular process itself is specified. On the product side, only detected particles are given.

4.3.2. *A + BC triatomic benchmark reactions*

Nowadays a complete study of dynamics of a bimolecular reaction means experimental measurement of state-to-state differential cross sections at different collision energies and comparison with the predictions, obtained from quantum mechanical calculation of reactive scattering on a fully *ab initio* potential energy surface. Such complete studies have

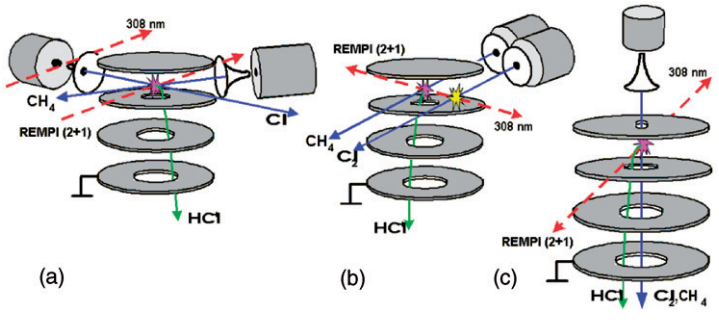

Figure 13. Three typical configurations for studying bimolecular processes by imaging: (a) crossed beams, (b) parallel beams and (c) single beam (PHOTOLOC). As example a study of the reaction $Cl + CH_4$ is shown where Cl atoms are produced by 308 nm photodissociation of Cl_2, and the HCl product is detected by (2 + 1)-REMPI. The position sensitive detector is placed at the bottom of the figure.

become possible only in the last decade due to the huge progress in computational capabilities which allow one to obtain chemically accurate (i.e. within 0.2–0.3 kcal/mol) potential energy surfaces for several benchmark systems, such as $H + H_2$, $F + H_2$, $Cl + H_2$ and $OH + H_2$. In such reactions three effects are in the focus of research. These are the geometric phase effect, i.e. the phase change of the nuclear wavefunction, when a conical intersection is encircled, the reactive resonance effect [212], and the influence of spin–orbit excitation on chemical reactivity. In this context, the term 'resonance' means a transiently formed metastable intermediate state on the pathway of the reaction.

The simplest chemical reaction is the hydrogen exchange reaction $H + H_2$ and its isotopic variants [117,213]. While for this reaction the geometric phase effect and reactive resonances can play a role, neither of these has been experimentally observed. The reaction has only recently been reinvestigated by Koszinowski *et al.* by means of VMI, where differential cross sections for the $H + D_2 \rightarrow HD(v = 1,\ J = 2,6,10) + D$ reaction channels were measured for five collision energies between 1.48 and 1.94 eV. The agreement between the experiment and the full quantum-mechanical theory is ideal. Thus, the hydrogen exchange reaction is a good example of a system where the theory yields reliable results for the whole collision-energy regime and all investigated internal product states [27]. The shapes of the differential cross sections show only a weak dependence on the collision energy, with the exception of $HD(v = 1, J = 2)$ which is bimodal at high collision energies. It was suggested that this feature results from both direct recoil and indirect scattering from the conical intersection.

The second simplest chemical reaction $F + H_2(HD, D_2)$ has never been studied by imaging techniques. Nevertheless, it is important in the context of detailed investigations of bimolecular reactions because the dynamical resonances $F + H_2 \rightarrow H + HF(v = 3)$ [214] and $F(^2P_{1/2,3/2}) + HD \rightarrow HF(v = 3) + D$ [215–217] occur in this system.

The influence of spin–orbit excitation on chemical reactivity was intensively studied by different methods before the appearance of imaging techniques. Most popular systems are $F,Cl(^2P_{1/2,3/2}) + H_2(HD, D_2)$. We know only one VMI study of Parsons *et al.* [218] in which cross sections for the inelastic collisions $Cl + D_2 \rightarrow Cl^* + D_2$ and $Cl^* + D_2 \rightarrow Cl + D_2$ were determined.

As one can see from Table 5, only few imaging studies of 'standard' $A + BC$ benchmark have been published. Instead, particular attention has been given to studies of $F,Cl,O,O(^1D) + C_nH_m$ reactions where the emphasis was laid on the influence of vibrational excitation of reactants on the reaction probability, vibrational excitation and angular distributions of products.

4.3.3. *Product-pair correlation measurement*

In the last years studies of bimolecular reactions involving polyatomic reactants often relied on state-selective REMPI detection of one of the reaction products, whereas the correlated state distribution of the coproducts was determined from a VMI high-resolution translation energy measurement of the REMPI-tagged ion from conservation of energy and momentum. This conceptually simple method is named 'product-pair correlation' measurement [95,117] and was applied, for example, to the reactions $Cl + CH_4(\nu_3 = 0, 1)$ [219], $Cl + CHD_3(\nu_1 = 0, 1)$ [220–222] and $Cl + CH_2D_2$ [223]. The most detailed study in this series is the work of Wu and Liu [223], in which $CHD_2(0_0)$ and $CH_2D(0_0)$ products were monitored by imaging for three combinations of reactant states, namely

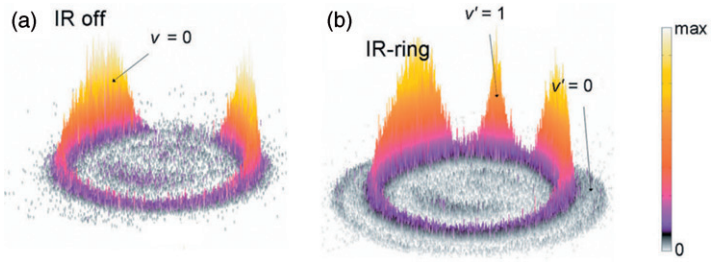

Figure 14. [Colour online] The 3D representation of the CHD_2 product raw image of the $Cl + CH_2D_2$ ($v_6 = 0, 1$) $\rightarrow HCl + CHD_2(v_i = 0)$ reaction from the study of Riedel *et al.* [224]. (a) No excitation, $v_6 = 0$. (b) CH_2D_2 molecules are excited into the $v_6 = 1$ state by radiation of an infrared laser when they pass through a multipass ring. The labels refer to the vibrational state of the HCl products. Reprinted from reference [110] with permission from AIP.

$Cl(^2P_{3/2}) + CH_2D_2(0_0)$, $Cl(^2P_{3/2}) + CH_2D_2(\nu_{bend} = 1)$ and $Cl^*(^2P_{1/2}) + CH_2D_2(0_0)$. The images allowed one to distinguish between $HCl(v = 0, 1)$ and $DCl(v = 0, 1, 2)$ states. Product pair-correlated excitation functions, vibrational branching ratios and angular distributions were obtained over a wide range of collision energies, from 2 to 22 kcal/mol. Eight different product-pair channels were observed and quantitatively characterised. From these data the direct peripheral mechanism and the reactive resonance mechanism were established as reaction mechanisms. Sometimes, different product-pair channels may easily be distinguished by their angular distributions. An interesting example of this situation is shown in Figure 14 where product raw images of the $Cl + CH_2D_2(v_6 = 0, 1)$ $HCl + CHD_2$ reaction at a collision energy of 12 kcal/mol from the study of Riedel *et al.* [224] are shown for ground ($v_6 = 0$) and preexcited ($v_6 = 1$) state CH_2D_2 reactants. CHD_2 products were detected through the 0_0^0-REMPI band near 333 nm. Hereafter the CHD_2 vibrational ground state is denoted by $v_i = 0$ whereas the labels $v = 0$, $v = 1$, $v' = 0$ and $v' = 1$ denote the vibrational states of the HCl products. Here, HCl vibrational numbers v and v' refer to reactions of Cl with CH_2D_2 in ground ($v_6 = 0$) and preexcited ($v_6 = 1$) states, respectively. As one can see from Figure 14, for the ground state reaction one observes two sideways scattered ring-like features. The strong outer one and the weak inner one correspond to the products $HCl(v = 0) + CHD_2$ and $HCl(v = 1) + CHD_2(v_i = 0)$, respectively. However, when some reactant CH_2D_2 molecules are excited to the $v_6 = 1$ state, two new contributions appear. The first one is the outermost feature for $HCl(v' = 0)$, the second one is a prominent forward peak for $HCl(v' = 1)$. Note that the second peak energetically overlaps with the $HCl(v = 0)$ peak from the ground-state reaction, but has a very different angular distribution. The analysis of such images allowed one to determine the fraction of vibrationally excited $CH_2D_2(v_6 = 1)$ molecules. This fraction increased with the intensity of the infrared pump laser, but reached an upper limit of 17% at high laser intensities.

4.3.4. *The resonant reaction mechanism*

The benchmark system for exploring mode-specific and bond-selective chemistry is the $Cl + CH_4$ reaction and its isotope variants. Zare *et al.* [209,225] found that one-quantum excitation of the ν_3 mode of CH_4 enhanced the reaction rate σ by a factor of 30 ± 15 at

a collision energy of 3.7 kcal/mol. A very recent re-investigation refined the enhancement factor to 13.4 ± 2.4: $\sigma(\nu_3 = 1) = 13.4$, $\sigma(\nu_i = 0)$. The ratio $[HCl(v = 1)]/[HCl(v = 0)]$ changed from ~ 0 for $CH_4(\nu_3 = 0)$ to ~ 0.5 for $CH_4(\nu_3 = 1)$. Also, a large difference in the HCl angular distributions was observed. While $HCl(v = 0)$ was back and sideways scattered, for $HCl(v = 1)$ a prominent forward peak was observed. Later, Crim *et al.* [226] observed a noticeable increase in the reaction cross section when two vibrational quanta of $CH_4(\nu_1 + \nu_4$ and $\nu_3 + \nu_4)$ were excited: $\sigma(\nu_1 + \nu_4) \sim 2\sigma(\nu_3 + \nu_4) \sim 20\sigma(\nu_i = 0)$ That means, an excitation of the initial C–H (or C–D) stretch leads almost exclusively to HCl (or DCl) products. Also, for the $Cl + CHD_3$ reaction it was found that $\sigma(C–H,ss) \sim 7\sigma(C–H,as)$, suggesting different pathways for the symmetric stretch (ss) and antisymmetric stretch (as) modes of excitation [227].

In the past several years there has been a break-through in elucidating the nature of reactive resonances in chemical reactions. The first reactive resonance in reactions of polyatomic molecules was observed by means of product-pair correlation measurements in the crossed beam imaging studies of $F + CH_4$ [228] and $F + CHD_3$ [229] systems. Later, experimental evidence for reactive resonances were also obtained for $Cl + CH_4$ [230], $Cl + CHD_3$ [231] and $Cl + CH_2D_2$ [223] reactions.

The nature of a reactive resonance can be easily explained for the example of the $Cl + CH_4$ reaction. Simpson *et al.* observed that the reaction rate increases strongly if the CH_4 molecule is excited in the symmetric stretching mode ν_1 [225, 226]. The origin of this enhancement in rate can be understood by examining the evolution of generalised normal mode vibrational frequencies along the reaction path (Figure 15). The interaction with an approaching Cl atom causes a rapid decrease in the C–H symmetric stretching frequency in the entrance valley. At the transition state its frequency drops to about half the starting value, which lowers the adiabatic barrier and gives rise to a significant coupling of this mode of excitation to the reaction coordinate, thus further facilitating surmounting the barrier to reaction for the colliding pair. This mechanism was first proposed by Duncan and Truong [232] from direct *ab initio* dynamics calculations. Experimentally this mechanism was confirmed by Zhang and Liu [230]. The results of their product-pair correlation measurements are shown in Figure 16. For ground state products (upper plot) the angular distribution evolves from backward near threshold to sideways with increasing collision energy, the reason mainly being a direct reaction mechanism. In contrast, the energy dependence of the angular distribution for $HCl(v = 1) + CH_3(v = 0)$ reaction products shown in the lower panel of Figure 16 is strikingly different. It changes from backward near the energetic threshold to a rather complex behaviour for large collision energies proving the existence of a reactive resonance [233,230].

The reactive resonance mechanism explains the above mentioned studies on the mode selectivity in the reaction $Cl + CH_4$. The resonant mechanism significantly contributes to the $Cl + CH_4(\nu_i = 1)$ reaction which can qualitatively account for the observed high yield and prominent forward peak of $HCl(v = 1)$. The effect is largest for the symmetric stretching mode ν_1, smaller for the symmetric ν_2 bending mode and much smaller for the asymmetric modes ν_3.

4.3.5. *Other results*

The effect of vibrational excitation of reactants was also studied for several other reactions. A study of product angular distributions for the reaction $O + CH_4$ was reported

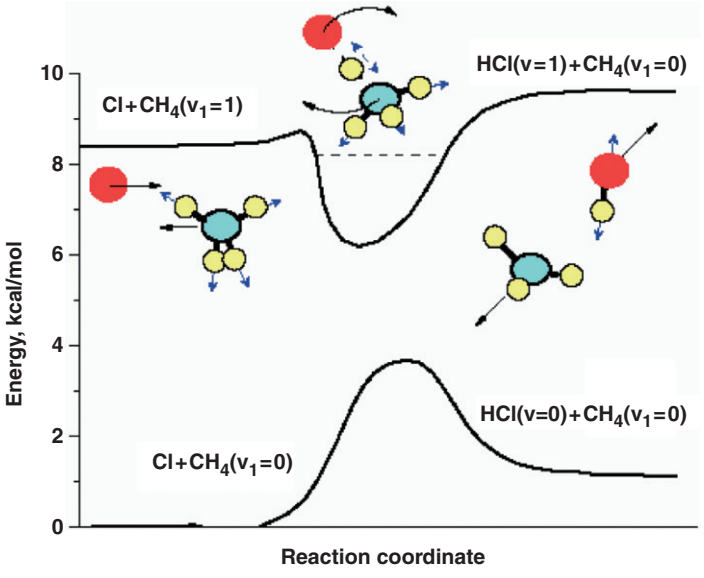

Figure 15. [Colour online] Selected vibrationally adiabatic potential energy curves along the reaction coordinate. Potential curves are based on *ab initio* calculations [232] and are approximately sketched showing the theoretically calculated vibrational frequencies. For clarity, only one high frequency excitation mode is shown. The horizontal dashed line shows the energy of the resonance state. The relative particle motion for the $Cl + CH_4(v_1 = 1) \rightarrow HCl(v' = 1) + CH_3(v_i = 0)$ reaction via the resonant mechanism is shown schematically. Adapted from reference [230] with permission from AIP.

by Zhang and Liu [234]. Although, theoretical calculations had predicted that stretching or bending excitation of CH_4 would promote chemical reactivity and that initial bending excitation of CH_4 would preferentially yield umbrella excited CH_3 products, it was observed experimentally instead that, compared to ground-state CH_4, bending excitation of methane increased vibrational excitation of the OH co-product.

The adiabatic and nonadiabatic dynamics in the $CH_3(CD_3) + HCl$ reaction was investigated by using photodissociation of CH_3I and CD_3I as sources of translationally hot methyl radicals and 2D VMI of the Cl atom products [235]. Image analysis with a Legendre moment fitting procedure demonstrated that the Cl/Cl* products are mostly forward scattered with respect to the HCl in the centre-of-mass frame but with a backward scattered component. The collision energy was found to be important for facilitating the nonadiabatic transitions that lead to Cl* production. The similarities of the Cl and Cl* channels suggest that the nonadiabatic transitions to a low-lying excited potential energy surface correlating with Cl* products occur after passage through the transition state region on the ground-state PES.

Kohguchi *et al.* studied the reaction $O^*(^1D) + CD_4$ at a collision energy of 5.6 kcal/mol [236]. They concluded that backward scattered CD_3 in low rotational states is produced by an abstraction mechanism, while forward scattered CD_3 in low rotational states is produced by an insertion mechanism via the formation of an extremely short-lived complex. Also, backward scattered CD_3 in high rotational states is produced by an

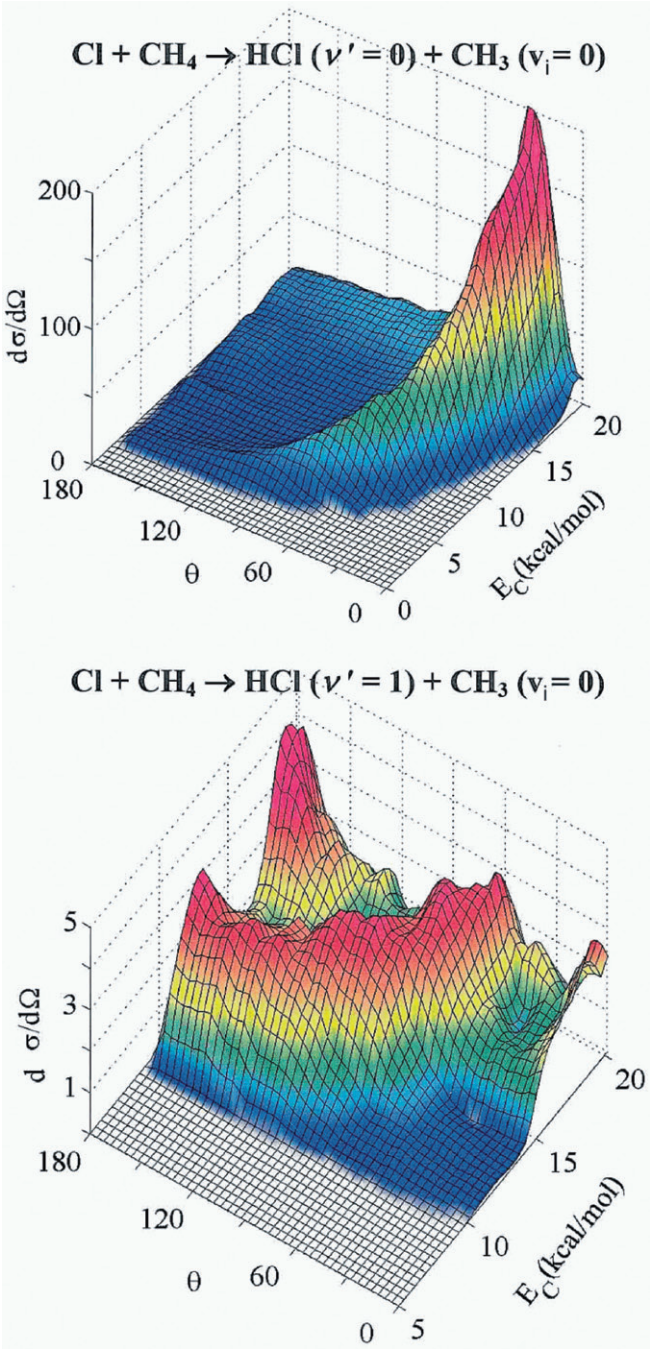

Figure 16. [Colour online] The 3D plot of differential cross sections $d\sigma/d\Omega(\theta,E_c)$ for the $Cl + CH_4 \rightarrow HCl(v' = 0, 1) + CH_3$ reaction (E_c: collision energy, θ: scattering angle). Distinct patterns suggest two dominant reaction pathways: (1) The mainly direct reaction mechanism leads to $HCl(v' = 0)$. (2) The resonant complex mechanism leads to $HCl(v' = 1)$.

insertion mechanism from an oscillating complex with a lifetime longer than its rotational period.

The effect of spin–orbit excitation of Cl atoms on their chemical reactivity was investigated in several studies. Zhou *et al*. found that the reactivity of $Cl^*(^2P_{1/2})$ towards CH_4/CD_4 is negligibly small [237]. However, in the similar system, $Cl + CH_2D_2$, significant spin–orbit reactivity of $Cl^*(^2P_{1/2})$ was discovered, and its mechanism appears to be also mediated by the resonant reaction pathway [223].

5. Conclusion and outlook

The interest to study chemical reactions in crossed beams reached the maximum in the 1980s, which was marked by the Nobel Prize of Yuan T. Lee in 1986. Imaging techniques, which are excellent for reaction dynamics studies of simple reactions at a quantum state-resolved level, appeared in this area too late, when the most fundamental features of chemical reactivity had already been established by other detection methods. However, imaging offers high resolution and state selectivity which allows one to obtain a precise quantitative description of chemical reactions. Hence it is best suited for comparing experimental scattering data to quantum mechanical calculations of reactive scattering on *ab initio* potential energy surfaces, which is of fundamental importance. Also, imaging techniques, especially the recently developed product-pair correlation measurements, allow one to understand bimolecular reaction dynamics in great detail. The recent discovery of the role of resonance mediated channels in mode-specific and bond-selective chemistry is a good example.

In the past years about 80 articles devoted to applications of imaging in gas-phase chemistry have been published each year. This number has been rather stable, with slightly less then half of these studies devoted to the photodissociation of neutral molecules. Nowadays the number of photodissociation studies decreases, but applications of VMI in new areas appear continuously. In this review, we have summarised our present knowledge of the most exciting results and developments that have occurred during the past 4 years in 2D and 3D VMI. We have tried at least to mention briefly all areas in gas-phase dynamics, where imaging techniques are being applied.

The 3D imaging is the ultimate goal of the researcher in elementary chemical dynamics. The 3D imaging is the latest development in the rapidly advancing field of imaging methods in chemical dynamics. The development of 3D imaging has been somewhat delayed with respect to the nowadays well-established 2D imaging techniques for two reasons. First, from a technical point of view, for 3D imaging technical requirements are more complex than for 2D imaging, and suitable detectors have only recently been developed. Second, from a scientific point of view, a wealth of detailed information can be and has been obtained by 2D imaging methods where 3D imaging can add little or no information to the results obtained relying on 2D techniques. One might have asked: Why bother?

Today, the technical difficulties have essentially been overcome. We have presented state of the art technologies and velocity mapping strategies which have yielded an experimental resolution of 3D imaging, which is equally as good as the experimental resolution of 2D imaging. Thus, 3D imaging offers the possibility to experimentally observe the full 3D momentum distribution of chemical reaction products paving the way

towards performing a 'complete' experiment at essentially no cost. The need to employ and rely on (possibly unreliable) mathematical reconstruction methods (Figure 1) or (possibly inapplicable) model assumptions can therefore be eliminated with relative ease. Thus, one must ask: Why should one not bother?

Of course, experimental effort associated with 3D imaging will always be larger than for 2D imaging. The application of 3D imaging is therefore indicated in those cases where one might expect to be blind for the real situation by the limitations of 2D methods. We believe that promising areas in chemical dynamics for 3D imaging studies are, for example, the study of bimolecular reactions of aligned or oriented reactants or multi-colour multi-photon polarisation spectroscopic studies of molecular fragmentation or ionisation.

As we have shown in this review, the current state of 3D imaging technology provides one with the necessary detection capabilities for such studies to be performed. As the most difficult challenge remaining for the realisation of such experiments one must regard the control over the initial reactants' conditions. Today, one has often to settle for a compromise between initial condition control and sufficiently high signal level which prevents the potential of 3D imaging to be fully utilised. Of course, there is no use in applying a highly sophisticated high resolution detection technique if the investigated system is blurred by averaging over very different start parameters. But, with the detection techniques being readily at hand, we regard it as very likely to see some major achievements in (stereo) dynamical investigations of chemical elementary processes in a not too far future, and we hope to be contributing to some small extent to this development by having compiled this review article.

Acknowledgements

Financial support by the Deutsche Forschungsgemeinschaft is gratefully acknowledged. A. I. Chichinin is also grateful to the Alexander von Humboldt Foundation for support.

References

[1] M. N. R. Ashfold, N. H. Nahler, A. J. Orr-Ewing, O. P. J. Vieuxmaire, R. L. Toomes, T. N. Kitsopoulos, I. A. Garcia, D. A. Chestakov, S.-M. Wu, and D. H. Parker, Phys. Chem. Chem. Phys. **8**, 26 (2006).
[2] D. W. Chandler and P. L. Houston, J. Chem. Phys. **87**, 1445 (1986).
[3] G. E. Busch, R. T. Mahoney, R. I. Morse, and K. R. Wilson, J. Chem. Phys. **51**, 449 (1969).
[4] Y. T. Lee, J. D. McDonald, P. R. LeBreton, and D. R. Herschbach, Rev. Sci. Instrum. **40**, 1402 (1969).
[5] M. N. R. Ashfold, I. R. Lambert, D. H. Mordaunt, G. P. Morley, and C. M. Western, J. Phys. Chem. **96**, 2938 (1992).
[6] J. L. Wiza, Nucl. Instrum. Methods **162**, 58 (1979).
[7] W. C. Wiley and I. H. McLaren, Rev. Sci. Instrum. **26**, 1150 (1955).
[8] C. Maul, T. Haas, K.-H. Gericke, and F. J. Comes, J. Chem. Phys. **102**, 3238 (1995).
[9] A. I. Chichinin, T. Einfeld, C. Maul, and K.-H. Gericke, Rev. Sci. Instrum. **73**, 1856 (2002).
[10] S. Kauczok, N. Gödecke, A. I. Chichinin, M. Veckenstedt, C. Maul, and K.-H. Gericke, Rev. Sci. Instrum. **80**, 083301 (2009).

[11] L. Dinu, A. T. J. B. Eppink, F. Rosca-Pruna, H. L. Offerhaus, W. J. van der Zande, and M. J. J. Vrakking, Rev. Sci. Instrum. **73**, 4206 (2002).
[12] A. T. B. J. Eppink and D. H. Parker, Rev. Sci. Instrum. **68**, 34 (1997).
[13] A. I. Chichinin, P. S. Shternin, N. Gödecke, S. Kauczok, C. Maul, O. S. Vasyutinskii, and K.-H. Gericke, J. Chem. Phys. **125**, 034310 (2006).
[14] I. Ali, R. Dörner, O. Jagutzki, S. Nüttgens, V. Mergel, L. Spielberger, K. Khayyat, T. Vogt, and H. Bräuning, Nucl. Instrum. Methods Phys. Res. B **149**, 490 (1999).
[15] D. H. Parker and A. T. J. B. Eppink, J. Chem. Phys. **107**, 2357 (1997).
[16] R. Dörner, V. Mergel, O. Jagutzki, L. Spielberger, J. Ullrich, R. Moshammer, and H. Schmidt-Böcking, Phys. Rep. **330**, 95 (2000).
[17] A. I. Chichinin, T. Einfeld, C. Maul, and K.-H. Gericke, Chem. Phys. Lett. **390**, 50 (2004).
[18] A. I. Chichinin, T. Einfeld, C. Maul, and K.-H. Gericke, Dokl. Phys. Chem. **402**, 96 (2005).
[19] L. Schäfer, N. Gödecke, O. Ott, C. Maul, K.-H. Gericke, P. S. Shternin, E. V. Orlenko, and O. S. Vasyutinskii, Chem. Phys. **301**, 213 (2004).
[20] A. I. Chichinin, T. Einfeld, C. Maul, and K.-H. Gericke, Dokl. Phys. Chem. **407**, 72 (2006).
[21] T. Einfeld, A. I. Chichinin, C. Maul, and K.-H. Gericke, J. Chem. Phys. **116**, 2803 (2002).
[22] T. Einfeld, A. I. Chichinin, C. Maul, and K.-H. Gericke, J. Chem. Phys. **117**, 1123 (2002).
[23] A. I. Chichinin, T. Einfeld, K.-H. Gericke, J. Grunenberg, C. Maul, and L. Schäfer, Phys. Chem. Chem. Phys. **7**, 301 (2005).
[24] T. Einfeld, A. I. Chichinin, C. Maul, and K.-H. Gericke, J. Chem. Phys. **117**, 4214 (2002).
[25] A. I. Chichinin, C. Maul, and K.-H. Gericke, J. Chem. Phys. **124**, 224324 (2006).
[26] N. Gödecke, C. Maul, A. I. Chichinin, S. Kauczok, and K.-H. Gericke, J. Chem. Phys. **131**, 054307 (2009).
[27] K. Koszinowski, N. T. Goldberg, A. E. Pomerantz, and R. N. Zare, J. Chem. Phys. **125**, 133503 (2006).
[28] N. T. Goldberg, K. Koszinowski, A. E. Pomerantz, and R. N. Zare, Chem. Phys. Lett. **433**, 439 (2007).
[29] K. Koszinowski, N. T. Goldberg, J. Zang, R. N. Zare, F. Bouakline, and S. C. Althorpe, J. Chem. Phys. **127**, 124315 (2007).
[30] S. J. Greaves, E. Wrede, N. T. Goldberg, J. Zhang, D. J. Miller, and R. N. Zare, Nature **454**, 88 (2008).
[31] N. T. Goldberg, J. Zhang, K. Koszinowski, F. Bouakline, S. C. Althorpe, and R. N. Zare, PNAS **105**, 18194 (2008).
[32] O. K. Yoon, M. D. Robbins, I. A. Zuleat, G. K. Barbula, and R. N. Zare, Anal. Chem. **80**, 8299 (2008).
[33] D. Strasser, X. Urbain, H. B. Pedersen, N. Altstein, O. Heber, R. Wester, K. G. Bhushan, and D. Zajfman, Rev. Sci. Instrum. **71**, 3092 (2000).
[34] R. E. Continetti, Ann. Rev. Phys. Chem. **52**, 165 (2001).
[35] D. S. Green, G. A. Bickel, and S. C. Wallace, J. Mol. Spectrosc. **150**, 303 (1991).
[36] D. S. Green, G. A. Bickel, and S. C. Wallace, J. Mol. Spectrosc. **150**, 354 (1991).
[37] D. S. Green, G. A. Bickel, and S. C. Wallace, J. Mol. Spectrosc. **150**, 388 (1991).
[38] C. Romanescu, S. Manzhos, D. Boldovsky, J. Clarke, and H.-P. Loock, J. Chem. Phys. **120**, 767 (2004).
[39] S. Manzhos, C. Romanescu, H.-P. Loock, and J. G. Underwood, J. Chem. Phys. **121**, 11802 (2004).
[40] A. Kvaran, H. Wang, K. Matthiasson, A. Bodi, and E. Jonsson, J. Chem. Phys. **129**, 164313 (2008).
[41] N. Goldstein, G. D. Greenblatt, and D. R. Wiesenfeld, Chem. Phys. Lett. **83**, 21 (1983).
[42] X. B. Wang, H. Z. Li, Q. H. Zhu, F. N. Kong, and H. G. Yu, J. Chin. Chem. Soc. **42**, 399 (1995).
[43] H. Akagi, Y. Fujimura, and O. Kajimoto, J. Chem. Phys. **111**, 115 (1999).
[44] G. Hancock and V. Haverd, Phys. Chem. Chem. Phys. **5**, 2369 (2003).

[45] F. Green, G. Hancock, A. J. Orr-Ewing, M. Brouard, S. P. Duxon, P. A. Enriquez, R. Sayos, and J. P. Simons, Chem. Phys. Lett. **182**, 568 (1991).
[46] M. Brouard, S. P. Duxon, P. A. Enriquez, R. Sayos, and J. P. Simons, J. Phys. Chem. **95**, 8169 (1991).
[47] M. Brouard, S. P. Duxon, P. A. Enriquez, and J. P. Simons, J. Chem. Phys. **97**, 7414 (1992).
[48] H. Akagi, Y. Fujimura, and O. Kajimoto, J. Chem. Soc. Faraday Trans. **94**, 1575 (1998).
[49] H. Tsurumaki, Y. Fujimura, and O. Kajimoto, J. Chem. Phys. **111**, 592 (1999).
[50] S. Kawai, Y. Fujimura, O. Kajimoto, and T. Takayanagi, J. Chem. Phys. **120**, 6430 (2004).
[51] K. Honma and O. Kajimoto, Chem. Phys. Lett. **117**, 123 (1985).
[52] K. Honma, Y. Fujimura, O. Kajimoto, and G. Inoue, J. Chem. Phys. **88**, 4739 (1988).
[53] K. Honma and O. Kajimoto, Chem. Phys. Lett. **117**, 123 (1985).
[54] D. J. Ruggieri, IEEE Nucl. Sci. **19**, 74 (1972).
[55] M. Lampton and F. Paresce, Rev. Sci. Instrum. **45**, 1098 (1974).
[56] P. J. C. M. Nowak, H. H. Holsboer, W. Heubers, R. W. W. van Resandt, and J. Los, Int. J. Mass Spectrom. Ion Phys. **34**, 375 (1980).
[57] W. Aberth, Int. J. Mass Spectrom. Ion Phys. **37**, 379 (1981).
[58] H. H. Tuithof, A. J. H. Boerboom, and H. L. C. Meuzelaar, Int. J. Mass Spectrom. Ion Phys. **17**, 299 (1975).
[59] J. H. Beynon, D. O. Jones, and R. G. Cooks, Anal. Chem. **47**, 1734 (1975).
[60] G. Griffin, R. Britten, H. Boettger, J. Conley, and D. Norris, Proceedings of the 27th Ann. Conference on Mass Spectrometry and Allied Topics, 714 Seattle, USA (1979).
[61] J. J. Czyzewski, T. E. Madey, and J. T. Yates, Phys. Rev. Let. **32**, 777 (1974).
[62] M. Galanti, R. Gott, and J. F. Renaud, Rev. Sci. Instrum. **42**, 1818 (1971).
[63] R. S. Gao, P. S. Gibner, J. H. Newman, K. A. Smith, and R. F. Stebbings, Rev. Sci. Instrum. **55**, 1756 (1984).
[64] E. Lienard, M. Herbane, G. Ban, G. Darius, P. Delahaye, D. Durand, X. Flechard, M. Labalme, F. Mauger, and A. Mery, Nucl. Instrum. Methods Phys. Res. A **551**, 375 (2005).
[65] T. Horio and T. Suzuki, Rev. Sci. Instrum. **80**, 13706 (2009).
[66] S. Loechner, Ph. D. thesis, Max-Planck-Institute for Nuclear Physics, Heidelberg, 2006.
[67] N. Saito, F. Heiser, O. Hemmers, K. Wieliczek, J. Viefhaus, and U. Becker, Phys. Rev. A **54**, 2004 (1996).
[68] J. Becker, K. Beckord, U. Werner, and H. Lutz, Nucl. Instrum. Meth. Phys. Res. A **337**, 409 (1999).
[69] M. Lampton, O. Siegmund, and R. Raffanti, Rev. Sci. Instrum. **58**, 2298 (1987).
[70] S. E. Sobottka and M. B. Williams, IEEE Trans. Nucl. Sci. **35**, 348 (1988).
[71] Z. Amitay and D. Zajfman, Rev. Sci. Instrum. **68**, 1387 (1997).
[72] I. Ali, R. Dörner, O. Jagutzki, S. Nuttgens, V. Mergel, L. Spielberger, K. Khayyat, T. Vogt, H. Bräuning, and K. Ullmann, Nucl. Instrum. Methods Phys. Res. B **149**, 490 (1999).
[73] O. Jagutzki, V. Mergel, K. Ullmann-Pfleger, L. Spielberger, U. Spillmann, R. Dörner, and H. Schmidt-Böcking, Nucl. Instrum. Meth. Phys. Res. B **477**, 244 (2002).
[74] E. Gagnon, A. S. Sandhu, A. Paul, K. Hagen, A. Czasch, T. Jahnke, P. Ranitovic, C. L. Cocke, B. Walker, and M. M. Murnane, Rev. Sci. Instrum. **79**, 063102 (2008).
[75] I. Thomann, R. Lock, V. Sharma, E. Gagnon, S. T. Pratt, H. C. Kapteyn, M. M. Murnane, and W. Li, J. Phys. Chem. A **112**, 9382 (2008).
[76] O. Jagutzki, J. S. Lapington, L. B. C. Worth, U. Spillman, V. Mergel, and H. Schmidt-Böcking, Nucl. Instrum. Meth. Phys. Res. B **477**, 256 (2002).
[77] D. L. Osborn, P. Zou, H. Johnsen, C. C. Hayden, C. A. Taatjes, V. D. Knyazev, S. W. North, D. S. Peterka, M. Ahmed, and S. R. Leone, Rev. Sci. Instrum. **79**, 104103 (2008).
[78] C. Martin, P. Jelinsky, M. Lampton, R. F. Malina, and H. O. Anger, Rev. Sci. Instrum. **52**, 1067 (1981).
[79] W. Li, S. D. Chambreau, S. A. Lahankar, and A. G. Suits, Rev. Sci. Instrum. **76**, 063106 (2005).

[80] A. A. Hoops, J. R. Gascooke, A. E. Faulhaber, K. E. Kautzman, and D. M. Neumark, J. Chem. Phys. **120**, 7901 (2004).
[81] A. E. Faulhaber, D. E. Szpunar, K. E. Kautzman, and D. M. Neumark, J. Phys. Chem. A **109**, 10239 (2005).
[82] A. E. Faulhaber, J. R. Gascooke, A. A. Hoops, and D. M. Neumark, J. Chem. Phys. **124**, 204303 (2006).
[83] D. E. Szpunar, K. E. Kautzman, A. E. Faulhaber, and D. M. Neumark, J. Chem. Phys. **124**, 054318 (2006).
[84] K. E. Kautzman, P. E. Crider, D. E. Szpunar, and D. M. Neumark, J. Phys. Chem. A **111**, 12795 (2007).
[85] D. E. Szpunar, A. E. Faulhaber, K. E. Kautzman, P. E. Crider II, and D. M. Neumark, J. Chem. Phys. **126**, 114311 (2007).
[86] A. A. Hoops, J. R. Gascooke, A. E. Faulhaber, K. E. Kautzman, and D. M. Neumark, Chem. Phys. Lett. **374**, 235 (2003).
[87] D. Zajfman, O. Heber, and D. Strasser, in *Imaging in Molecular Dynamics: Technology and Applications*, edited by B. J. Whitaker (University Press, Cambridge, 2003), pp. 122–137.
[88] G. D. Costa, F. Vurpillot, A. Bostel, M. Bouet, and B. Deconihout, Rev. Sci. Instrum. **76**, 13304 (2005).
[89] B. Deconihout, F. Vurpillot, B. Gault, G. D. Costa, M. Bouet, A. Bostel, D. Blavette, A. Hideur, G. Martel, and M. Brunel, Surf. Interface Anal. **39**, 278 (2007).
[90] A. Vredenborg, W. G. Roeterdink, and M. H. M. Janssen, Rev. Sci. Instrum. **79**, 063108 (2008).
[91] T. P. Rakitzis and T. N. Kitsopoulos, in *Imaging in Molecular Dynamics: Technology and Applications*, edited by B. J. Whitaker (University Press, Cambridge, 2003), pp. 227–245.
[92] B. D. Leskiw, M. H. Kim, G. E. Hall, and A. G. Suits, Rev. Sci. Instrum. **76**, 104101 (2005).
[93] B. Retail, S. J. Greaves, J. K. Pearce, R. A. Rose, and A. J. Orr-Ewing, Phys. Chem. Chem. Phys. **9**, 3261 (2007).
[94] D. Townsend, M. P. Minitti, and A. G. Suits, Rev. Sci. Instrum. **74**, 2530 (2003).
[95] J. J. Lin, J. Zhou, W. Shiu, and K. Liu, Rev. Sci. Instrum. **74**, 2495 (2003).
[96] E. Wrede, S. Laubach, S. Schulenberg, A. J. Orr-Ewing, E. A. Brown, and M. N. R. Ashfold, J. Chem. Phys. **114**, 2629 (2001).
[97] A. J. van den Brom, T. P. Rakitzis, and M. H. M. Janssen, J. Chem. Phys. **123**, 164313 (2005).
[98] M. L. Lipciuc and M. H. M. Janssen, Phys. Chem. Chem. Phys. **8**, 3007 (2006).
[99] R. A. Rose, A. J. Orr-Ewing, C.-H. Yang, K. Vidma, G. C. Groenenboom, and D. H. Parker, J. Chem. Phys. **130**, 034307 (2009).
[100] G. A. Garcia, L. Nahon, C. J. Harding, E. A. Mikajlo, and I. Powis, Rev. Sci. Instrum. **76**, 053302 (2005).
[101] M. L. Lipciuc, A. J. van den Brom, L. Dinu, and M. H. M. Janssen, Rev. Sci. Instrum. **76**, 123103 (2005).
[102] R. de Nalda, J. G. Izquierdo, J. Dura, and L. Banares, J. Chem. Phys. **126**, 021101 (2007).
[103] H. L. Offerhaus, C. Nicole, F. Lepine, C. Bordas, F. Rosca-Pruna, and M. J. J. Vrakking, Rev. Sci. Instrum. **72**, 3245 (2001).
[104] V. Papadakis and T. N. Kitsopoulos, Rev. Sci. Instrum. **77**, 083101 (2006).
[105] L. Rubio-Lago, D. Zaouris, Y. Sakellariou, D. Sofikitis, T. N. Kitsopoulos, F. Wang, X. Yang, B. Cronin, A. L. Devine, G. A. King, M. G. D. Nix, and M. N. R. Ashfold, J. Chem. Phys. **127**, 064306 (2007).
[106] B. D. Leskiw, M. H. Kim, G. E. Hall, and A. G. Suits, Rev. Sci. Instrum. **76**, 129901 (2005).
[107] M. H. Kim, B. D. Leskiw, and A. G. Suits, J. Phys. Chem. A **109**, 7839 (2005).
[108] M. H. Kim, B. D. Leskiw, L. Shen, and A. G. Suits, Int. J. Mass Spectrom. **252**, 73 (2006).
[109] M. J. J. Vrakking, A. S. Bracker, T. Suzuki, and Y. T. Lee, Rev. Sci. Instrum. **64**, 645 (1993).

[110] A. E. Pomerantz and R. N. Zare, Chem. Phys. Lett. **370**, 515 (2003).
[111] J. Riedel, S. Dziarzhytski, A. Kuczmann, F. Renth, and F. Temps, Chem. Phys. Lett. **414**, 473 (2005).
[112] P. C. Samartzis, B. L. G. Bakker, T. P. Rakitzis, D. H. Parker, and T. N. Kitsopoulos, J. Chem. Phys. **110**, 5201 (1999).
[113] I. V. Hertel and W. Radlo, Rep. Prog. Phys. **69**, 1897 (2006).
[114] P. L. Houston, B. R. Cosofret, A. Dixit, S. M. Dylewski, J. D. Geiser, J. A. Mueller, R. J. Wilson, P. J. Pisano, M. S. Westley, and K. T. Lorenz, J. Chin. Chem. Soc. **48**, 309 (2001).
[115] D. Townsend, W. Li, S. K. Lee, R. L. Gross, and A. G. Suits, J. Phys. Chem. A **109**, 8661 (2005).
[116] A. G. Suits and J. W. Hepburn, Ann. Rev. Phys. Chem. **57**, 431 (2006).
[117] K. Liu, J. Chem. Phys. **125**, 132307 (2006).
[118] A. G. Suits and O. S. Vasyutinskii, Chem. Rev. **108**, 3706 (2008).
[119] D. M. Neumark, Ann. Rev. Phys. Chem. **52**, 255 (2001).
[120] T. Seideman, Ann. Rev. Phys. Chem. **53**, 41 (2002).
[121] A. Sanov and W. C. Lineberger, Phys. Chem. Comm. **5**, 165 (2002).
[122] T. Suzuki, Ann. Rev. Phys. Chem. **57**, 555 (2006).
[123] D. M. Neumark, J. Chem. Phys. **125**, 132303 (2006).
[124] D. M. Neumark, J. Phys. Chem. A **112**, 13287 (2008).
[125] D. M. Neumark, Mol. Phys. **106**, 2183 (2008).
[126] A. Sanov and R. Mabbs, Int. Rev. Phys. Chem. **27**, 53 (2008).
[127] W. Li, L. Poisson, D. S. Peterka, M. Ahmed, R. R. Lucchese, and A. G. Suits, Chem. Phys. Lett. **374**, 334 (2003).
[128] S.-T. Tsai, C.-K. Lin, Y. T. Lee, and C.-K. Ni, Rev. Sci. Instrum. **72**, 1963 (2001).
[129] C.-K. Ni, C.-M. Tseng, M.-F. Lin, and Y. A. Dyakov, J. Phys. Chem. B **111**, 12631 (2007).
[130] K. V. Vidma, A. V. Baklanov, E. B. Khvorostov, V. N. Ishchenko, S. A. Kochubei, A. T. J. B. Eppink, D. A. Chestakov, and D. H. Parker, J. Chem. Phys. **122**, 204301 (2005).
[131] C. Romanescu and H.-P. Loock, J. Chem. Phys. **127**, 124304 (2007).
[132] O. Vieuxmaire, N. Nahler, R. Dixon, and M. N. R. Ashfold, Phys. Chem. Chem. Phys. **9**, 5531 (2007).
[133] A. Vredenborg, W. G. Roeterdink, and M. H. M. Janssen, J. Chem. Phys. **128**, 204311 (2008).
[134] A. V. Baklanov, L. M. C. Janssen, D. H. Parker, L. Poisson, B. Soep, J.-M. Mestdagh, and O. Gobert, J. Chem. Phys. **129**, 214306 (2008).
[135] A. Sugita, M. Mashino, M. Kawasaki, G. Trott-Kriegeskorte, Y. Matsumi, R. Bersohn, and K.-H. Gericke, J. Chem. Phys. **112**, 7095 (2000).
[136] A. H. Zewail, Science **242**, 1645 (1988).
[137] A. H. Zewail, J. Phys. Chem. A **104**, 5660 (2000).
[138] I. V. Hertel and W. Radloff, Rep. Prog. Phys. **69**, 1897 (2006).
[139] R. de Nalda, J. G. Izquierdo, J. Dura, and L. Banares, J. Chem. Phys. **126**, 021101 (2007).
[140] J. Dura, R. de Nalda, J. Alvarez, J. G. Izquierdo, G. A. Amaral, and L. Banares, ChemPhysChem **9**, 1245 (2008).
[141] R. de Nalda, J. Dura, A. Garcia-Vela, J. G. Izquierdo, J. Gonzalez-Vazquez, and L. Banares, J. Chem. Phys. **128**, 244309 (2008).
[142] W. G. Roeterdink and M. H. M. Janssen, Phys. Chem. Chem. Phys. **4**, 601 (2002).
[143] W. G. Roeterdink, A. M. Rijs, and M. H. M. Janssen, J. Am. Chem. Soc. **128**, 576 (2006).
[144] I. Ben-Itzhak, P. Wang, J. Xia, A. M. Sayler, M. A. Smith, J. W. Maseberg, K. D. Carnes, B. D. Esry, and J. Macdonald, Nucl. Instrum. Methods Phys. Res. B **233**, 56 (2005).
[145] W. Li, S. A. Lahankar, C. Huang, P. S. Shternin, O. S. Vasyutinskii, and A. G. Suits, Phys. Chem. Chem. Phys. **8**, 2950 (2006).
[146] A. D. Webb, N. H. Nahler, R. N. Dixon, and M. N. R. Ashfold, J. Chem. Phys. **125**, 204312 (2006).

[147] O. P. J. Vieuxmaire, N. H. Nahler, J. R. Jones, R. N. Dixon, and M. N. R. Ashfold, Mol. Phys. **103**, 2437 (2005).
[148] O. P. J. Vieuxmaire, N. H. Nahler, J. R. Jones, R. N. Dixon, and M. N. R. Ashfold, Mol. Phys. **103**, 1677 (2005).
[149] N. H. Nahler, O. P. J. Vieuxmaire, J. R. Jones, M N.R. Ashfold, A. T. J. B. Eppink, A. M. Coriou, and D. H. Parker, J. Phys. Chem. A **108**, 8077 (2004).
[150] M. Beckert, S. J. Greaves, and M. N. R. Ashfold, Phys. Chem. Chem. Phys. **5**, 308 (2003).
[151] O. P. J. Vieuxmaire, M. G. D. Nix, J. A. J. Fitzpatrick, R. N. Dixon, M. Beckert, and M. N. R. Ashfold, Phys. Chem. Chem. Phys. **6**, 543 (2004).
[152] A. D. Webb, N. Kawanaka, R. N. Dixon, and M. N. R. Ashfold, J. Chem. Phys. **127**, 224308 (2007).
[153] A. D. Webb, R. N. Dixon, and M. N. R. Ashfold, J. Chem. Phys. **127**, 224307 (2007).
[154] C. Chang, C.-Y. Luo, and K. Liu, J. Phys. Chem. A **109**, 1022 (2005).
[155] N. Hansen, A. M. Wodtke, A. V. Komissarov, K. Morokuma, and M. C. Heaven, J. Chem. Phys. **118**, 10485 (2003).
[156] J. H. Huang, D. D. Xu, W. H. Fink, and W. M. Jackson, J. Chem. Phys. **115**, 6012 (2001).
[157] J. Huang, D. Xu, J. S. Francisco, and W. M. Jackson, J. Chem. Phys. **118**, 3083 (2003).
[158] J. R. Greene, J. S. Francisco, J. Huang, D. Xu, and W. M. Jackson, J. Chem. Phys. **121**, 5868 (2004).
[159] F. Aguirre and S. T. Pratt, J. Chem. Phys. **118**, 6318 (2003).
[160] F. Aguirre and S. T. Pratt, J. Chem. Phys. **118**, 9467 (2003).
[161] W. M. Jackson and D. Xu, J. Chem. Phys. **113**, 3651 (2000).
[162] D. D. Xu, R. J. Price, J. H. Huang, and W. M. Jackson, Z. Phys. Chem. **215**, 253 (2001).
[163] L. R. McCunn, D. I. G. Bennett, L. J. Butler, H. Fan, F. Aguirre, and S. T. Pratt, J. Phys. Chem. A **110**, 843 (2006).
[164] J. A. Smith, J. Winkel, N. G. Gotts, A. J. Stace, and B. J. Whitaker, J. Phys. Chem. **96**, 9696 (1992).
[165] J. A. Smith, N. G. Gotts, J. F. Winkel, R. Hallett, C. A. Woodward, A. J. Stace, and B. J. Whitaker, J. Chem. Phys. **97**, 397 (1992).
[166] A. G. Suits and J. W. Hepburn, Ann. Rev. Phys. Chem. **57**, 431 (2006).
[167] T. Okino, Y. Furukawa, P. Liu, T. Ichikawa, R. Itakura, K. Hoshina, K. Yamanouchi, and H. Nakano, J. Phys. B: At. Mol. Opt. Phys. **39**, S515 (2006).
[168] L. Rubio-Lago, D. Zaouris, Y. Sakellariou, D. Sofikitis, T. N. Kitsopoulos, F. Wang, X. Yang, B. Cronin, A. L. Devine, G. A. King, M. G. D. Nix, M. N. R. Ashfold, and S. S. Xantheas, J. Chem. Phys. **127**, 064306 (2007).
[169] A. V. Baklanov, G. A. Bogdanchikov, K. V. Vidma, D. A. Chestakov, and D. H. Parker, J. Chem. Phys. **126**, 124316 (2007).
[170] A. Braun and M. Drabbels, J. Chem. Phys. **127**, 114303 (2007).
[171] A. Braun and M. Drabbels, J. Chem. Phys. **127**, 114304 (2007).
[172] A. Braun and M. Drabbels, J. Chem. Phys. **127**, 114305 (2007).
[173] E. Loginov, A. Braun, and M. Drabbels, Phys. Chem. Chem. Phys. **10**, 6107 (2008).
[174] A. G. Suits, S. D. Chambreau, and S. A. Lahankar, Int. Rev. Phys. Chem. **26**, 585 (2007).
[175] S. D. Chambreau, D. Townsend, S. A. Lahankar, S. K. Lee, and A. G. Suits, Phys. Scr. **73**, C89 (2006).
[176] S. A. Lahankar, S. D. Chambreau, D. Townsend, F. Suits, J. Farnum, X. Zhang, J. M. Bowman, and A. G. Suits, J. Chem. Phys. **125**, 044303 (2006).
[177] S. A. Lahankar, S. D. Chambreau, X. Zhang, J. M. Bowman, and A. G. Suits, J. Chem. Phys. **126**, 044314 (2007).
[178] D. Townsend, S. A. Lahankar, S. K. Lee, S. D. Chambreau, A. G. Suits, X. Zhang, J. Rheinecker, L. B. Harding, and J. M. Bowman, Science **306**, 1158 (2004).
[179] V. Goncharov, N. Herath, and A. G. Suits, J. Phys. Chem. A **112**, 9423 (2008).

[180] P. L. Houston and S. H. Kable, Proceed. NAS **103**, 16079 (2006).
[181] L. Rubio-Lago, G. A. Amaral, A. Arregui, J. G. Izquierdo, F. Wang, D. Zaouris, T. N. Kitsopoulos, and L. Bañares, Phys. Chem. Chem. Phys. **9**, 6123 (2007).
[182] H. J. Loesch and J. Remscheid, J. Chem. Phys. **93**, 4779 (1990).
[183] B. Friedrich and D. Herschbach, Phys. Rev. Lett. **74**, 4623 (1995).
[184] H. Stapelfeldt and T. Seideman, Rev. Mod. Phys. **75**, 543 (2003).
[185] V. Kumarappan, C. Z. Bisgaard, S. S. Viftrup, L. Holmegaard, and H. Stapelfeldt, J. Chem. Phys. **125**, 194309 (2006).
[186] T. Seideman and E. Hamilton, Adv. At. Mol. Opt. Phys3. **52**, 289 (2006).
[187] D. Herschbach, Eur. Phys. J. D **38**, 3 (2006).
[188] B. Friedrich and D. Herschbach, J. Phys. Chem. A **103**, 10280 (1999).
[189] J. C. H. Spence and R. B. Doak, Phys. Rev. Lett. **92**, 198102 (2004).
[190] O. Gessner, A. M. D. Lee, J. P. Shaffer, H. Reisler, S. V. Levchenko, A. I. Krylov, J. G. Underwood, H. Shi, A. L. L. East, D. M. Wardlaw, E. T. H. Chrysostom, C. C. Hayden, and A. Stolow, Science **311**, 219 (2006).
[191] S. S. Viftrup, V. Kumarappan, S. Trippel, H. Stapelfeldt, E. Hamilton, and T. Seideman, Phys. Rev. Lett. **99**, 143602 (2007).
[192] L. Holmegaard, J. H. Nielsen, I. Nevo, H. Stapelfeldt, F. Filsinger, J. Kupper, and G. Meijer, Phys. Rev. Lett. **102**, 023001 (2009).
[193] A. Gijsbertsen, W. Siu, M. F. Kling, P. Johnsson, P. Jansen, S. Stolte, and M. J. J. Vrakking, Phys. Rev. Lett. **99**, 13003 (2007).
[194] H. Gijsbertsen, G. Rus, A. E. Wiskerke, S. Stolte, D. W. Chandler, and J. Klos, J. Chem. Phys. **123**, 224305 (2005).
[195] A. G. Smolin, O. S. Vasyutinskii, O. P. J. Vieuxmaire, M. N. R. Ashfold, G. G. Balint-Kurti, and A. J. Orr-Ewing, J. Chem. Phys. **124**, 94305 (2006).
[196] A. S. Bracker, E. R. Wouters, A. G. Suits, Y. T. Lee, and O. S. Vasyutinskii, Phys. Rev. Lett. **80**, 1626 (1998).
[197] Y. Wang, H. P. Loock, J. Cao, and C. X. W. Qian, J. Chem. Phys. **102**, 808 (1995).
[198] A. S. Bracker, E. R. Wouters, A. G. Suits, and O. S. Vasyutinskii, J. Chem. Phys. **110**, 6749 (1999).
[199] V. Aquilanti, D. Ascenzi, D. Cappelletti, and F. Pirani, Nature **371**, 399 (1994).
[200] V. Aquilanti, D. Ascenzi, D. Cappelletti, and F. Pirani, J. Phys. Chem. **99**, 1362 (1995).
[201] V. Aquilanti, D. Ascenzi, D. Cappelletti, R. Fedeli, and F. Pirani, J. Phys. Chem. A **101**, 7648 (1997).
[202] S. Harich and A. M. Wodtke, J. Chem. Phys. **107**, 5983 (1997).
[203] E. B. Anthony, W. Schade, M. J. Bastian, V. M. Bierbaum, and S. R. Leone, J. Chem. Phys. **106**, 5413 (1997).
[204] F. Pirani, D. Cappelletti, M. Bartolomei, V. Aquilanti, M. Scotoni, M. Vescovi, D. Ascenzi, and D. Bassi, Phys. Rev. Lett. **86**, 5035 (2001).
[205] V. Aquilanti, D. Ascenzi, M. de Castro Vítores, F. Pirani, and D. Cappelletti, J. Chem. Phys. **111**, 2620 (1999).
[206] J. G. Zhou, J. J. Lin, W. C. Shiu, S. C. Pu, and K. Liu, J. Chem. Phys. **119**, 2538 (2003).
[207] C. Murray, J. K. Pearce, S. Rudic, B. Retail, and A. J. Orr-Ewing, J. Phys. Chem. A **109**, 11093 (2005).
[208] N. E. Shafer, A. J. Orr-Ewing, W. R. Simpson, H. Xu, and R. N. Zare, Chem. Phys. Lett. **212**, 155 (1993).
[209] W. R. Simpson, A. J. Orr-Ewing, T. P. Rakitzis, S. A. Kandel, and R. N. Zare, J. Chem. Phys. **103**, 7299 (1995).
[210] T. P. Rakitzis and T. N. Kitsopoulos, in *Imaging in Molecular Dynamics: Technology and Applications*, edited by B. J. Whitaker (University Press, Cambridge, 2003), pp. 217–226.

[211] M. Bass, M. Brouard, R. Cireasa, A. Clark, and C. Vallance, J. Chem. Phys. **123**, 094301 (2005).
[212] R. D. Levine and S.-F. Wu, Chem. Phys. Lett. **11**, 557 (1971).
[213] K. Liu, Ann. Rev. Phys. Chem. **52**, 139 (2001).
[214] D. M. Neumark, A. M. Wodtke, G. N. Robinson, C. C. Hayden, and Y. T. Lee, J. Chem. Phys. **82**, 3045 (1985).
[215] F. Dong, S.-H. Lee, and K. Liu, J. Chem. Phys. **124**, 224312 (2006).
[216] S.-H. Lee, F. Dong, and K. Liu, J. Chem. Phys. **125**, 133106 (2006).
[217] S.-H. Lee, F. Dong, and K. Liu, Faraday Discuss. **127**, 49 (2004).
[218] B. F. Parsons and D. W. Chandler, J. Chem. Phys. **122**, 174306 (2005).
[219] H. Kawamata, S. Tauro, and K. Liu, Phys. Chem. Chem. Phys. **10**, 4378 (2008).
[220] S. Yan, Y.-T. Wu, and K. Liu, Phys. Chem. Chem. Phys. **9**, 250 (2007).
[221] S. Yan and K. Liu, Chinese J. Chem. Phys. **20**, 333 (2007).
[222] J. Riedel and K. Liu, J. Phys. Chem. A **113**, 4249 (2009).
[223] Y.-T. Wu and K. Liu, J. Chem. Phys. **129**, 154302 (2008).
[224] J. Riedel, S. Yan, H. Kawamata, and K. Liu, Rev. Sci. Instrum. **79**, 033105 (2008).
[225] W. R. Simpson, T. P. Rakitzis, S. A. Kandel, T. Lev-On, and R. N. Zare, J. Phys. Chem. **100**, 7938 (1996).
[226] S. Yoon, S. Henton, A. N. Zivkovic, and F. F. Crim, J. Chem. Phys. **116**, 10744 (2002).
[227] S. Yoon, R. J. Holiday, E. L. Sibert III, and F. F. Crim, J. Chem. Phys. **119**, 9568 (2003).
[228] J. G. Zhou, J. J. Lin, and K. P. Liu, J. Chem. Phys. **121**, 813 (2004).
[229] W. Shiu, J. J. Lin, and K. Liu, Phys. Rev. Lett. **92**, 103201 (2004).
[230] B. Zhang and K. Liu, J. Chem. Phys. **122**, 101102 (2005).
[231] S. Yan, Y.-T. Wu, B. Zhang, X.-F. Yue, and K. Liu, Science **316**, 1723 (2007).
[232] W. T. Duncan and T. N. Truong, J. Chem. Phys. **103**, 9642 (1995).
[233] W. R. Simpson, A. J. Orr-Ewing, and R. N. Zare, Chem. Phys. Lett. **212**, 163 (1993).
[234] B. Zhang and K. Liu, J. Phys. Chem. A **109**, 6791 (2005).
[235] J. K. Pearce, B. Retail, S. J. Greaves, R. A. Rose, and A. J. Orr-Ewing, J. Phys. Chem. A **111**, 13296 (2007).
[236] H. Kohguchi, Y. Ogi, and T. Suzuki, Phys. Chem. Chem. Phys. **10**, 7222 (2008).
[237] J. Zhou, J. J. Lin, B. Zhang, and K. Liu, J. Phys. Chem. A **108**, 7832 (2004).
[238] B. Lescovar and C. C. Lo, IEEE Trans. Nucl. Sci. NS-25, 582 (1978).
[239] M. A. Buntine, D. P. Baldwin, and D. W. Chandler, J. Chem. Phys. **96**, 5843 (1992).
[240] K. Ito, R. I. Hall, and M. Ukai, J. Chem. Phys. **104**, 8449 (1996).
[241] B. L. G. Bakker, D. H. Parker, P. C. Samartzis, and T. N. Kitsopoulos, J. Chem. Phys. **113**, 9044 (2000).
[242] B. L. G. Bakker, D. H. Parker, and W. J. van der Zande, Phys. Rev. Lett. **86**, 3272 (2001).
[243] F. Aguirre and S. T. Pratt, J. Chem. Phys. **121**, 9855 (2004).
[244] D. C. Radenovic, A. J. A. van Roij, S.-M. Wu, J. J. ter Meulen, D. H. Parker, M. P. J. van der Loo, L. M. C. Janssen, and G. C. Groenenboom, Mol. Phys. **106**, 557 (2008).
[245] D. C. Radenovic, A. J. A. van Roij, D. A. Chestakov, A. T. J. B. Eppink, J. J. ter Meulen, D. H. Parker, M. P. J. van der Loo, G. C. Groenenboom, M. E. Greenslade, and M. I. Lester, J. Chem. Phys. **119**, 9341 (2003).
[246] C. Romanescu and H.-P. Loock, J. Chem. Phys. **127**, 124304 (2007).
[247] S. A. Huang, M. H. Kim, B. Zhang, and A. G. Suits, Phys. Chem. Chem. Phys. **8**, 4652 (2006).
[248] W. Huang, M. H. Kim, and A. G. Suits, J. Chem. Phys. **125**, 121101 (2006).
[249] P. M. Regan, D. Ascenzi, E. Wrede, M. N. R. Ashfold, P. A. Cook, and A. J. Orr-Ewing, Phys. Chem. Chem. Phys. **2**, 5364 (2000).
[250] D. H. Parker, R. F. Delmdahl, B. Bakker, and H.-P. Loock, J. Chin. Chem. Soc. **48**, 327 (2001).
[251] S. Manzhos, H. P. Loock, B. L. G. Bakker, and D. H. Parker, J. Chem. Phys. **117**, 9347 (2002).

[252] U. Müller, T. Eckert, M. Braun, and H. Helm, Phys. Rev. Lett. **83**, 2718 (1999).
[253] R. Reichle, I. Mistrik, U. Müller, and H. Helm, Phys. Rev. A **60**, 3929 (1999).
[254] M. Brown, M. Beckert, and U. Müller, Rev. Sci. Instrum. **71**, 4535 (2000).
[255] I. Mistrik, R. Reichle, H. Helm, and U. Müller, Phys. Rev. A **60**, 2711 (2001).
[256] R. Mistrik, H. Helm, and U. Müller, Phys. Rev. A **60**, 3929 (2001).
[257] U. Galster, P. Kaminski, M. Beckert, H. Helm, and U. Müller, Eur. Phys. J., D **17**, 307 (2001).
[258] L. J. Rogers, M. N. R. Ashfold, Y. Matsumi, M. Kawasaki, and B. J. Whitaker, J. Chem. Soc. Faraday Trans. **92**, 5181 (1996).
[259] M. L. Hause, Y. H. Yoon, and F. F. Crim, J. Chem. Phys. **125**, 174309 (2006).
[260] M. L. Hause, Y. H. Yoon, and F. F. Crim, Mol. Phys. **106**, 1127 (2008).
[261] D. P. Baldwin, M. A. Buntine, and D. W. Chandler, J. Chem. Phys. **93**, 6578 (1990).
[262] L. R. Valachovic, M. F. Tuchler, M. Dulligan, T. Droz-Georget, M. Zyrianov, A. Kolessov, H. Reisler, and C. Wittig, J. Chem. Phys. **112**, 2752 (2000).
[263] A. Sanov, T. Droz-Georget, M. Zyrianov, and H. Reisler, J. Chem. Phys. **106**, 7013 (1997).
[264] V. Dribinski, A. B. Potter, A. V. Demyanenko, and H. Reisler, J. Chem. Phys. **115**, 7474 (2001).
[265] A. J. R. Heck, R. N. Zare, and D. W. Chandler, J. Chem. Phys. **104**, 3399 (1996).
[266] A. J. R. Heck, R. N. Zare, and D. W. Chandler, J. Chem. Phys. **104**, 4019 (1996).
[267] M. Ahmed, D. S. Peterka, and A. G. Suits, J. Chem. Phys. **110**, 4248 (1999).
[268] M. Mashino, H. Yamada, A. Sugita, and M. Kawasaki, J. Photochem. Photobiol. A **176**, 78 (2005).
[269] W. M. Jackson, R. J. Price, D. D. Xu, J. D. Wrobel, M. Ahmed, D. S. Peterka, and A. G. Suits, J. Chem. Phys. **109**, 4703 (1998).
[270] D.-S. Ahn, J. Lee, J.-M. Choi, K.-S. Lee, S. J. Baek, K. Lee, K.-K. Baeck, and S. K. Kim, J. Chem. Phys. **128**, 224305 (2008).
[271] A. J. van den Brom, M. Kapelios, T. N. Kitsopoulos, N. H. Nahler, B. Cronin, and M. N. R. Ashfold, Phys. Chem. Chem. Phys. **7**, 892 (2005).
[272] M. L. Lipciuc, F. Wang, X. Yang, T. N. Kitsopoulos, G. S. Fanourgakis, and S. S. Xantheas, ChemPhysChem **9**, 1838 (2008).
[273] J. Wei, A. Kuczmann, J. Riedel, F. Renth, and F. Temps, Phys. Chem. Chem. Phys. **5**, 315 (2003).
[274] J. Wei, J. Riedel, A. Kuczmann, F. Renth, and F. Temps, Faraday Discuss. **127**, 267 (2004).
[275] J. H. Zhang, B. Jiang, X. M. Yang, and J. C. Xie, Chem. Phys. Lett. **364**, 80 (2002).
[276] M. Schneider, C. Schon, I. Fischer, L. Rubio-Lago, and T. Kitsopoulos, Phys. Chem. Chem. Phys. **9**, 6021 (2007).
[277] M. L. Hause, Y. H. Yoon, A. S. Case, and F. F. Crim, J. Chem. Phys. **128**, 104307 (2008).
[278] M. Schneider, R. Maksimenka, F. J. Buback, T. Kitsopoulos, L. Rubio-Lago, and I. Fischer, Phys. Chem. Chem. Phys. **8**, 3017 (2006).
[279] M. Kawasaki, A. Sugita, C. Ramos, Y. Matsumi, and H. Tachikawa, J. Phys. Chem. A **108**, 8119 (2004).
[280] B. L. G. Bakker and D. H. Parker, Chem. Phys. Lett. **330**, 293 (2000).
[281] N. Hansen and A. M. Wodtke, Chem. Phys. Lett. **356**, 340 (2002).
[282] B. R. Cosofret, H. M. Lambert, and P. L. Houston, J. Chem. Phys. **117**, 8787 (2002).
[283] R. E. Continetti, D. R. Cyr, R. B. Metz, and D. M. Neumark, Chem. Phys. Lett. **182**, 406 (1991).
[284] B. R. Cosofret, H. M. Lambert, and P. L. Houston, Bull. Korean Chem. Soc. **23**, 179 (2002).
[285] H. M. Lambert, E. W. Davis, O. Tokel, A. A. Dixit, and P. L. Houston, J. Chem. Phys. **122**, 174304 (2005).
[286] B. L. G. Bakker, A. T. J. B. Eppink, D. H. Parker, M. L. Costen, G. Hancock, and G. A. D. Ritchie, Chem. Phys. Lett. **283**, 319 (1998).

[287] B. L. G. Bakker, D. H. Parker, G. Hancock, and G. A. D. Ritchie, Chem. Phys. Lett. **294**, 565 (1998).
[288] M. Brouard, R. Cireasa, A. P. Clark, F. Quadrini, and C. Vallance, Phys. Chem. Chem. Phys. **8**, 5549 (2006).
[289] H. Kim, K. S. Dooley, S. W. North, G. E. Hall, and P. L. Houston, J. Chem. Phys. **125**, 133316 (2006).
[290] A. T. J. B. Eppink and D. H. Parker, Rev. Sci. Instrum. **68**, 3484 (1997).
[291] B. Buijsse, W. J. van der Zande, A. T. J. B. Eppink, D. H. Parker, B. R. Lewis, and S. T. Gibson, J. Chem. Phys. **108**, 7229 (1998).
[292] B. L. G. Bakker and D. H. Parker, J. Chem. Phys. **112**, 4037 (2000).
[293] D. H. Parker, Acc. Chem. Res. **33**, 563 (2000).
[294] H. M. Lambert, A. A. Dixit, E. W. Davis, and P. L. Houston, J. Chem. Phys. **121**, 10437 (2004).
[295] H. Kim, K. S. Dooley, G. C. Groenenboom, and S. W. North, Phys. Chem. Chem. Phys. **8**, 2964 (2006).
[296] H. Kim, K. S. Dooley, E. R. Johnson, and S. W. North, J. Chem. Phys. **124**, 134304 (2006).
[297] J. M. Teule, G. C. Groenenboom, D. W. Neyer, D. W. Chandler, and M. H. M. Janssen, Chem. Phys. Lett. **320**, 177 (2000).
[298] M. Brouard, A. P. Clark, C. Vallance, and O. S. Vasyutinskii, J. Chem. Phys. **119**, 771 (2003).
[299] K. Tonokura and T. Suzuki, Chem. Phys. Lett. **224**, 1 (1994).
[300] M. Brouard, R. Cireasa, A. P. Clark, T. J. Preston, and C. Vallance, J. Chem. Phys. **124**, 064309 (2006).
[301] A. M. Coroiu, D. H. Parker, G. C. Groenenboom, J. Barr, I. T. Novalbos, and B. J. Whitaker, Eur. Phys. J. D **38**, 151 (2006).
[302] I. Wilkinson and B. J. Whitaker, J. Chem. Phys. **129**, 154312 (2008).
[303] V. P. Hradil, T. Suzuki, S. A. Hewitt, P. L. Houston, and B. J. Whitaker, J. Chem. Phys. **99**, 4455 (1993).
[304] M. Ahmed, D. S. Peterka, A. S. Bracker, O. Vasyutinskii, and A. G. Suits, J. Chem. Phys. **110**, 4115 (1999).
[305] A. V. Demyanenko, V. Dribinski, H. Reisler, H. Meyer, and C. X. W. Qian, J. Chem. Phys. **111**, 7383 (1999).
[306] M. Brouard, A. Goman, S. J. Horrocks, A. J. Johnsen, F. Quadrini, and W.-H. Yuen, J. Chem. Phys. **127**, 144304 (2007).
[307] R. J. Wilson, J. A. Mueller, and P. L. Houston, J. Phys. Chem. A **101**, 7593 (1997).
[308] J. D. Geiser, S. M. Dylewski, J. A. Mueller, R. J. Wilson, R. Toumi, and P. L. Houston, J. Chem. Phys. **112**, 1279 (2000).
[309] B. Jones, J. Zhou, L. Yang, and C. Y. Ng, Rev. Sci. Instrum. **79**, 123106 (2008).
[310] R. Cosofret, S. M. Dylewski, and P. L. Houston, J. Phys. Chem. A **104**, 10240 (2000).
[311] M. Brouard, R. Cireasa, A. P. Clark, T. J. Preston, C. Vallance, G. C. Groenenboom, and O. S. Vasyutinskii, J. Phys. Chem. A **108**, 7965 (2004).
[312] R. F. Delmdahl, B. L. G. Bakker, and D. H. Parker, J. Chem. Phys. **112**, 5298 (2000).
[313] R. F. Delmdahl, D. H. Parker, and A. T. J. B. Eppink, J. Chem. Phys. **114**, 8339 (2001).
[314] A. T. J. B. Eppink, D. H. Parker, M. H. M. Janssen, B. Buijsse, and W. J. van der Zande, J. Chem. Phys. **108**, 1305 (1998).
[315] H. Kawamata, H. Kohguchi, T. Nishide, and T. Suzuki, J. Chem. Phys. **125**, 133312 (2006).
[316] T. Suzuki, H. Katayanagi, Y. X. Mo, and K. Tonokura, Chem. Phys. Lett. **256**, 90 (1996).
[317] M. Ahmed, E. R. Wouters, D. S. Peterka, O. S. Vasyutinskii, and A. G. Suits, Faraday Discuss. **113**, 425 (1999).
[318] D. W. Neyer, A. J. R. Heck, D. W. Chandler, J. M. Teule, and M. H. M. Janssen, J. Phys. Chem. A **103**, 10388 (1999).
[319] R. F. Delmdahl, B. L. G. Bakker, and D. H. Parker, J. Chem. Phys. **113**, 7728 (2000).

[320] T. Nishide and T. Suzuki, J. Phys. Chem. A **108**, 7863 (2004).
[321] A. G. Smolin, O. S. Vasyutinskii, E. R. Wouters, and A. G. Suits, J. Chem. Phys. **121**, 6759 (2004).
[322] M. Brouard, R. Cireasa, A. P. Clark, G. C. Groenenboom, G. Hancock, S. J. Horrocks, F. Quadrini, G. A. D. Ritchie, and C. Vallance, J. Chem. Phys. **125**, 133308 (2006).
[323] S. Kyoung Lee, D. Townsend, O. S. Vasyutinskii, and A. G. Suits, Phys. Chem. Chem. Phys. **7**, 1650 (2005).
[324] S. Kyoung Lee, D. Townsend, O. S. Vasyutinskii, and A. G. Suits, Phys. Chem. Chem. Phys. **7**, 1650 (2005).
[325] N. Taniguchi, K. Takahashi, Y. Matsumi, S. M. Dylewski, J. D. Geiser, and P. L. Houston, J. Chem. Phys. **111**, 6350 (1999).
[326] S. M. Dylewski, J. D. Geiser, and P. L. Houston, J. Chem. Phys. **115**, 7460 (2001).
[327] D. A. Chestakov, S.-M. Wu, G. Wu, D. H. Parker, A. T. J. B. Eppink, and T. N. Kitsopoulos, J. Phys. Chem. A **108**, 8100 (2004).
[328] M. Brouard, F. Quadrini, and C. Vallance, J. Chem. Phys. **127**, 084305 (2007).
[329] H. Katayanagi, Y. X. Mo, and T. Suzuki, Chem. Phys. Lett. **247**, 571 (1995).
[330] A. A. Dixit, Y. Lei, K. W. Lee, E. Quinones, and P. L. Houston, J. Phys. Chem. A **109**, 1770 (2005).
[331] P. C. Samartzis and T. N. Kitsopoulos, J. Phys. Chem. A **101**, 5620 (1997).
[332] T. P. Rakitzis, P. C. Samartzis, and T. N. Kitsopoulos, J. Chem. Phys. **111**, 10415 (1999).
[333] T. N. Kitsopoulos, C. R. Gebhardt, and T. P. Rakitzis, J. Chem. Phys. **115**, 9727 (2001).
[334] T. P. Rakitzis, P. C. Samartzis, and T. N. Kitsopoulos, Phys. Rev. Lett. **87**, 123001 (2001).
[335] T. P. Rakitzis, Chem. Phys. Lett. **342**, 121 (2001).
[336] L. M. C. Janssen, M. P. J. van der Loo, G. C. Groenenboom, S.-M. Wu, D. C. Radenovic, A. J. A. van Roij, I. A. Garcia, and D. H. Parker, J. Chem. Phys. **126**, 094304 (2007).
[337] M. Brouard, A. V. Green, F. Quadrini, and C. Vallance, J. Chem. Phys. **127**, 084304 (2007).
[338] S. K. Lee, R. Silva, S. Thamanna, O. S. Vasyutinskii, and A. G. Suits, J. Chem. Phys. **125**, 144318 (2006).
[339] Y. X. Mo, H. Katayanagi, M. C. Heaven, and T. Suzuki, Phys. Rev. Lett. **77**, 830 (1996).
[340] T. Suzuki, H. Katayanagi, S. Nanbu, and M. Aoyagi, J. Chem. Phys. **109**, 5778 (1998).
[341] S. Manzhos and H.-P. Loock, Comp. Phys. Comm. **154**, 76 (2003).
[342] M. H. Kim, W. Li, S. K. Lee, and A. G. Suits, Can. J. Chem. **82**, 880 (2004).
[343] D. Townsend, S. K. Lee, and A. G. Suits, Chem. Phys. **301**, 197 (2004).
[344] S.-M. Wu, X. Yang, and D. H. Parker, Mol. Phys. **103**, 1797 (2005).
[345] T. P. Rakitzis, P. C. Samartzis, R. L. Toomes, L. Tsigaridas, M. Coriou, D. Chestakov, A. T. J. B. Eppink, D. H. Parker, and T. N. Kitsopoulos, Chem. Phys. Lett. **364**, 115 (2002).
[346] T. P. Rakitzis, P. C. Samartzis, R. L. Toomes, T. N. Kitsopoulos, A. Brown, G. G. Balint-Kurti, O. S. Vasyutinskii, and J. A. Beswick, Science **300**, 1936 (2003).
[347] H. Kim, J. Park, T. C. Niday, and S. W. North, J. Chem. Phys. **123**, 174303 (2005).
[348] C. R. Gebhardt, T. P. Rakitzis, P. C. Samartzis, V. Ladopoulos, and T. N. Kitsopoulos, Rv. Sci. Instrum. **72**, 3848 (2001).
[349] P. C. Samartzis, B. L. G. Bakker, T. P. Rakitzis, D. H. Parker, and T. N. Kitsopoulos, J. Chem. Phys. **110**, 5201 (1999).
[350] H. Kawamata, H. Kohguci, T. Nishide, and T. Suzuki, J. Chem. Phys. **125**, 133312 (2006).
[351] P. C. Samartzis, T. Gougousi, and T. N. Kitsopoulos, Laser Chem. **17**, 185 (1997).
[352] P. C. Samartzis, I. Sakellariou, T. Gougousi, and T. N. Kitsopoulos, J. Chem. Phys. **107**, 43 (1997).
[353] D. H. Parker, B. L. G. Bakker, P. C. Samartzis, and T. N. Kitsopoulos, J. Chem. Phys. **115**, 1205 (2001).
[354] A. Sugita, K. Suto, M. Kawasaki, and Y. Matsumi, Chem. Phys. Lett. **340**, 83 (2001).
[355] T. P. Rakitzis and T. N. Kitsopoulos, J. Chem. Phys. **116**, 9228 (2002).

[356] M. J. Bass, M. Brouard, A. P. Clark, C. Vallance, and B. Martinez-Haya, Phys. Chem. Chem. Phys. **5**, 856 (2003).
[357] O. P. J. Vieuxmaire, N. Nahler, R. N. Dixon, and M. N. R. Ashfold, Phys. Chem. Chem. Phys. **9**, 5531 (2007).
[358] M. J. Cooper, P. J. Jackson, L. J. Rogers, A. J. Orr-Ewing, M. N. R. Ashfold, and B. J. Whitaker, J. Chem. Phys. **109**, 4367 (1998).
[359] M. S. Park, Y. J. Jung, S. H. Lee, D. C. Kim, and K. H. Jung, Chem. Phys. Lett. **322**, 429 (2000).
[360] E. R. Wouters, M. Beckert, L. J. Russell, M. N. R. Ashfold, K. N. Rosser, A. J. Orr-Ewing, and O. S. Vasyutinskii, J. Chem. Phys. **117**, 2087 (2002).
[361] M. Beckert, E. R. Wouters, M. N. R. Ashfold, and E. Wrede, J. Chem. Phys. **119**, 9576 (2003).
[362] L. J. Rogers, M. N. R. Ashfold, Y. Matsumi, M. Kawasaki, and B. J. Whitaker, Chem. Phys. Lett. **258**, 159 (1996).
[363] T. P. Rakitzis, S. A. Kandel, A. J. Alexander, Z. H. Kim, and R. N. Zare, J. Chem. Phys. **110**, 3351 (1999).
[364] Y. Tanaka, M. Kawasaki, Y. Matsumi, H. Fujiwara, T. Ishiwata, L. J. Rogers, R. N. Dixon, and M. N. R. Ashfold, J. Chem. Phys. **109**, 1315 (1998).
[365] V. Skorokhodov, Y. Sato, K. Suto, Y. Matsumi, and M. Kawasaki, J. Phys. Chem. **100**, 12321 (2000).
[366] M. Kawasaki, K. Suto, Y. Sato, Y. Matsumi, and R. Bersohn, J. Phys. Chem. **100**, 19853 (1996).
[367] M. J. Bass, M. Brouard, A. P. Clark, and C. Vallance, J. Chem. Phys. **117**, 8723 (2002).
[368] A. B. Potter, V. Dribinski, A. Demyanenko, and H. Reisler, Chem. Phys. Lett. **349**, 257 (2001).
[369] P. C. Samartzis, N. Hansen, and A. M. Wodtke, Phys. Chem. Chem. Phys. **8**, 2958 (2006).
[370] N. Hansen and A. M. Wodtke, J. Phys. Chem. A **107**, 10608 (2003).
[371] D. Townsend, S. K. Lee, and A. G. Suits, J. Phys. Chem. A **108**, 8106 (2004).
[372] J. Zhou, K.-C. Lau, E. Hassanein, H. Xu, S.-X. Tian, B. Jones, and C. Y. Ng, J. Chem. Phys. **124**, 034309 (2006).
[373] S. H. Lee, Y. J. Jung, and K.-H. Jung, Chem. Phys. **260**, 143 (2000).
[374] S. H. Lee and K. H. Jung, Chem. Phys. Lett. **350**, 306 (2001).
[375] A. Yokoyama, K. Yokoyama, and T. Takayanagi, J. Chem. Phys. **114**, 1617 (2001).
[376] Y. J. Jung, M. S. Park, Y. S. Kim, K.-H. Jung, and H. R. Volpp, J. Chem. Phys. **111**, 4005 (1999).
[377] K. Tonokura, L. B. Daniels, T. Suzuki, and K. Yamashita, J. Phys. Chem. A **101**, 7754 (1997).
[378] M. S. Park, K. W. Lee, and K.-H. Jung, J. Chem. Phys. **114**, 10368 (2001).
[379] X. Tang, B. J. Ratli., B. L. FitzPatrick, and L. J. Butler, J. Phys. Chem. B **112**, 16050 (2008).
[380] S. Deshmukh, J. D. Myers, S. S. Xantheas, and W. P. Hess, J. Phys. Chem. **98**, 12535 (1994).
[381] K.-C. Lau, Y. Liu, and L. J. Butler, J. Chem. Phys. **123**, 054322 (2005).
[382] M. J. Bell, K.-C. Lau, M. J. Krisch, D. I. G. Bennett, L. J. Butler, and F. Weinhold, J. Phys. Chem. A **111**, 1762 (2007).
[383] E.J. Glassman and L.J. Butler, 235th ACS National Meeting in Abstracts of Papers, Department of Chemistry, The University of Chicago, Chicago, IL, USA, New Orleans, LA, United States, 2008.
[384] Y. Liu and L. J. Butler, J. Chem. Phys. **121**, 11016 (2004).
[385] Z.-R. Wei, X.-P. Zhang, W.-B. Lee, B. Zhang, and K.-C. Lin, J. Chem. Phys. **130**, 014307 (2009).
[386] M. J. Krisch, M. J. Bell, B. L. FitzPatrick, L. R. McCunn, K.-C. Lau, Y. Liu, and L. J. Butler, J. Phys. Chem. A **111**, 5968 (2007).
[387] A. S. Raman, M. Justine Bell, K.-C. Lau, and L. J. Butler, J. Chem. Phys. **127**, 154316 (2007).
[388] B. L. Fitzpatrick, K.-C. Lau, L. J. Butler, S.-H. Lee, and J. J.-M. Lin, J. Chem. Phys. **129**, 084301 (2008).

[389] R. L. Gross, X. H. Liu, and A. G. Suits, Chem. Phys. Lett. **362**, 229 (2002).
[390] D. A. Chestakov, A. Zawadzka, D. H. Parker, K. V. Vidma, A. V. Baklanov, and S. A. Kochubei, Rev. Sci. Instrum. **76**, 026102 (2005).
[391] A. J. R. Heck, D. W. Neyer, R. N. Zare, and D. W. Chandler, J. Phys. Chem. **99**, 17700 (1995).
[392] D. A. Chestakov, D. H. Parker, and A. V. Baklanov, J. Chem. Phys. **122**, 084302 (2005).
[393] T. P. Rakitzis, P. C. Samartzis, R. L. Toomes, and T. N. Kitsopoulos, J. Chem. Phys. **121**, 7222 (2004).
[394] M. J. Cooper, E. Wrede, A. J. Orr-Ewing, and M. N. R. Ashfold, J. Chem. Soc. Faraday Trans. **94**, 2901 (1998).
[395] Y. J. Jee, M. S. Park, Y. S. Kim, Y. J. Jung, and K.-H. Jung, Chem. Phys. Lett. **287**, 701 (1998).
[396] P. C. Samartzis, T. N. Kitsopoulos, and M. N. R. Ashfold, Phys. Chem. Chem. Phys. **2**, 453 (2000).
[397] Y.-J. Jee, Y.-J. Jung, and K.-H. Jung, J. Chem. Phys. **115**, 9739 (2001).
[398] E. Wrede, E. R. Wouters, M. Beckert, R. N. Dixon, and M. N. R. Ashfold, J. Chem. Phys. **116**, 6064 (2002).
[399] Y. S. Kim, Y. J. Jung, and K.-H. Jung, J. Chem. Phys. **107**, 3805 (1997).
[400] E. Wrede, S. Laubach, S. Schulenburg, A. J. Orr-Ewing, and M. N. R. Ashfold, Chem. Phys. Lett. **326**, 22 (2000).
[401] C. Huang, W. Li, R. Silva, and A. G. Suits, Chem. Phys. Lett. **426**, 242 (2006).
[402] D. D. Xu, J. H. Huang, J. S. Francisco, J. C. Hansen, and W. M. Jackson, J. Chem. Phys. **117**, 7483 (2002).
[403] V. Blanchet, P. C. Samartzis, and A. M. Wodtke, J. Chem. Phys. **130**, 034304 (2009).
[404] W. P. Hess, D. W. Chandler, and J. W. Thoman, Chem. Phys. **163**, 277 (1992).
[405] T. Gougousi, P. C. Samartzis, and T. N. Kitsopoulos, J. Chem. Phys. **108**, 5742 (1998).
[406] J. Zhou, K. C. Lau, E. Hassanein, H. Xu, J. Huang, and W. M. Jackson, J. Chem. Phys. **125**, 133311 (2006).
[407] T. K. Kim, M. S. Park, K. W. Lee, and K.-H. Jung, J. Chem. Phys. **115**, 10745 (2001).
[408] J. H. Huang, D. D. Xu, J. S. Francisco, and W. M. Jackson, J. Chem. Phys. **119**, 3661 (2003).
[409] L. Ji, Y. Tang, R. Zhu, Z. Wei, and B. Zhang, Spectrochim. Acta A **67**, 273 (2007).
[410] M. S. Park, T. K. Kim, and S. H. Lee, J. Phys. Chem. A **105**, 5606 (2001).
[411] D. D. Xu, J. S. Francisco, J. Huang, and W. M. Jackson, J. Chem. Phys. **117**, 2578 (2002).
[412] J. R. Greene, J S. Francisco, D. Xu, J. Huang, and W. M. Jackson, J. Chem. Phys. **125**, 133311 (2006).
[413] K.-S. Lee, K. W. Lee, T. K. Kim, R. Ryoo, and K.-H. Jung, J. Chem. Phys. **122**, 034308 (2005).
[414] G. J. Mains, L. M. Raff, and S. A. Abrash, J. Phys. Chem. **99**, 3532 (1995).
[415] H. Katayanagi, N. Yonekuira, and T. Suzuki, Chem. Phys. **231**, 345 (1998).
[416] H. Fan and S. T. Pratt, J. Chem. Phys. **124**, 144313 (2006).
[417] H. Shen, L. Hua, Z. Cao, C. Hu, and B. Zhang, Opt. Commun. **282**, 387 (2009).
[418] K. W. Lee, Y. J. Jee, and K.-H. Jung, J. Chem. Phys. **116**, 4490 (2002).
[419] Y. Tang, L. Ji, R. Zhu, Z. Wei, and B. Zhang, ChemPhysChem **6**, 2137 (2005).
[420] L. Hua, H. Shen, C. Zhang, Z. Cao, and B. Zhang, Chem. Phys. Lett. **460**, 50 (2008).
[421] H. Fan, S. T. Pratt, and J. A. Miller, J. Chem. Phys. **127**, 144301 (2007).
[422] L. Ji, Y. Tang, R. Zhu, Z. Wei, and B. Zhang, J. Chem. Phys. **125**, 164307 (2006).
[423] Z. Wei, Y. Wang, Q. Zheng, Z. Zhao, and B. Zhang, Opt. Commun. **281**, 287 (2008).
[424] K.-S. Lee, K. Y. Yeon, K.-H. Jung, and S. K. Kim, J. Phys. Chem. A **112**, 9312 (2008).
[425] Y. Tang, L. Ji, R. Zhu, Z. Wei, and B. Zhang, J. Phys. Chem. A **109**, 11123 (2005).
[426] Y. Liu, K.-C. Lau, and L. J. Butler, J. Phys. Chem. A **110**, 5379 (2006).
[427] K.-C. Lau, Y. Liu, and L. J. Butler, J. Chem. Phys. **125**, 144312 (2006).

[428] X.-P. Zhang, Z.-R. Wei, Y. Tang, T.-J. Chao, B. Zhang, and K.-C. Lin, ChemPhysChem. **9**, 1130 (2004).
[429] Y. Tang, W.-B. Lee, B. Zhang, and K.-C. Lin, J. Phys. Chem. A **112**, 1421 (2008).
[430] P.-J. Liu, B. Tang, and B. Zhang, Chem. Phys. **340**, 141 (2007).
[431] B. Tang and B. Zhang, Chem. Phys. Lett. **412**, 145 (2005).
[432] C. Zhang, Z. Cao, L. Hua, Y. Chen, and B. Zhang, Chem. Phys. Lett. **454**, 171 (2008).
[433] Z. Wei, Y. Tang, Q. Zheng, and B. Zhang, Opt. Commun. **265**, 532 (2006).
[434] H. Qu, H. Li, F. Liang, and B. A. Zhang, Chem. Phys. **330**, 355 (2006).
[435] H.-P. Loock, B. L. G. Bakker, and D. H. Parker, Can. J. Phys. **79**, 211 (2001).
[436] K. S. Dooley, J. N. Geidosch, and S. W. North, Chem. Phys. Lett. **457**, 303 (2008).
[437] Y. Wang, S. Zhang, Z. Wei, and B. Zhang, Chem. Phys. Lett. **468**, 14 (2009).
[438] H. Yamada, N. Taniguchi, M. Kawasaki, Y. Matsumi, and R. J. Gordon, J. Chem. Phys. **117**, 1130 (2002).
[439] D. A. Chestakov, D. H. Parker, K. V. Vidma, and T. P. Rakitzis, J. Chem. Phys. **124**, 024315 (2006).
[440] S. Unny, Y. Du, L. C. Zhu, R. J. Gordon, A. Sugita, M. Kawasaki, Y. Matsumi, and T. Seideman, Phys. Rev. Lett. **86**, 2245 (2001).
[441] K.-S. Lee, J.-S. Lim, D. S. Ahn, K.-W. Choi, S. K. Kim, and Y. S. Choi, J. Chem. Phys. **124**, 124307 (2006).
[442] H. F. Xu, S. L. Liu, X. X. Ma, D. X. Dai, J. C. Xie, and G. H. Sha, Acta Phys. Sinica **51**, 240 (2002).
[443] H. F. Xu, Y. Guo, S. L. Liu, X. X. Ma, D. X. Dai, and G. H. Sha, J. Chem. Phys. **117**, 5722 (2002).
[444] M. H. M. Janssen, J. W. G. Mastenbroek, and S. Stolte, J. Phys. Chem. A **109**, 7839 (2005).
[445] F. Aguirre and S. T. Pratt, J. Chem. Phys. **122**, 234303 (2005).
[446] A. T. J. B. Eppink and D. H. Parker, J. Chem. Phys. **110**, 832 (1999).
[447] A. T. J. B. Eppink and D. H. Parker, J. Chem. Phys. **109**, 4758 (1998).
[448] Y. S. Kim, W. K. Kang, and K.-H. Jung, J. Chem. Phys. **105**, 551 (1996).
[449] F. Aguirre and S. T. Pratt, J. Chem. Phys. **118**, 1175 (2003).
[450] X.-P. Zhang, W.-B. Lee, and K.-C. Lin, J. Phys. Chem. A **113**, 35 (2009).
[451] H. Fan and S. T. Pratt, J. Chem. Phys. **123**, 204301 (2005).
[452] Y. Tang, W.-B. Lee, Z. Hu, B. Zhang, and K.-C. Lin, J. Chem. Phys. **126**, 064302 (2007).
[453] P. A. Arnold, B. R. Cosofret, S. M. Dylewski, P. L. Houston, and B. K. Carpenter, J. Phys. Chem. A **105**, 1693 (2001).
[454] H. Fan and S. T. Pratt, J. Chem. Phys. **124**, 114312 (2006).
[455] S. Unny, Y. Du, L. C. Zhu, K. Truhins, R. J. Gordon, A. Sugita, M. Kawasaki, Y. Matsumi, R. Delmdahl, D. H. Parker, and A. Berces, J. Phys. Chem. A **105**, 2270 (2001).
[456] K. V. Vidma, A. V. Baklanov, E. B. Khvorostov, V. N. Ishchenko, S. A. Kochubei, A. T. J. B. Eppink, D. A. Chestakov, and D. H. Parker, J. Chem. Phys. **122**, 204301 (2005).
[457] Y. Tanaka, M. Kawasaki, and Y. Matsumi, Bull. Chem. Soc. Jpn. **71**, 2539 (1998).
[458] A. J. van den Brom, T. P. Rakitzis, and M. H. M. Janssen, Phys. Scr. **73**, C83 (2006).
[459] M. L. Lipciuc and M. H. M. Janssen, J. Chem. Phys. **126**, 194318 (2007).
[460] Y. Sato, Y. Matsumi, M. Kawasaki, K. Tsukiyama, and R. Bersohn, J. Phys. Chem. **99**, 16307 (1995).
[461] A. J. van den Brom, T P. Rakitzis, J. van Heyst, T. N. Kitsopoulos, S. R. Jezowski, and M. H. M. Janssen, J. Chem. Phys. **117**, 4255 (2002).
[462] T. P. Rakitzis, A. J. van den Brom, and M. H. M. Janssen, Science **303**, 1852 (2004).
[463] A. J. van den Brom, T. P. Rakitzis, and M. H. M. Janssen, J. Chem. Phys. **121**, 11645 (2004).
[464] S. D. Chambreau, S. A. Lahankar, and A. G. Suits, J. Chem. Phys. **125**, 044302 (2006).
[465] H. Wang, S.-L. Liu, J. Liu, F.-Y. Wang, B. Jiang, and X.-M. Yang, Chinese J. Chem. Phys. **20**, 388 (2007).

[466] M. Kawasaki, Y. Sato, K. Suto, Y. Matsumi, and S. H. S. Wilson, Chem. Phys. Lett. **251**, 67 (1996).
[467] T. Droz-Georget, M. Zyrianov, A. Sanov, and H. Reisler, Ber. Bunsen Ges. Phys. Chem. **101**, 469 (1997).
[468] T. Droz-Georget, M. Zyrianov, H. Reisler, and D. W. Chandler, Chem. Phys. Lett. **276**, 316 (1997).
[469] M. Zyrianov, T. Droz-Georget, and H. Reisler, J. Chem. Phys. **110**, 2059 (1999).
[470] E. Wrede, L. Schnieder, K. H. Welge, F. J. Aoiz, L. Bañares, J. F. Castillo, B. Martinez-Haya, and V. J. Herrero, J. Chem. Phys. **110**, 9971 (1999).
[471] C. Huang, A. D. Estillore, and A. G. Suits, J. Chem. Phys. **128**, 134301 (2008).
[472] A. V. Komissarov, M. P. Minitti, A. G. Suits, and G. E. Hall, J. Chem. Phys. **124**, 014303 (2006).
[473] J. Liu, F. Wang, H. Wang, B. Jiang, and X. Yang, J. Chem. Phys. **122**, 104309 (2005).
[474] S. M. Clegg, B. F. Parsons, S. J. Klippenstein, and D. L. Osborn, J. Chem. Phys. **119**, 7222 (2003).
[475] C. W. Walter, P. C. Cosby, and H. Helm, J. Chem. Phys. **112**, 4621 (2000).
[476] D. W. Neyer, A. J. R. Heck, and D. W. Chandler, J. Chem. Phys. **110**, 3411 (1999).
[477] N. Hansen, A. M. Wodtke, A. V. Komissarov, and M. C. Heaven, Chem. Phys. Lett. **368**, 568 (2003).
[478] S. J. Matthews, S. Willitsch, and T. P. Softley, Phys. Chem. Chem. Phys. **9**, 5656 (2007).
[479] N. T. Form, B. J. Whitaker, L. Poisson, and B. Soep, Phys. Chem. Chem. Phys. **8**, 2925 (2006).
[480] T. Suzuki, V. P. Hradil, S. A. Hewitt, P. L. Houston, and B. J. Whitaker, Chem. Phys. Lett. **187**, 257 (1991).
[481] S. Wolf and H. Helm, Phys. Rev. A **56**, R4385 (1997).
[482] M. Ahmed, D. S. Peterka, and A. G. Suits, Abs. Pap Am. Chem. Soc. **215**, U164 (1998).
[483] V. K. Nestorov and J. I. Cline, J. Chem. Phys. **111**, 5287 (1999).
[484] Y. X. Mo, H. Katayanagi, and T. Suzuki, J. Chem. Phys. **110**, 2029 (1999).
[485] O. L. A. Monti, H. Dickinson, S. R. Mackenzie, and T. P. Softley, J. Chem. Phys. **112**, 3699 (2000).
[486] B. F. Parsons, D. W. Chandler, E. C. Sklute, S. L. Li, and E. A. Wade, J. Phys. Chem. A **108**, 9742 (2004).
[487] E. A. Wade, J. I. Cline, K. T. Lorenz, C. Hayden, and D. W. Chandler, J. Chem. Phys. **116**, 4755 (2002).
[488] A. V. Demyanenko, A. B. Potter, V. Dribinski, and H. Reisler, J. Chem. Phys. **117**, 2568 (2002).
[489] A. B. Potter, V. Dribinski, A. V. Demyanenko, and H. Reisler, J. Chem. Phys. **119**, 7197 (2003).
[490] M. Tsubouchi and T. Suzuki, Chem. Phys. Lett. **382**, 418 (2003).
[491] M. Tsubouchi, C. A. de Lange, and T. Suzuki, J. Chem. Phys. **119**, 11728 (2003).
[492] V. Dribinski, A. B. Potter, I. Fedorov, and H. Reisler, Chem. Phys. Lett. **385**, 233 (2004).
[493] V. Dribinski, A. Potter, I. Fedorov, and H. Reisler, J. Chem. Phys. **121**, 12353 (2004).
[494] V. K. Nestorov, R. D. Hinchliffe, R. Uberna, J. I. Cline, K. T. Lorenz, and D. W. Chandler, J. Chem. Phys. **115**, 7881 (2001).
[495] T. J. Obernhuber, U. Kensy, and B. Dick, Phys. Chem. Chem. Phys. **5**, 2799 (2003).
[496] A. G. Suits, R. L. Miller, L. S. Bontuyan, and P. L. Houston, J. Chem. Soc. Faraday Trans. **89**, 1443 (1993).
[497] G. Li, J. Parr, I. Fedorov, and H. Reisler, Phys. Chem. Chem. Phys. **8**, 2915 (2006).
[498] K. V. Vidma, A. V. Baklanov, Y. Zhang, and D. H. Parker, J. Chem. Phys. **125**, 133303 (2006).
[499] H. A. Cruse and T. P. Softley, J. Chem. Phys. **122**, 124303 (2005).
[500] M. L. Lipciuc and M. H. M. Janssen, J. Chem. Phys. **127**, 224310 (2007).
[501] V. Blanchet, P. C. Samartzis, and A. M. Wodtke, J. Chem. Phys. **130**, 034304 (2009).

[502] J. Dura, R. de Nalda, J. Alvarez, J. G. Izquierdo, G. A. Amaral, and L. Bañares, ChemPhysChem. **9**, 1245 (2008).
[503] R. de Nalda, J. Dura, A. Garcia-Vela, J. G. Izquierdo, J. Gonzalez-Vazquez, and L. Bañares, J. Chem. Phys. **128**, 244309 (2008).
[504] D. W. Chandler, J. W. Thoman, M. H. M. Janssen, and D. H. Parker, Chem. Phys. Lett. **156**, 151 (1989).
[505] D. W. Chandler, M. H. M. Janssen, S. Stolte, R. N. Strickland, J. W. Thoman, and D. H. Parker, J. Phys. Chem. **94**, 4839 (1990).
[506] M. H. M. Janssen, D. H. Parker, G. O. Sitz, S. Stolte, and D. W. Chandler, J. Phys. Chem. **95**, 8007 (1991).
[507] J. W. G. Mastenbroek, C. A. Taatjes, K. Nauta, M. H. M. Janssen, and S. Stolte, J. Phys. Chem. **99**, 4360 (1995).
[508] A. J. van den Brom, M. Lipciuc, and M. H. M. Janssen, Chem. Phys. Lett. **368**, 324 (2003).
[509] C. Vallance, Phil. Trans. R. Soc. Lond. Ser. A **362**, 2591 (2004).
[510] J. G. Izquierdo, G. A. Amaral, F. Ausfelder, F. J. Aoiz, and L. Bañares, ChemPhysChem. **7**, 1682 (2006).
[511] G. A. Amaral, F. Ausfelder, J. G. Izquierdo, L. Rubio-Lago, and L. Bañares, J. Chem. Phys. **126**, 024301 (2007).
[512] P. Quintana, R. F. Delmdahl, D. H. Parker, B. Martinez-Haya, F. J. Aoiz, L. Bañares, and E. Verdasco, Chem. Phys. Lett. **325**, 146 (2000).
[513] B. Martínez-Haya, P. Quintana, L. Bañares, P. Samartzis, D. J. Smith, and T. N. Kitsopoulos, J. Chem. Phys. **114**, 4450 (2001).
[514] B. Martinez-Haya, M. J. Bass, M. Brouard, C. Vallance, I. Torres, and J. Barr, J. Chem. Phys. **120**, 11042 (2004).
[515] A. G. Sage, M. G. D. Nix, and M. N. R. Ashfold, Chem. Phys. **347**, 300 (2008).
[516] M. L. Lipciuc, J. B. Buijs, and M. H. M. Janssen, Phys. Chem. Chem. Phys. **8**, 219 (2006).
[517] J. A. Parr, G. Li, I. Fedorov, A. J. McCaffery, and H. Reisler, J. Phys. Chem. A **111**, 7589 (2007).
[518] H. Fan and S. T. Pratt, J. Chem. Phys. **125**, 144302 (2006).
[519] L. Poisson, K. D. Raffael, M.-A. Gaveau, B. Soep, J.-M. Mestdagh, J. Caillat, R. Taieb, and A. Maquet, Phys. Rev. Lett. **99**, 103401 (2007).
[520] M. A. Buntine, D. P. Baldwin, R. N. Zare, and D. W. Chandler, J. Chem. Phys. **94**, 4672 (1991).
[521] A. Gijsbertsen, H. Linnartz, G. Rus, A. E. Wiskerke, S. Stolte, D. W. Chandler, and J. Klos, J. Chem. Phys. **123**, 224305 (2005).
[522] A. G. Suits, L. S. Bontuyan, P. L. Houston, and B. J. Whitaker, J. Chem. Phys. **96**, 8618 (1992).
[523] L. S. Bontuyan, A. G. Suits, P. L. Houston, and B. J. Whitaker, J. Phys. Chem. **97**, 6342 (1993).
[524] M. S. Westley, K. T. Lorenz, D. W. Chandler, and P. L. Houston, J. Chem. Phys. **114**, 2669 (2001).
[525] K. T. Lorenz, D. W. Chandler, J. W. Barr, W. Chen, G. L. Barnes, and G. I. Cline, Science **293**, 2063 (2001).
[526] J. I. Cline, K. T. Lorenz, E. A. Wade, J. W. Barr, and D. W. Chandler, J. Chem. Phys. **115**, 6277 (2001).
[527] T. N. Kitsopoulos, M. A. Buntine, D. P. Baldwin, R. N. Zare, and D. W. Chandler, Science **260**, 1605 (1993).
[528] W. R. Simpson, T. P. Rakitzis, S. A. Kandel, A. J. Orr-Ewing, and R. N. Zare, J. Chem. Phys. **103**, 7313 (1995).
[529] A. J. Orr-Ewing, W. R. Simpson, T. P. Rakitzis, and R. N. Zare, J. Chem. Phys. **106**, 5961 (1997).

[530] N. Yonekura, C. Gebauer, H. Kohguchi, and T. Suzuki, Rev. Sci. Instrum. **70**, 3265 (1999).
[531] K. T. Lorenz, M. S. Westley, and D. W. Chandler, Phys. Chem. Chem. Phys. **2**, 481 (2000).
[532] M. Ahmed, D. S. Peterka, and A. G. Suits, Phys. Chem. Chem. Phys. **2**, 861 (2000).
[533] M. Ahmed, D. S. Peterka, and A. G. Suits, Chem. Phys. Lett. **317**, 264 (2000).
[534] P. C. Samartzis, D. J. Smith, T. P. Rakitzis, and T. N. Kitsopoulos, Chem. Phys. Lett. **324**, 337 (2000).
[535] K. T. Lorenz, D. W. Chandler, and G. C. McBane, J. Phys. Chem. A **106**, 1144 (2002).
[536] X. Liu, R. L. Gross, and A. G. Suits, J. Chem. Phys. **116**, 5341 (2002).
[537] B. Zhang, J. Zhang, and K. Liu, J. Chem. Phys. **122**, 104310 (2005).
[538] J. Zhou, W. Shiu, J. J. Lin, and K. Liu, J. Chem. Phys. **124**, 104309 (2006).
[539] J. Zhou, J. J. Lin, W. Shiu, and K. Liu, Phys. Chem. Chem. Phys. **8**, 3000 (2006).
[540] J. G. Zhou, J. J. Lin, and K. Liu, J. Chem. Phys. **119**, 8289 (2003).
[541] J. J. Lin, J. G. Zhou, W. C. Shiu, and K. Liu, Science **300**, 966 (2003).
[542] J. G. Zhou, J. J. Lin, W. C. Shiu, and K. Liu, J. Chem. Phys. **119**, 4997 (2003).
[543] W. Shiu, J. J. Lin, K. Liu, M. Wu, and D. H. Parker, J. Chem. Phys. **120**, 117 (2004).
[544] R. L. Toomes and T. N. Kitsopoulos, Phys. Chem. Chem. Phys. **5**, 2481 (2003).
[545] R. L. Toomes, A. J. van den Brom, T. N. Kitsopoulos, C. Murray, and A. J. Orr-Ewing, J. Phys. Chem. A **108**, 7909 (2004).
[546] C. Murray, A. J. Orr-Ewing, R. L. Toomes, and T. N. Kitsopoulos, J. Chem. Phys. **120**, 2230 (2004).
[547] J. Zhou, B. Zhang, J. J. Lin, and K. Liu, Mol. Phys. **103**, 1757 (2005).
[548] B. Zhang, W. Shiu, and K. Liu, J. Phys. Chem. A **109**, 8983 (2005).
[549] B. Zhang, W. Shiu, and K. Liu, J. Phys. Chem. A **109**, 8989 (2005).
[550] B. Zhang, W. Shiu, J. J. Lin, and K. Liu, J. Chem. Phys. **122**, 131102 (2005).
[551] B. F. Parsons, K. E. Strecker, and D. W. Chandler, Eur. Phys. J. D **38**, 15 (2006).
[552] W. Li, C. Huang, M. Patel, D. Wilson, and A. G. Suits, J. Chem. Phys. **124**, 011102 (2006).
[553] C. Huang, W. Li, and A. G. Suits, J. Chem. Phys. **125**, 133107 (2006).
[554] H. Kohguchi, T. Suzuki, S. Nanbu, T. Ishida, G. V. Milnikov, P. Oloyede, and H. Nakamura, J. Phys. Chem. A **112**, 818 (2008).
[555] H. Kohguchi and T. Suzuki, ChemPhysChem. **7**, 1250 (2006).
[556] B. Retail, J. K. Pearce, S. J. Greaves, R. A. Rose, and A. J. Orr-Ewing, J. Chem. Phys. **128**, 184303 (2008).
[557] B. Zhang, S. Yan, and K. Liu, J. Phys. Chem. A **111**, 9263 (2007).
[558] B. Retail, R. A. Rose, J. K. Pearce, S. J. Greaves, and A. J. Orr-Ewing, Phys. Chem. Chem. Phys. **10**, 1675 (2008).